HYPOTHALAMIC CELL TYPES AND CIRCUITS THAT DRIVE BEHAVIORS ESSENTIAL FOR SURVIVAL

by

Julia Elizabeth Slocomb Dluzen

A dissertation submitted to Johns Hopkins University in conformity with the requirements for the degree of Doctor of Philosophy

Baltimore, Maryland

January 2018

Abstract

Cracking the cytoarchitectural organization, activity patterns, and neurotransmitter nature of genetically-distinct cell types in the lateral hypothalamus is fundamental to understanding survival behaviors such as feeding. Here I revealed that chemogenetic inhibition of parvalbumin-positive neurons in the lateral hypothalamus increases food consumption and general arousal in sated mice. Moreover, functional imaging using two-photon fluorescence endomicroscopy exhibited decreased activity of these neurons during food-deprived conditions, suggesting an unprecedented role in encoding for metabolic states. Furthermore, these neurons are fast-spiking similar to canonical inhibitory parvalbumin neurons in the neocortex and hippocampus, but unlike those cells, lateral hypothalamic parvalbumin neurons are excitatory. Finally, sensory detection of food rapidly increases the activity of these neurons.

Primary Reader: Yeka Aponte

Secondary Readers: Haiqing Zhao, Antonello Bonci, Carl Lupica, Samer Hattar, Robert Johnston

Preface

First and foremost, I would like to begin by thanking Dr. Yeka Aponte for deciding to take a chance on me. As a student with a highly unorthodox background, she took a risk taking me in as her first graduate student, and I will be forever grateful for her decision. Under her guidance, support, and mentorship I have flourished. She has helped me learn how to push myself further than I imagined and how to be kind to myself when I have hit my limit, and thus has helped me become a better scientist and person. She has built a lab full of wonderful people and brought us together to pursue a common goal with extraordinary passion and commitment, which she leads through example. I am proud to have been Yeka's first student and aim to pass on her courage and fervor for discovery to others for the rest of my days.

Additionally, I would like to thank my committee members for their support and enthusiasm for this work and my progress throughout graduate school. So many of you have gone above and beyond the call of duty and have been mentors to me from the start of my time in graduate school. Dr. Antonello Bonci has made time for me and supported me from the first time I stepped into NIDA, and I will strive to embody his style of person-focused leadership for the rest of my career. I would like to thank Dr. Carl Lupica for providing wisdom and humor when I needed it and for always helping me to delve deeper and to ask better questions. I would like to thank Dr. Samer Hattar for taking me under his wing from the first moment I started at Hopkins. He is a joy to know and work with. Similarly, I am indebted to Dr. Haiqing Zhao for his advice and creativity, he has given me confidence and kindness in spades. Additionally, I would like to thank Dr. Robert

Johnston, who so kindly agreed to join my committee this year and has approached everything with gusto and honesty. I think it is rare for a student to look forward to their committee meetings, and I thank each of you for providing such a positive and creative environment for me to learn in.

I would be remiss to continue without thanking my lab members, a second family to me and a group of people I truly cherish. Please know that I could write pages about every one of you and still not begin to reflect my gratitude to you all. Sarah Sarsfield has been a mentor, a fabulous friend, a shoulder to lean on, and an inspiration. Dr. Alexandre Kisner is a living example of the kind of person I want to be, always taking the time to invest his energy in helping others. He has always made time to help me, whether it be discussing results, assisting on an experiment, or brewing beer. From the moment Dr. Maria Laura Zuccoli joined the lab I had no doubt that I had found a kindred spirit whom I would quickly form deep admiration for. She has been a sounding board and voice of reason in my life.

There are so many other people at NIDA outside of my lab that have helped me throughout my time here. Drs. Matthew Gardner and Brian Sadacca have taught me how to bring my computational ideas to reality and have made learning how to code surprisingly fun. Dr. Hugo Tejeda opened my mind to the possibilities and challenges of behavioral assays, and was always willing to find time to talk through experiments. I would be remiss if I didn't take a moment to thank the many members of the animal care staff, security personnel, and custodial staff at NIDA for always finding ways to make my life at work possible and feel like a second home.

Additionally, I would like to take a moment to thank my first scientific mentor, Dr. Kerstin Bettermann. I would not have ended up here without her. She revealed a world of possibilities to me and gave me endless opportunities to grow and to challenge myself. She has been a role model for me as a scientist, a mentor, a woman, a mother, and a friend.

Without a doubt, my greatest source of support, inspiration and delight has been my husband, Dr. Douglas Dluzen. Doug has been my editor, assistant, and cheerleader, along with any other role I needed him to play without complaint. I cannot imagine anyone I would rather have by my side throughout this journey and into the future. I am grateful to our new son Parker, for being a reminder to slow down and appreciate each moment. I would also like to thank my wonderful parents, Terri and Steve Slocomb, and my brothers, Josh and Matt Slocomb, for giving me the freedom to pursue my passions while giving me love and four unique and equally important role models in life. You have each shown me how to be fearless, honest, and creative, as well as how to devote yourself to something you love, and to have compassion for all living things. Additionally, I would like to thank my dog (Flynn) and my cat (Wrigley), for reminding me to find a balance of work and play and for appearing to listen with fascination as I practiced presentations for countless hours.

Table of Contents

List of Tables

List of Figures

Key acronym guide

Brain regions:

ARC = arcuate nucleus
BNST = bed nucleus of the stria terminalis
LH = lateral hypothalamus
LHb = lateral habenula
PAG = periaqueductal gray matter
PVN = paraventricular nucleus
VMH = ventromedial hypothalamus

Cell types:

AGRP = agouti related peptide
GABA = gamma-aminobutyric acid
HCRT = hypocretin/oxytocin
LEPR = leptin receptor
MCH = melanin-concentrating hormone
POMC = proopiomelanocortin
PV = parvalbumin
VGAT = vesicular GABA transporter
VGLUT2 = vesicular glutamate transporter type 2

Chapter 1

General introduction

1.1 Overview

It has been argued that feeding and reproduction are the core drivers of the continuum of behavior for most vertebrate species (1); indeed, all behavior may exist to support an organism's ability to survive as both an individual (energy balance) and as a species (reproduction). This concept is not unique to researchers, one need only look to the wisdom of Dolly Parton:

"My weaknesses have always been food and men – in that order."

Ms. Parton's instinctual understanding of the hierarchy of animal behavior exemplifies the findings of decades of research. Indeed, feeding behaviors and their regulatory circuits interact with all other survival behaviors. Survival behaviors, such as feeding, represent some of the most critical functions for survival and homeostasis in all species. Without survival behaviors we would not exist, and evolution may have taken a very different path, or perhaps no path at all.

Natural behaviors include a broad family of behaviors which are required for survival including feeding, drinking, mating, arousal, aggression, and fear. The brain does not drive such survival behaviors in complete seclusion, it integrates sensory information from the environment and peripheral organ systems to coordinate homeostasis and response to stimuli. Although higher level brain function and peripheral inputs may interact with the manifestation and modulation of these behaviors, research throughout the past half century has consistently shown that the hypothalamus is the central regulator of homeostasis. Research from the past 20 years has driven this field forward with alacrity due to significant advances in gene therapy and technology. Such progress

has allowed scientists to identify specific neuronal circuits driving survival behaviors and to begin to piece together the chemical and temporal mechanisms by which they regulate these behaviors. Hereafter, I will review the supporting historical information that will provide scope and context to the techniques and analytical approaches used in this dissertation.

1.2 Historical context leading to current approaches in neuronal circuits

Scientists had been probing the brain for centuries before modern theories of feeding behavior regulation were proposed. Despite rudimentary methods, some of this work provided compelling observations long before technology allows the specificity we have today. In the fifth century BCE, Alcmaeon became the first physician to use dissection to postulate his theory that the brain is the source of sensory perception (2). During the fourth and third centuries BCE, Hippocrates and his peers deducted that the brain is the center of pain, fear, and sleep via observations of patients with epilepsy (3). The role of the brain remained a matter of great debate until the rise of physiologists and anatomists in the 18th and 19th centuries CE. For example, Charles Bell and François Magendie performed experiments in live animals to study motor responses and sensation (4, 5). Around this same period, Camillo Golgi and Santiago Ramón y Cajal were studying the structure of nerve cells, and Emil du Bois-Reymond, Johannes Peter Müller, and Hermann von Helmholtz were studying the electrical function of neurons, driving our understanding of neuroscience at the cellular level (6). However, a tremendous gap remained between anatomy and behavior.

Documented studies of behavior date back as far as the 17th century with René Descartes, but it was not until Charles Darwin's studies of evolution that we began to consider the use of animals to model human behavior (7, 8). Karl Wernicke and Paul Broca made enormous advances by identifying areas of the brain that were responsible for speech and language and in enumerating that these areas communicate using neuronal pathways (6). In the mid-1900s animal models of behavior first introduced by Darwin, were refined and combined with the advent of surgical techniques to progress our understanding of how the brain drives feeding and other survival behaviors.

Behavior does not occur spontaneously, it requires a stimulus of some sort from which motivation (*i.e.* the desire to complete an action or reach a goal) and drive (*i.e.* the result of unmet instinctual needs that ultimately induce motivation) develop. The neural correlates of these processes are still being explored today, but the foundation of such work is rooted in the theories and findings of psychologist Clark L. Hull. The work of Hull and his contemporaries introduced the concepts of conditioning and animal learning, which have provided a system which we now use to determine the contributions of neuronal circuits to the different motivating factors that shape survival behaviors. Hull theorized that when animals are deprived of a resource, the deprivation generates a need which, in turn, activates a drive. This drive subsequently produces a behavior towards a goal that represents a specific value to the animal's survival (**Figure 1**, (9)). Around the same time, Karl Lashley's work in studying motivation led him to conclude that behaviors such as feeding were not driven by a chain reaction of peripheral signals, as much of the field thought at the time. Lashley hypothesized that behaviors were a result of motivation

and thus must be driven by the brain (10). Nikolaas Tinbergen expanded on these concepts and provided a framework for understanding survival behaviors and how they are interrelated. He theorized that external stimuli generate motivation, which is stored in the brain. Response to this motivation is blocked at several centers in the brain, each one gating the release of the signal to the next center in a cascade until the behavior ultimately results (11). The work of Jean Mayer and Gordon C. Kennedy in the 1950s and 1960s led to two competing hypotheses of energy balance: the glucostatic model and the lipostatic model. The glucostatic model suggests that feeding is regulated by plasma glucose level; the lipostatic model suggests that feeding is a reflection of maintaining a homeostatic level of fat in the body (12, 13). In time, both models were proven to be partially correct—the glucostatic model relating to short term feeding behavior and the lipostatic model being more important in long term feeding patterns. Together, these theories shaped the way researchers conceptualized their discoveries throughout the middle of the 20th century, the period in which modern neuroscience was born.

The experimental data to support a relationship between the brain and peripheral signals of nutrition emerged during the same period that these early conceptual models of neuronal circuits were emerging. Observational and case studies were the only sources of information relating the brain to behavior until the invention of the stereotaxic surgical instrument in 1939, which facilitated performance of brain surgeries in animals with a high degree of precision. A year later, A. W. Hetherington and S. W. Ranson showed that lesions to the ventromedial hypothalamus (VMH) were capable of driving obesity and thirst in rats (14). Attempting to replicate these findings, John Brobeck and Bal Krishnan

Anand discovered that lesions in the hypothalamus of rats induced dramatic weight loss. Detailed histological analysis revealed that their lesions were much more extensive and incorporated the lateral hypothalamus (LH) rather than the more medial hypothalamic areas lesioned by Hetherington and Randon, which likely accounted for the observed difference in response (15). These observations led to a generation of behavior researchers who experimented with the size and location of lesions and electrical stimulation of the brain. These discoveries formed the basis of the "dual center theory" of feeding behavior and energy regulation, wherein the VMH functions as a "satiety center" and the LH functions as a "hunger center" (16). Years later, chemical lesions revealed that fibers of passage that emanated from, terminated in, and passed through the LH were also involved in regulating feeding, drinking, and body weight (17-21). These studies generated interest in the signals being used by the VMH to regulate feeding.

G. R. Hervey used a unique approach to study the VMH in which he employed a technique called parabiosis, developed by Paul Bert in the mid-1800s, to surgically attach two rats together. Hervey lesioned the VMH in one of the two rats prior to their "union" and made an enormously important discovery. As expected, the lesioned rat grew obese, but more importantly, the non-lesioned conjoined rat stopped eating and became emaciated (**Figure 2**). This result indicated that there was a factor produced in the blood of the lesioned rat that was being passed to the non-lesioned rat, and this factor was inhibiting food intake in the non-lesioned rat (22). Around the same time, a recessive mutation developed in a litter of mice in the laboratory of Ann Ingalls and colleagues. This mutation led the mice to develop severe obesity and infertility, and Ingalls and her

colleagues called the mutation *obese* or *ob/ob* (23). A few years later, Douglas Coleman identified another strain of obese mice, caused by a mutation in a gene on a different chromosome. This mutation induced obesity as well as diabetes, and thus was called *db/db*. Coleman performed parabiosis experiments with *ob/ob* and *db/db* mice, and determined that joining an *ob/ob* mouse with a normal mouse attenuated the weight gain in the obese partner. Joining a *db/db* mouse with a normal mouse induced emaciation in the normal partner due to loss of appetite. When a *db/db* and an *ob/ob* mouse were joined, the *ob/ob* mouse reduced its food intake and weight to that of a normal mouse, while the *db/db* mouse remained obese. Coleman concluded that the *db/db* mice must be producing a circulating satiety factor that they were insensitive to, and the *ob/ob* mice have normal sensitivity to this satiety factor but have lost production of the factor itself (24, 25). This theory was finally proven correct two decades later, when it was found that the *ob* gene encodes the satiety hormone leptin, while the *db* gene encodes the receptor for leptin (26, 27). Leptin receptor-positive (LEPR) neurons have been identified in many areas of the brain, but especially in areas of the brain associated with driving feeding behaviors. Ultimately, other feeding and satiety circuits throughout the hypothalamus in addition to the VMH and LH were identified using similar methods; these include the arcuate nucleus (ARC), the dorsomedial hypothalamus (DMH), and the paraventricular hypothalamus (PVN) (1, 28).

The development of state-of-the-art techniques such as, patch-clamp electrophysiology, genetically-modified mice, fluorescent reporter genes, optogenetics, chemogenetics, and functional imaging has allowed researchers to establish causal

relationships between activity in specific cell types, circuit function, and animal behavior. Thus, the focus began to shift from studying "feeding centers" to understanding the role of genetically-identified cell types and circuits that drive motivated survival behaviors.

1.3 Established feeding circuits

The melanocortin system is perhaps the most well studied circuit driving feeding and energy balance (**Figure 3**). Two juxtaposed populations of neurons within the ARC were identified in the 1980s to 1990s: a population of cells expressing proopiomelanocortin (POMC) and cocaine-amphetamine regulated transcript (CART) and a population expressing neuropeptide Y (NPY) and agouti related peptide (AGRP) (29-32). The POMC neurons and POMC cleavage products were found to reduce feeding and increase energy expenditure, while NPY/AGRP neurons as well as the peptides themselves induce feeding and reduce energy expenditure (31, 33-36). AGRP is an antagonist of receptors for POMC cleavage products, and NPY neurons actively inhibit POMC cells, creating a local circuit for the regulating of feeding (31, 37). Dozens of areas of the brain have been shown to project to POMC and AGRP neurons in the ARC (38). POMC and NPY/AGRP neurons have been shown to project to several areas of the brain known to be involved with feeding and energy expenditure, including (but not limited to) the PVN, LH, DMH, VMH, bed nucleus of the stria terminalis (BNST), paraventricular thalamic nucleus (PVT), and the periaqueductal gray matter (PAG) (38-45). ARC NPY/AGRP projection sites are not innervated by the same neurons, rather, topographically distributed subgroups of this population project to different sites in parallel (39). Recently, great strides in

understanding the function of ARC NPY/AGRP and POMC neurons have been made thanks to the advent of multiple approaches to recording the activity of these neurons *in vivo* during behavior. Surprisingly, researchers discovered that the activity of AGRP neurons declines and the activity of POMC neurons increases rapidly and dramatically upon both, the sensory detection of food and nutrient ingestion (**Figure 4**, (46-49)). It was shown that AGRP neuron activity in sated mice was inhibited 5 to 15 minutes following peripheral injection of ghrelin, a hormone released endogenously by the stomach to stimulate feeding (46). Interestingly, injection of the satiety hormone leptin into fasted mice induced a delayed and attenuated shift in AGRP and POMC neuron activity, which was enhanced in leptin-deficient mice (49). While this may seem counterintuitive, as it was previously shown that optogenetic stimulation of AGRP neurons drove voracious feeding, additional experiments have shown that AGRP neurons appear to be regulating food seeking rather than merely hunger (33, 50). Therefore, the mechanism for gating AGRP and POMC activity in response to nutritional cues during different metabolic states is still a challenge for the feeding field.

Several AGRP and POMC neuron projection sites were found to regulate food intake, but the arousal and energy expenditure effects of these neurons remain less well understood (38, 39). Studies using numerous techniques have indicated that cells and pathways in the lateral hypothalamus LH play a role in feeding, arousal, energy expenditure, and motivation (28). Several intermingled populations of cells have been identified in the LH which influence these behaviors. These encompass a diverse collection of cell types, defined by the expression of classical neurotransmitters,

receptors, and neuropeptides, such as vesicular glutamate transporter type 2 (VGLUT2), vesicular GABA (GABA, γ-aminobutyric acid transporter (VGAT), LEPR, hypocretin/orexin (HCRT), parvalbumin (PV), and melanin-concentrating hormone (MCH) (28, 51, 52). While some markers represent distinct populations, others are expressed in overlapping populations of neurons. For example, the intermingled and yet distinct populations of HCRT and MCH neurons both express VGLUT2, but MCH neurons have also been reported to express GABA-producing enzymes (53-56). Meanwhile, GABAergic LEPR neurons in the LH do not overlap with MCH or HCRT neurons but are known to be intermingled with them. LEPR neurons are thought to regulate metabolism and energy homeostasis both directly through the regulation of the mesolimbic dopamine system and indirectly via regulation of local HCRT neurons (51). HCRT neurons have been shown to drive arousal and increased food intake, but also play a role in reward, whereas MCH neurons promote REM sleep but are also thought to drive food intake (57-59). HCRT and MCH neurons project to many of the same target sites, reciprocally synapse onto each other as well as other LH neurons, and yet drive differing effects on their targets (1). Interestingly, optogenetic stimulation of LH GABAergic neurons was found to drive intense feeding; however, stimulation of LH glutamatergic neurons inhibits food intake (60, 61). LH neurons project to diverse areas of the brain including the lateral habenula (LHb), an area typically associated with reward and aversion processing via downstream indirect regulation of VTA dopamine neurons (51, 57, 62, 63). A subpopulation of LH glutamatergic neurons projecting to the LHb, an area not previously indicated to be involved with food intake, were recently discovered to inhibit food intake when

stimulated and drive increased food intake when inhibited (64). Greater specificity regarding the molecular identities of subpopulations of neurons composing the LH glutamatergic population of neurons projecting to the LHb has not been determined to date.

1.4 Parvalbumin neurons

Parvalbumin (PVALB or PV) neurons have been shown to serve a variety of important functions throughout the brain, from regulating network dynamics in the cortex and hippocampus to modulating local microcircuit function (65). PV is a high affinity calcium binding protein known to buffer intracellular calcium dynamics and regulate calcium localization (66). PV is found in a diverse family of cells that are distinguished by location, site of axon targeting, neurotransmitter identity, cell morphology, and firing properties. Throughout the central nervous system, PV-expressing neurons are typically GABAergic interneurons with fast-spiking characteristics.

Cortical GABAergic PV neurons regulate gamma oscillations in the cortex, which are critical for normal cortical function (67). PV knockout mice are known to exhibit increased propensity for seizures, which is thought to result from asynchronicity in the absence of PV (68). Additionally, PV dysfunction has been associated with cognitive deficits seen in schizophrenia (69). In animal models, PV neurons have also been found to regulate fear responses, mobility, reward-related behavioral flexibility, and attention (70-73). Thus, the potential clinical significance of PV neurons is vast.

1.5 Role of PV neurons in the neocortex and hippocampus

The large majority of PV neurons are known to be fast-spiking, GABAergic interneurons that encompass the largest subgroup of interneurons in the cortex and hippocampus (74). In the cortex, PV labeling does not overlap with other common immunohistochemical markers such as somatostatin, calretinin, cholecystokinin, vasointestinal peptide, or neuropeptide Y (75). The thin yet extensive dendritic arbors of such cortical PV interneurons exhibit highly efficient responses to excitatory inputs. This response is due to a high ratio of dendritic potassium (K^+) to sodium (Na^+) channels and strong AMPA (α-amino-3-hydroxy-5-methyl-4-isoxazolepropionic acid) channels that receive excitatory signals from clustered presynaptic inputs. In particular, the KV3 type K^+ channels allow the elevated threshold and rapid activation/deactivation responses that are characteristic of PV neurons. The most abundant classes of PV neurons, cortical basket and chandelier interneurons, send dense short-range axons to nearby neurons, typically pyramidal cells, and exert potent inhibitory control over these cells (basket (76); chandelier (77); in rat: (78-80)).

1.6 Role of PV neurons in other brain regions

Some populations of PV neurons have been shown to send long range projections throughout the brain. Small numbers of PV positive projections have been identified in the corpus callosum and subcortical white matter (81). Recently, a group of GABAergic PV neurons in the primary motor cortex with long range projections to the striatum were shown to inhibit motor output (71). Additionally, populations of retrosplenial and

somatosensory GABAergic PV neurons have been shown to project to the caudal striatum (82).

1.7 Figures

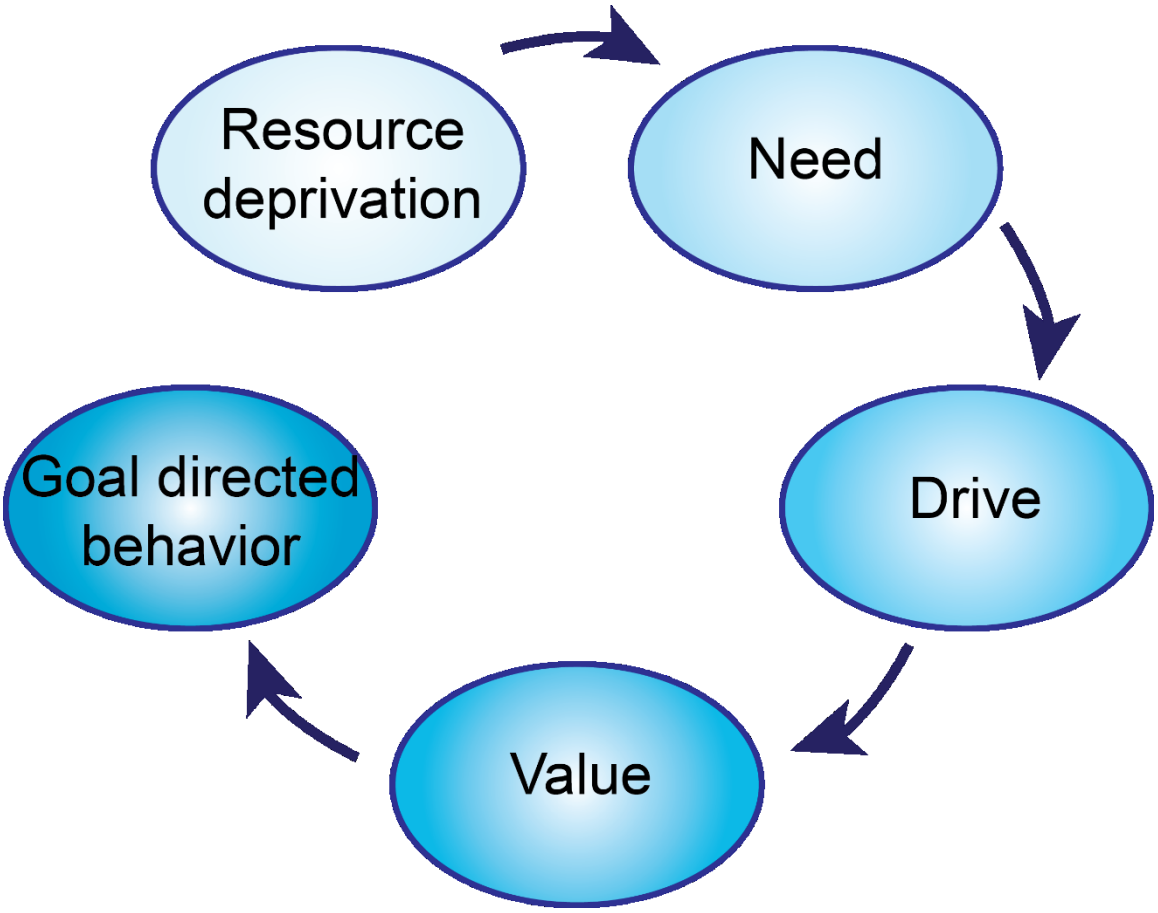

Figure 1

Drive reduction theory model (based on (9)). This model proposes that organisms are driven by biological need to perform goal-directed behaviors to reach a reward or homeostatic state. When this goal is reached, the result is typically rewarding, and thus animals learn to associate the pleasurable reduction in an aversive drive with a specific behavior. This is the cycle by which reinforcement can induce conditioned learning.

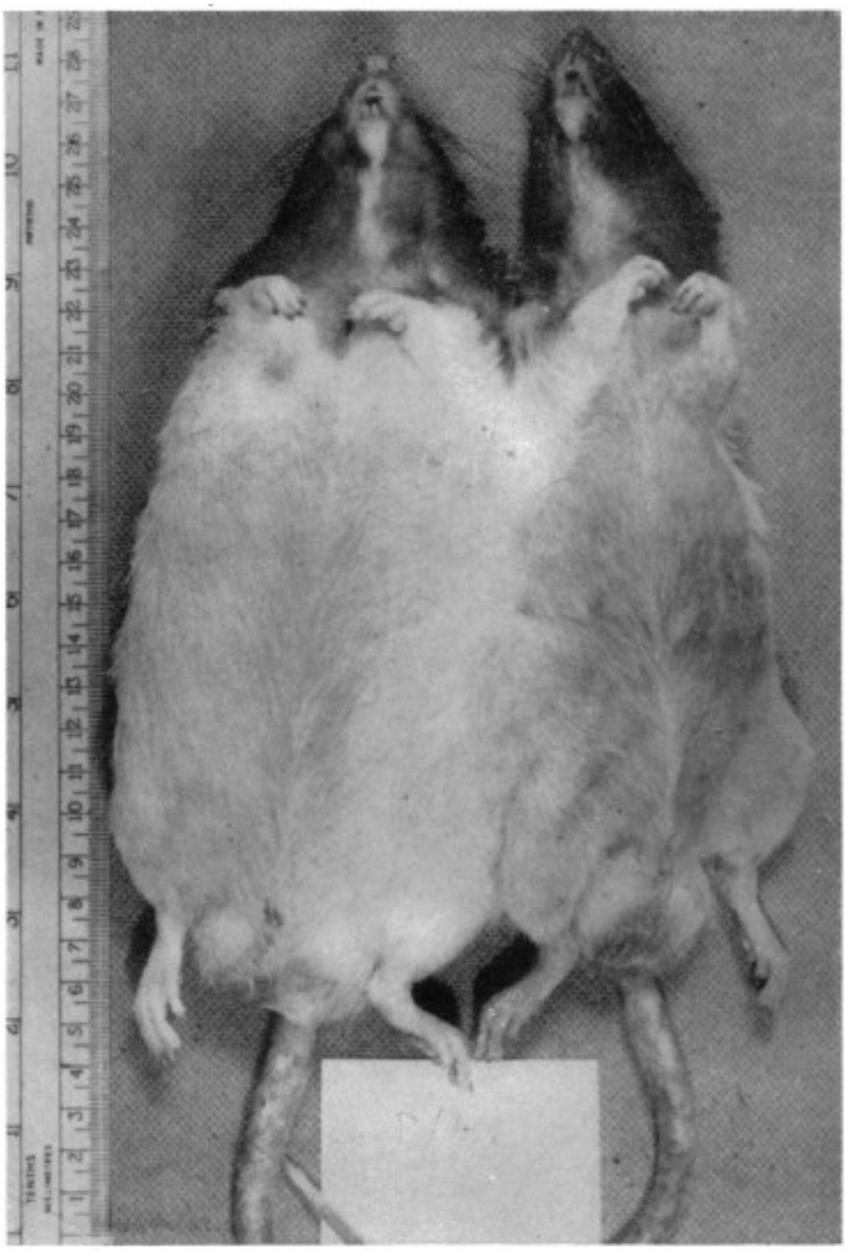

Figure 2

Image of G. R. Hervey parabiotic experiment with VMH lesion ((22); Plate 2). The rodent on the left was given a lesion in the VMH, and grew obese; the non-lesioned, conjoined rat shown on the right stopped eating and became emaciated. This indicated that there was a factor produced in the blood of the lesioned rat that was passed to the non-lesioned rat, and this factor was inhibiting food intake in the non-lesioned rat.

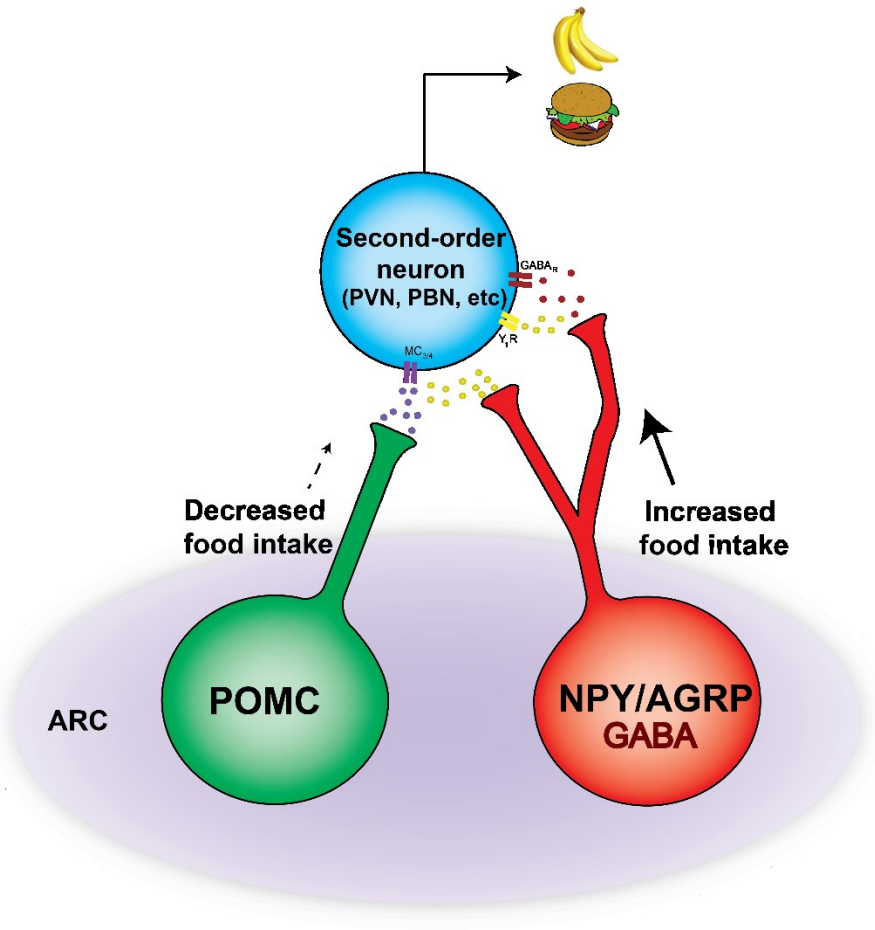

Figure 3

Schematic illustration of the melanocortin system (Adapted from (83) Figure 1). The melanocortin system consists of two intermingled populations of GABAergic neurons in the arcuate nucleus: AGRP (NPY/AGRP) and POMC neurons. POMC neurons target cells in the same target nuclei as AGRP neurons, where AGRP/NPY and POMC cleavage products compete to bind to receptors and drive opposite behavioral effects.

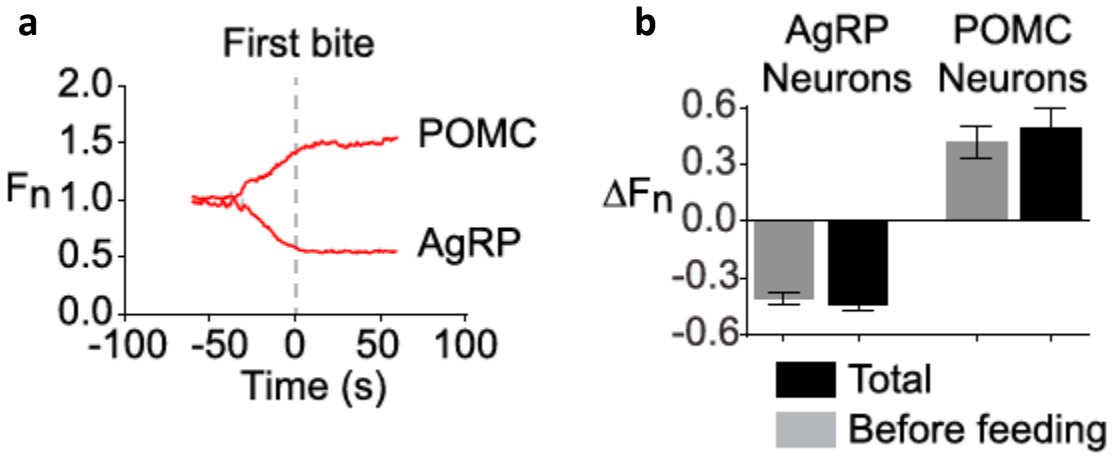

Figure 4

Sensory detection of food rapidly regulates AGRP and POMC neurons (Adapted from (47), Figure 3 H,I). (**a**) Calcium signals aligned to the initiation of feeding for AGRP and POMC neurons, changes in activity begin prior to the onset of feeding. (**b**) Quantification of change in fluorescence that occurs before feeding is initiated versus the total change in the trial.

Chapter 2

Functional properties of LH^{PV} neurons

2.1 Introduction

Survival behaviors such as feeding are regulated by the cooperative work of genetically-distinct neuronal populations scattered throughout the brain, particularly in the hypothalamic area (28, 33, 84). The hypothalamus contains a diverse collection of intermingled cell types defined by the expression of classical neurotransmitters and neuropeptides (85, 86). While extensive research has been done on hypothalamic neurons that express neuropeptides, such as agouti-related peptide (AGRP), pro-opiomelanocortin (POMC) (33, 47, 48, 87), hypocretin (orexin; HCRT), melanin-concentrating hormone (MCH) (88, 89), or on larger populations defined by neurotransmitter expression (*e.g.* vesicular GABA (γ-aminobutyric acid) transporter (*Vgat*) and vesicular glutamate transporter 2 (*Vglut2*)) (61), much less attention has been given to a small collection of neurons expressing the calcium-binding protein parvalbumin (PVALB; PV neurons) in the lateral hypothalamus (LH^{PV} neurons) (90, 91).

Throughout the central nervous system, PV-expressing neurons are typically GABAergic interneurons with fast-spiking characteristics (92). At the cellular and behavioral levels, these interneurons are necessary and sufficient for the generation of network oscillations in both the neocortex and hippocampus (65, 93). However, the fundamental electrophysiological properties, synaptic connections, and the functional roles of LH^{PV} neurons have remained largely uncharacterized. Here, we used a combination of selective targeting and manipulation of neuronal activity,

electrophysiology, and *in situ* hybridization to determine that LH^{PV} neurons embody a novel functional component within the LH.

2.2 Materials and methods

2.2.1 Animals

All experimental protocols were conducted in accordance with U.S. National Institutes of Health Guidelines for the Care and Use of Laboratory Animals and with the approval of the National Institute on Drug Abuse Animal Care and Use Committee. One to six-month-old male and female C57BL/6J (wild-type, Strain 664, The Jackson Laboratory, ME, USA), *Pvalb*^{IREScre} (C57BL/6 background, Strain 8069, The Jackson Laboratory), and *Pvalb*^{IREScre} crossed with *Rosa26*$^{LSL\text{-}tdTomato}$ (C57BL/6 background, Strain 7909, The Jackson Laboratory) mice were used in this study. Prior to stereotaxic viral injection, mice were group housed with littermates in temperature and humidity controlled rooms with *ad libitum* access to water and rodent chow (PicoLab Rodent Diet 20, 5053 tablet, LabDiet/Land O'Lakes Inc., MO, USA) on a 12 h light/dark cycle.

2.2.2 Stereotaxic viral injection

For brain slice electrophysiological recordings, two to five-month-old *Pvalb*^{IREScre} heterozygous mice were used. Mice were anesthetized with isoflurane and placed into a stereotaxic apparatus (David Kopf Instruments, CA, USA). After exposing the skull by a minor incision, small holes (< 1 mm diameter) were drilled bilaterally for virus injection. An adeno-associated virus (rAAV2/rh10-CAG-FLEX-*rev*-ChR2:tdTomato or rAAV2/1-CAG-FLEX-*rev*-CHR2:tdTomato; titer: 8.43×10^{12} genomic copies/ml and 6.86×10^{12} genomic copies/ml, respectively; University of Pennsylvania Gene Therapy Program Vector Core, PA, USA) (33) was injected bilaterally (50–100 nl; rate: 30 nl/min) into the lateral

hypothalamus (LH; bregma, −1.80 mm; midline, ±1.40 mm; dorsal surface, −5.4 mm) by a pulled glass pipette (20−30 μm tip diameter) with a micromanipulator (Narishige International USA Inc., NY, USA) controlling the injection speed. Subsequently, the incision was stitched, and mice were individually housed for 2−5 weeks for post-surgical recovery and viral transduction.

For mapping LH^{PV} axonal projections, 8-week-old *Pvalb*^{IREScre} heterozygous mice were bilaterally injected with 30 nl of an adeno-associated virus (rAAV2/9-hEF1α-DIO-hSyn-mCherry; titer: 1.0×10^{13} genomic copies/ml; Massachusetts Institute of Technology Viral Gene Transfer Core, Boston, MA, USA)(94) into the lateral hypothalamus as described above. After surgery, mice were individually housed for 6 weeks for post-surgical recovery and viral transduction.

2.2.3 Slice preparation and electrophysiology

After cervical dislocation, mice were decapitated and their brains were rapidly removed and placed into an ice-cold N-methyl-D-glucamine (NMDG)-based slicing solution (95) containing (in mM): 92 NMDG, 20 HEPES, 25 glucose, 30 $NaHCO_3$, 1.2 NaH_2PO_4, 2.5 KCl, 5 sodium ascorbate, 3 sodium pyruvate, 2 thiourea, 10 $MgSO_4$, and 0.5 $CaCl_2$, pH 7.4, and osmolarity of 304−308 mOsm. Acute horizontal brain slices (200−240 μm thick) containing the lateral hypothalamus were obtained using a vibratome (Leica VT1200, Leica Biosystems Inc., IL, USA). Brain slices were transferred to a holding chamber filled with a solution containing (in mM): 92 NaCl, 20 HEPES, 25 glucose, 30 $NaHCO_3$, 1.2 NaH_2PO_4, 2.5 KCl, 5 sodium ascorbate, 3 sodium pyruvate, 2 thiourea, 1 $MgSO_4$, and 2

$CaCl_2$ (pH 7.4, 304–308 mOsm). For electrophysiological recordings, a single slice was submerged in artificial cerebrospinal fluid (aCSF, in mM: 125 NaCl, 2.5 KCl, 1.25 NaH_2PO_4, 1 $MgCl_2$ $6H_2O$, 11 glucose, 26 $NaHCO_3$, 2.4 $CaCl_2$, pH 7.4, and osmolarity of 304–308 mOsm) in a recording chamber that was continuously perfused with a peristaltic pump (World Precision Instruments, FL, USA), at a flow rate of 1.5 to 2.0 ml/min. All solutions were saturated with 95% O_2 and 5% CO_2.

Characterization of the intrinsic electrophysiological properties of lateral hypothalamic parvalbumin (LH^{PV}) neurons was performed using *Pvalb*^{IREScre};*Rosa26*$^{LSL\text{-}tdTomato}$ mice (*Pvalb*$^{cre/+;}$*Rosa26*$^{tom/tom}$). Parvalbumin-tdTomato-positive lateral hypothalamic neurons were located in brain slices, first with epifluorescence, followed by infrared differential interference contrast (IR-DIC) optics, using an upright Olympus BX51WI microscope (Olympus Corporation, MA, USA). Whole-cell current-clamp recordings were performed using a MultiClamp 700B amplifier (5 kHz low-pass Bessel filter and 10 kHz digitization using a 1440A Digidata Digitizer) with pClamp 10.3 software (Molecular Devices LLC, CA, USA). Borosilicate glass patch pipettes (2.2–4.5 MΩ) containing (in mM): 135 potassium gluconate, 10 HEPES, 4 KCl, 4 MgATP, 0.3 Na_3GTP, and 0.2% biocytin (pH adjusted to 7.3 using KOH, and osmolarity of 290 mOsm). The holding potential was –70 mV and the whole-cell access resistances were ≤ 15 MΩ. All recordings were made at 32 °C.

For channelrhodopsin (ChR2)-assisted circuit mapping (CRACM) of neurons synaptically connected to LH^{PV} neurons, *Pvalb*^{IREScre} heterozygous mice were bilaterally injected with an adeno-associated virus into the LH as previously described. Horizontal

slices containing the LH from AAV-injected *Pvalb*^{IREScre} mice were used and ChR2:tdTomato-containing axons visualized in the LH. Whole-cell voltage-clamp recordings of LH neurons synaptically connected to LH^{PV} neurons were performed using patch pipettes (3.0–4.5 MΩ) containing (in mM): 117 cesium methanesulfonate, 20 HEPES, 0.4 EGTA, 2.8 NaCl, 5 TEA-Cl, 4 Mg-ATP, 0.4 Na-GTP, 3 QX-314, and 0.2% biocytin (pH adjusted to 7.3 using CsOH, and osmolality of 287 mOsm). Recorded cells were held at −70 mV and photocurrents were evoked by 1 ms blue (473 nm) light pulses (diode-pumped solid state laser; OptoEngine LLC, UT, USA) delivered at a frequency of 0.1 Hz. Series resistance (10–25 MΩ) was monitored with a −5 mV hyperpolarizing pulse given every 10 s, and only recordings that remained stable over the period of data collection were used. Light-evoked glutamatergic currents were blocked by perfusing the ionotropic glutamate receptor antagonist, 6,7-dinitroquinoxaline-2,3-dione (DNQX; 10 µM) and D-(-)-2-amino-5-phosphonopentanoic acid (D-AP5; 50 µM). The liquid junction potential for these measurements was not corrected. All recordings were made at 32 °C. All chemicals were obtained from Sigma-Aldrich (MO, USA) or Tocris Bioscience (Bristol, UK).

2.2.4 Electrophysiological analysis

Intrinsic membrane properties of LH^{PV} neurons were characterized in current-clamp configuration. Briefly, the resting membrane potential (V_{rmp}) and capacitance of the cell membrane (C_{mem}) were measured directly after obtaining whole-cell configuration. Both, the action potential (AP) and fast after-hyperpolarization (fAHP) amplitudes were determined relative to the AP threshold (*i.e.* membrane potential (V_m) at which dV_m/dt

first reached 20 V/s). The fAHP latency was determined as the time difference between the AP threshold level and the largest fAHP peak. The AP properties were determined by applying a 500 ms depolarizing current steps in a range of 20–100 pA in 20 pA increments. The respective AP parameters were determined from the first evoked AP. Both the action potential (AP) and fast after-hyperpolarization (fAHP) amplitudes were determined relative to the AP threshold (*i.e.* membrane potential (V_m) at which dV_m/dt first reached 20 V/s). The fAHP latency was determined as the time difference between the AP threshold level and the largest fAHP peak. AP latency was measured as the time difference between the current onset time and the time when the AP peak was reached, while the AP half-width (HW) was determined as the halfway duration between AP peak and the AP threshold level. AP broadening was measured at twice current amplitude of the first evoked AP and calculated according to (HW2 – HW1)/HW1, where HW1 and HW2 correspond to the HW of the first and second APs, respectively. Further membrane properties and firing rate were determined by applying 500 ms current step injections ranging from –100 pA to 1500 pA in 20–50 pA increments. Input resistance (R_{in}) was calculated from the slope of a linear regression fit to the steady-state voltage-current relation using a range of hyperpolarizing current steps. The membrane time constant (τ) was determined by single exponential fit to the rising phase of a mean voltage response to a –100 pA current step. The sag ratio was determined according to V_{steady}/V_{hyp}, where V_{steady} and V_{hyp} correspond to the voltage response measured at the end of a –100 pA hyperpolarizing current step and the hyperpolarization peak, respectively. The maximal

firing frequency was determined as the spike frequency response to the largest depolarizing current step (500 ms) below that where AP failures were observed.

To generate the *I–f* curves, we measured the firing rate by counting the number of spikes elicited in response to step depolarizing current injections during a 500 ms window. Note that each neuron was tested for a subset of current amplitudes from 0 – 1200 pA.

2.2.5 Immunohistochemistry

Mice were deeply anesthetized with isoflurane and transcardially perfused with phosphate buffered saline (1× PBS) followed by 4% paraformaldehyde (PFA) in 1× PBS. Whole brains were removed and post-fixed in 4% PFA for 2–4 h at 4 °C and subsequently transferred to 1× PBS for storage at 4 °C. Horizontal brain sections (50–70 µm thick) containing the LH were collected in 1× PBS using a vibrating tissue slicer (vibratome; Leica VT1200), and freely floating slices were immunostained for parvalbumin. First, slices were incubated in a solution of 1× PBS/0.3% Triton X-100 with 10% normal donkey serum (NDS) for 1 h at room temperature. Slices were then incubated with rabbit anti-parvalbumin antibody (1:500 PV25 or PV27; Swant, Marly, Switzerland) in a solution of 1× PBS/0.3% Triton X-100/2% NDS for 14–18 h at 4 °C. Slices were washed in 1× PBS (4 × 10 min each) and then incubated for 3 h with secondary antibody (1:500 donkey anti-rabbit-AlexaFluor 488 or AlexaFluor 647, Invitrogen, CA, USA) in 1× PBS/0.3% Triton X-100/2% NDS at room temperature. Following PBS washes (4 × 10 min each), slices were mounted onto

Superfrost Plus glass slides (VWR International, PA, USA) and coverslipped with DAPI-Fluoromount-G aqueous mounting medium (Electron Microscopy Sciences, PA, USA).

Images were taken with an AxioZoom.V16 fluorescence microscope and z-stacks were collected using an LSM700 laser scanning confocal microscope (Carl Zeiss Microscopy LLC, NY, USA). Stacks were imported into Vaa3D 3D visualization-assisted analysis software (96), and fluorescent neurons were counted bilaterally from every section. Mice used for anterograde tracing were perfused 6 weeks after infection, brains were sliced and signal was enhanced by immunostaining for mCherry (rabbit anti-DsRed).

2.2.6 Fluorescent *in situ* hybridization

Following cervical dislocation, wildtype mice were decapitated, and brains were dissected and rapidly frozen in −80 °C isopentane then subsequently stored at −80 °C. Horizontal cryosections (16 µm) containing the lateral hypothalamus were sliced using a Leica CM3050 S cryostat (Leica Biosystems Inc.) and sections collected onto Superfrost Plus glass slides (VWR International). Slides were stored at −80 °C prior to processing. Fluorescent *in situ* hybridization was performed using the RNAscope® Multiplex Fluorescent Assay for fresh frozen tissue (Advanced Cell Diagnostics Inc., CA, USA). Briefly, sections were fixed in 4% PFA in PBS, dehydrated by ethanol series, and treated with Protease IV. Sections were incubated with target probes for mouse parvalbumin (*Pvalb*, accession number NM_013645.3, target region aa2-885), vesicular glutamate transporter 2 (*Slc17a6 (Vglut2)*, accession number NM_080853.3, target region aa1986-2998), and vesicular GABA transporter (*Slc32a1 (Vgat)*, accession number NM_009508.2, target

region aa894-2037). After hybridization, a series of signal amplification steps (Amp1, Amp2, and Amp3) were performed per kit protocol followed by incubation with labels (Amp4B) for fluorescent visualization of each probe: *Pvalb* (Alexa488), *Vglut2* (Atto550), and *Vgat* (Atto647). Slides were counterstained with DAPI and coverslipped with Fluoromount-G aqueous mounting medium (Electron Microscopy Systems). Z-stack images were obtained using an LSM700 confocal microscope (Carl Zeiss Microscopy). LH^{PV} neurons were manually assessed for co-expression of *Pvalb* with *Vglut2* or *Vgat*.

2.2.7 Radioactive *in situ* hybridization and immunohistochemistry

Wildtype mice were deeply anesthetized with isoflurane and transcardially perfused with 0.1 M phosphate buffer (PB) followed by 4% PFA in 0.1 M PB. Whole brains were removed and post-fixed in 4% PFA/PB for 2 h at 4 °C. Samples were washed with 0.1 M PB (2 × 30 min each) at 4 °C, and then transferred to 18% sucrose in 0.1 M PB. Free-floating coronal cryosections (14 µm) were sliced using a Leica CM3050 S cryostat. *In situ* hybridization was performed as previously detailed (97, 98). Steps are at room temperature unless otherwise noted. Sections were incubated for 3 × 10 min in 0.1 M PB/0.5% Triton X-100, rinsed with 0.1 M PB (3 × 10 min), treated with 0.2 N HCl for 15 min, rinsed with 0.1 M PB (3 × 10 min), and then acetylated in 0.25% acetic anhydride/0.1 M triethanolamine pH 8.0 for 10 min. Sections were rinsed for 3 × 10 min with 0.1 M PB, fixed with 4% PFA/PB for 10 min, washed again with 0.1 M PB (3 × 10 min), and then prehybridized for 2 h at 55 °C. Sections were hybridized for 16 h at 55 °C with [^{35}S]- and [^{33}P]-labeled (10^7 c.p.m./ml) antisense probe for either *Vglut2* (nucleotides 317-2357;

Accession Number NM_053427) or *Vgat* (nucleotides 1-2814, Accession Number BC052020). After hybridization, sections were incubated in 2× SSC buffer/10 mM β-mercaptoethanol (BME) for 30 min at room temperature. Sections were next treated with 5 µg/ml RNase A in 10 mM Tris-HCl pH 7.9/10 mM NaCl/0.1 mM EDTA for 1 h at 37 °C, washed in 0.5× SSC/50% formamide/10 mM BME/0.5% sarkosyl for 2 h at 55 °C, washed in 0.1× SSC/10 mM BME/0.5% sarkosyl for 1 h at 60 °C, and rinsed with 0.1 M PB (3× 10 min) prior to parvalbumin immunolabeling.

For immunohistochemistry, sections were blocked with 0.1 M PB/4% bovine serum albumin (BSA)/3% Triton X-100 for 1 h. Sections were incubated with goat anti-parvalbumin antibody (1:1000 PVG-213, Swant) in block solution overnight at 4 °C. After washing with 0.1 M PB (3 × 10 min), sections were incubated with biotinylated anti-goat IgG secondary antibody (1:200) in block solution, washed with 0.1 M PB (3 × 10 min), incubated for 1 h in avidin-biotinylated horseradish peroxidase (1:200, ABC kit; Vector Laboratories, CA, USA), rinsed with 0.1 M PB (3 × 10 min), and developed with 0.05% 3,3-diaminobenzidine-4 HCl (DAB)/0.003% hydrogen peroxide/0.1 M PB for 10 min. Sections were washed with 0.1 M PB (3 × 10 min), mounted onto coated slides, dipped in Ilford K5 nuclear tract emulsion (Harman Technology Ltd, TX, USA), and exposed in the dark at 4 °C for four weeks prior to development.

Sections were imaged with brightfield and epiluminescence microscopy using a Leica DMR microscope with a 20× objective and cellSens Standard v1.11 software (Olympus Corporation). Neurons observed within the LH^{PV} region were manually assessed for the co-expression of *Vglut2* mRNA or *Vgat* mRNA with anti-parvalbumin

immunolabeled cells. Brightfield was used to determine whether a parvalbumin-immunolabeled (brown DAB product) neuron contained the aggregates of silver grains for *Vglut2* mRNA or *Vgat* mRNA, which were viewed under epiluminescence.

2.2.8 Single-cell gene expression profiling and analysis

Single-cell cytoplasm harvesting was performed as previously described (99). Brain slices were prepared from *Pvalb*$^{cre/+}$*;Rosa26*$^{tom/tom}$ mice as described above. First, the fast-spiking firing pattern of a LH^{PV} tdTomato-positive neuron was recorded during whole-cell configuration. Subsequently, the cytoplasm of the recorded neuron was harvested into the recording pipette. The stability of the gigaseal (*i.e.* seal between the neuron and the pipette) was constantly monitored to avoid extracellular contamination. The total recording time and harvesting of the intracellular content did not exceed more than 4 min. The content of the pipette tip containing the harvested cytoplasm was then expelled into an RNase-free PCR tube. For positive control samples, we patched fast-spiking parvalbumin-expressing (tdTomato-positive) basket cells in the hippocampus and performed the same procedure as described above.

Single-cell extracts were processed using the Ambion® Single Cell-to-CT Kit (Thermo Fisher Scientific, MA, USA). Briefly, samples were incubated in lysis solution with DNase I. Reverse transcription was then performed followed by preamplification of all target genes using pooled TaqMan Gene Expression Assays (Thermo Fisher Scientific). Target genes in LH^{PV} cells were detected using the recommended best coverage assays for *Pvalb* (Mm00443100_m1), *Slc17a6* (*Vglut2*, Mm00499876_m1), *Slc32a1* (*Vgat*,

Mm00494138_m1), *Kcnc1* (*Kv3.1*, Mm00657708_m1), *Kcnc2* (*Kv3.2*, Mm01234232_m1), and *Hcn2* (Mm00468538_m1). qPCR was performed in 10 µl reactions in 96-well plates using an Applied Biosystems 7500 Fast Real-Time PCR System (Invitrogen, CA, USA) with the following cycling parameters: (1) 50 °C for 2 min, (2) 95 °C for 10 min, and (3) 40 repeats of 95 °C for 15 s, 60 °C for 1 min. Reactions included TaqMan Gene Expression Master Mix, TaqMan probe, and cDNA according to manufacturer's protocol (Thermo Fisher Scientific). Each plate was run with a negative control (no cDNA template) and a positive control (hippocampal basket cell positive for *Pvalb*, *Vgat*, *Kv3.1*, *Kv3.2*, and *Hcn2*). Technical replicates (triplicate) were performed for each sample-gene combination. Cycle threshold (Ct) values were determined using Applied Biosystems 7500 v2.0.6 software (Invitrogen). Amplification Ct values higher than 37 and samples lacking any amplification curves were designated below the limit of detection. Three out of eight LH^{PV} cells lacked amplification curves for *Kv3.2*. These samples were excluded from the *Kv3.2* analysis. For all other target genes, n = 8 cells. Gene expression was normalized to *Pvalb* and *Vglut2* using the $2^{-\Delta\Delta Ct}$ method (100).

2.2.9 Statistical analysis

Data are reported as mean ± s.e.m. or mean ± s.d. unless otherwise noted. Individual data points are shown for qPCR. Statistical analyses were performed using the Analysis ToolPak of Microsoft *Excel* 2016 (Microsoft Corporation, WA, USA). Statistical significance (*P* values) for paired comparisons was determined by two-tailed Student's *t* test ($P < 0.05$ considered statistically significant). Statistical tests, *n* values for number of animals or

number of cells, exact *P* values, degrees of freedom and *t* values are reported in figure legends where pertinent. Data were assumed to have a normal distribution; however, this was not formally tested. No statistical methods were used to determine sample sizes, but sample sizes used are similar to other publications (101, 102). Experimenters were not blinded to groups. Data from electrophysiological recordings were analyzed with Clampfit v10.6 (Molecular Devices LLC, CA, USA), Origin Pro v9.2 (OriginLab Corporation, MA, USA) and MATLAB R2015A (The MathWorks Inc., MA, USA).

2.3 Results

2.3.1 Anatomical and electrophysiological characteristics of LH^{PV} neurons

We first characterized the electrophysiological properties of LH^{PV} neurons under current-clamp conditions. These neurons form a compact and small cluster in the LH medial to the optic tract (340 ± 10 neurons, n = 3 mice; bilateral; (**Figure 5**) and the number of cells was consistent with previous studies estimating ~400 PV-immunoreactive neurons in the LH of mice (91). We performed whole-cell recordings from LH^{PV} neurons (n = 34) identified by tdTomato fluorescence in brain slices sectioned horizontally from *Pvalb*^{IREScre};*Rosa26*$^{LSL\text{-}tdTomato}$ mice. We observed that these neurons fired action potentials at high-frequency and with little accommodation in response to depolarizing current injections (**Figure 6a**). This fast-spiking action potential phenotype and other electrophysiological characteristics such as the resting membrane potential (V_{rmp}), action potential half-width (AP_{HW}), and the maximal firing frequency (**Table 1**) are similar to the properties of both hippocampal and neocortical PV-positive GABAergic interneurons (65, 93).

2.3.2 LH^{PV} neurons are equipped with ion channels that support their fast-spiking phenotype

Previous studies showed that fast-spiking interneurons can be characterized by the expression of a specific combination of ion channels that confer these electrophysiological properties as, for example, delayed rectifier voltage-gated potassium

channels (KV3.1 and KV3.2) and the hyperpolarization-activated cation channels (HCN) (92). Therefore, we sought to determine whether the expression of these channels is similar in LH^{PV} neurons. Single-cell RT-qPCR analysis revealed that LH^{PV} neurons express *Kv3.1*, *Kv3.2*, and *Hcn2* subunit genes with comparable relative abundance (**Figure 7a,b**).

Together, these results demonstrate that LH^{PV} neurons are equipped with ion channels that are implicated in setting precise pacing of spiking activity to minimize accommodation during prolonged depolarization, with some electrophysiological diversity (**Figures 8a,b**) possibly attributed to the variations in the relative contributions of specific ion channels.

2.3.3 LH^{PV} neurons are glutamatergic

Thus far, our results indicate that LH^{PV} neurons have many common features with inhibitory interneurons. Therefore, we predicted that these neurons may comprise a lateral hypothalamic inhibitory circuit that may be involved in the orchestration of appetitive and consummatory behaviors. To test this, we first sought to determine whether LH^{PV} neurons are GABAergic. Surprisingly, a previous study has shown that parvalbumin can be found colocalized with glutamate immunohistochemically in both, rats and mouse (91). However, a quantification of the number of LH^{PV} neurons expressing specific markers for glutamate and their ability to release the neurotransmitter and form functional synapses have not been determined.

Therefore, we used several convergent approaches to unravel the neurotransmitter system used by LH^{PV} neurons. We first performed channelrhodopsin

(ChR2)-assisted circuit mapping (CRACM) to examine whether LH^{PV} neurons are synaptically connected to other cells within the LH (**Figure 6b**, (40, 103). We stereotaxically injected a Cre recombinase-dependent viral vector (40) bilaterally into the LH of *Pvalb*^{IREScre} transgenic mice to target channelrhodopsin-2 (ChR2) fused to the fluorophore tdTomato (ChR2:tdTomato) specifically to LH^{PV} neurons. We performed whole-cell recordings from individual neurons within the LH (*n* = 75) under voltage-clamp configuration (**Figure 6b**) and observed that photostimulation of ChR2-expressing LH^{PV} neurons and axons evoked excitatory postsynaptic currents (EPSCs; 69.0 ± 5.0 pA) on the connected LH neurons (*n* = 13; 17.33 % connected). Those EPSCs were blocked by selective antagonists of glutamate receptors (2.5 ± 0.4 pA). This demonstrates that rather than releasing GABA, LH^{PV} neurons release the excitatory neurotransmitter glutamate.

To determine whether LH^{PV} neurons contained markers of glutamate or GABA neurons, we performed in situ hybridization assays to measure the expression of *Slc17a6* (*Vglut2*; vesicular glutamate transporter 2) and *Slc32a1* (*Vgat*; vesicular GABA transporter) in these neurons (**Figure 9** and **Figure 10a-b**). We observed that *Pvalb* mRNA was predominantly detected in neurons that express *Vglut2* (95 % *Pvalb*$^{+}$*/Vglut2*$^{+}$; 5 % *Pvalb*$^{+}$*/Vgat*$^{+}$; *n* = 4). Together, these results describe a cluster of glutamatergic fast-spiking LH^{PV} neurons that provide excitatory inputs to neuronal circuits within the LH.

2.3.4 LH^{PV} neurons send long range projections throughout the brain

Previously, a Cre recombinase-dependent anterograde viral vector approach to labeling LH^{PV} neurons has been employed. Projections were seen in many areas

throughout the brain, with the strongest pathway in the PAG, but this approach does not distinguish between fibers of passage and synaptic terminals (52). We stereotaxically injected a Cre recombinase-dependent viral vector that expresses synaptophysin fused to mCherry bilaterally into the LH of *Pvalb*^{IREScre} transgenic mice. This approach allowed us to selectively label axon terminals of LH^{PV} neurons throughout the brain. We identified terminals in the LHb, parafascicular thalamic nucleus (PF) surrounding the retroflex fascicle (fr), submedius thalamic nucleus (Sub), PAG, reticulotegmental nucleus of the pons (RtTg), posterior hypothalamus (PH) and retromamillary nucleus (RMM) (**Figure 11**). These findings confirm several of the proposed projection sites seen by Celio *et al.* including the PAG, LHb, and PF (52).

2.4 Figures and tables

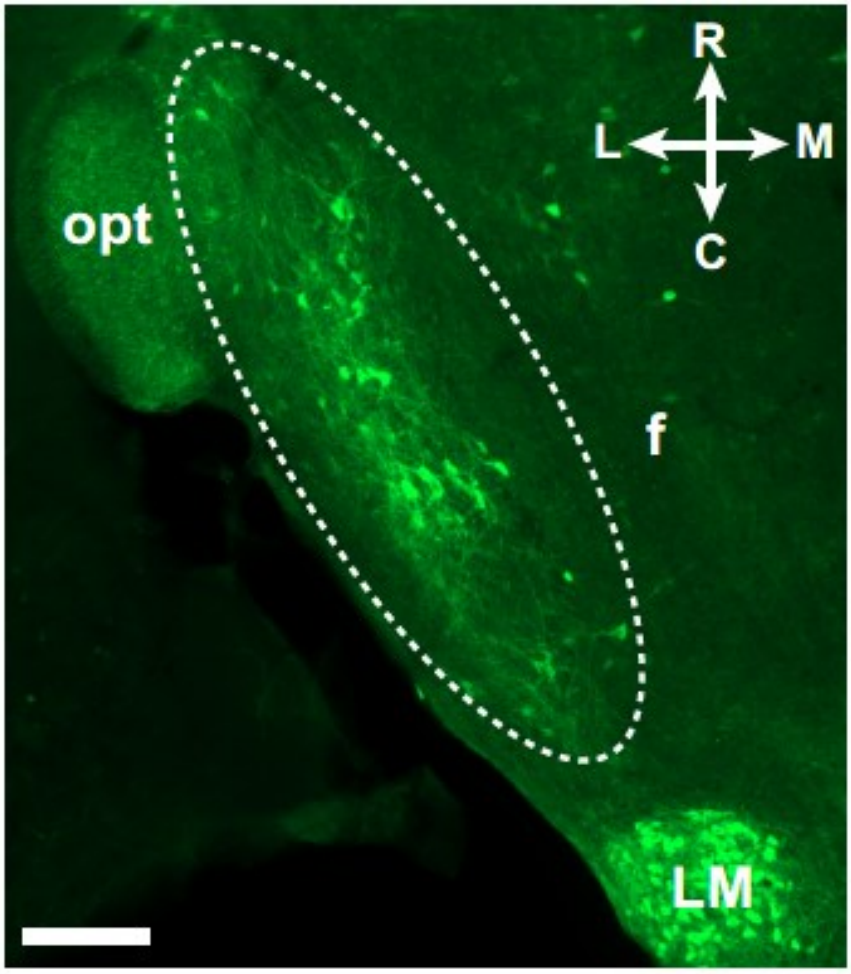

Figure 5

Immunohistochemical identification of parvalbumin-expressing neurons in a horizontal section of the mouse LH. Dotted lines highlight a cluster of immuno-positive LH^{PV} neurons (green). Scale bar = 200 μm. Abbreviations, fornix (f), optic tract (opt), lateral mammillary nucleus (LM), lateral (L), medial (M), rostral (R), and caudal (C).

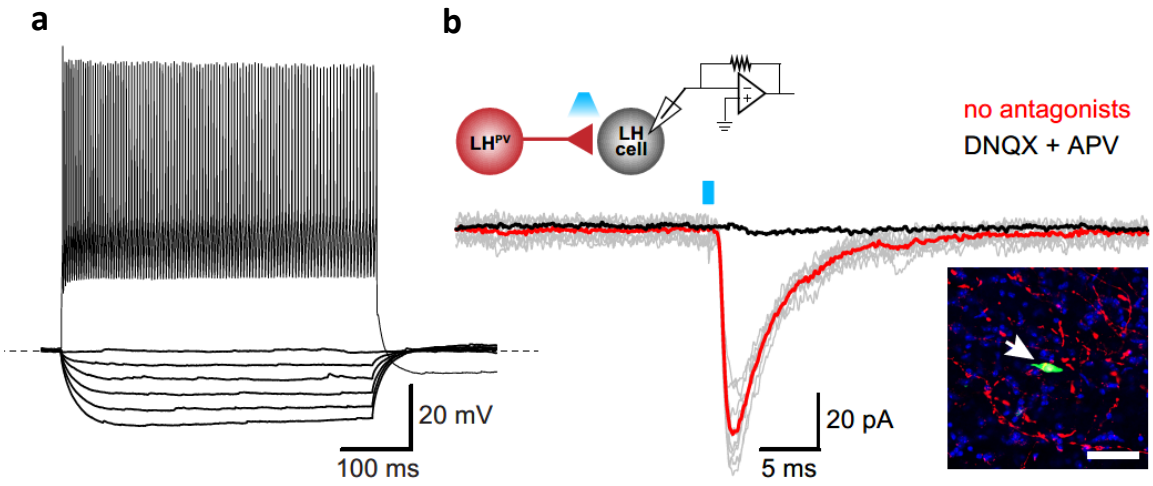

Figure 6

LH^{PV} neurons exhibit fast-spiking characteristics and provide excitatory input to neurons within the LH. (**a**) Representative traces and firing pattern of a fast-spiking LH^{PV} neuron in response to step hyperpolarizing (bottom traces; from −100 to 0 pA) and depolarizing current injections (upper traces; 900 pA) during a 500 ms pulse. Resting membrane potential (V_{rmp} = −66 mV) and maximal firing frequency 264 Hz. (**b**) Traces of excitatory postsynaptic currents (EPSCs; gray) evoked by photostimulation (1 ms light pulses) of LH^{PV}-ChR2^{+} neurons before and after bath application of DNQX and APV (black trace; AMPA-R and NMDA-R antagonists). Red and black traces are the average of ten consecutive sweeps. LH neuron was held at −70 mV. Note schematic of ChR2-assisted circuit mapping (inset; upper left) from LH^{PV}-ChR2^{+} neuron (red) onto a postsynaptic lateral hypothalamic neuron (gray) as well as arrow indicating the recorded postsynaptic LH neuron (inset; bottom right) filled with biocytin (green) surrounded by ChR2:tdTomato-expressing LH^{PV} axons (red). Scale bar = 50 µm.

Electrophysiological Property	
V_{rmp} (mV)	−65.6 ± 1.2
C_{mem} (pF)	40.2 ± 2.5
R_{in} (MΩ)	327.3 ± 29.6
τ_m (ms)	21.3 ± 1.8
Sag ratio	0.96 ± 0.004
AP threshold (mV)	−40.5 ± 1.1
AP latency (ms)	49.5 ± 6.7
AP amplitude (mV)	63.4 ± 1.3
AP_{HW} (ms)	0.45 ± 0.02
fAHP amplitude (mV)	21.9 ± 0.8
fAHP latency (ms)	1.97 ± 0.13
AP broadening	0.06 ± 0.01
Maximal firing frequency (Hz)	193.6 ± 10.3

Table 1

Electrophysiological properties of LH^{PV} neurons. Data are reported as mean ± S.E.M. Descriptions of electrophysiological properties are explained in Materials and Methods

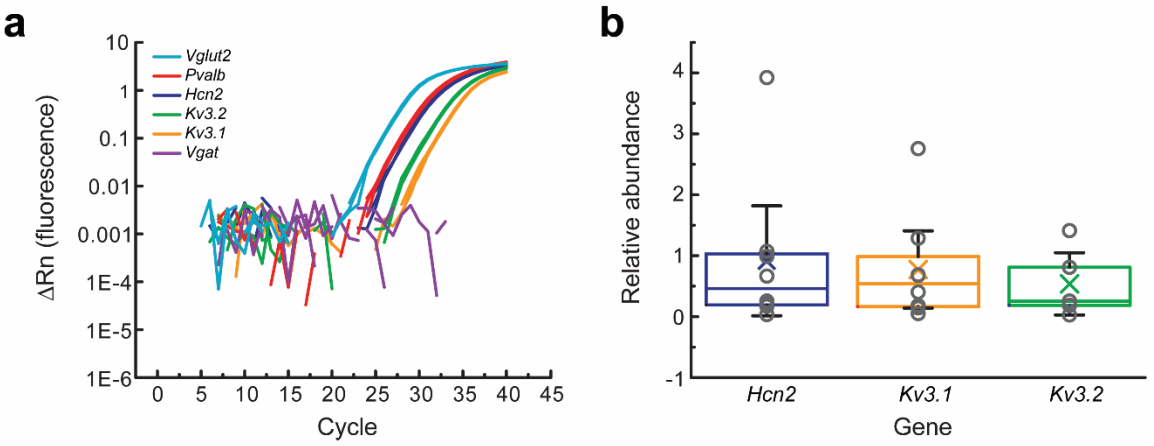

Figure 7

LH^{PV} neurons express KV3 and HCN channels. (**a**) Detection of *Kv3.1*, *Kv3.2*, and *Hcn2* subunit genes by RT-qPCR analysis after harvesting the cytoplasm from single LH^{PV} neurons. (**b**) Relative abundance of *Kv3.1*, *Kv3.2*, and *Hcn2* in single LH^{PV} neurons. Box plots show mean (×), median, quartiles (boxes), and s.e.m. (whiskers). Circles indicate data from individual cells. Cycle threshold (Ct), relative abundance values, and sample sizes are explained in Materials and Methods.

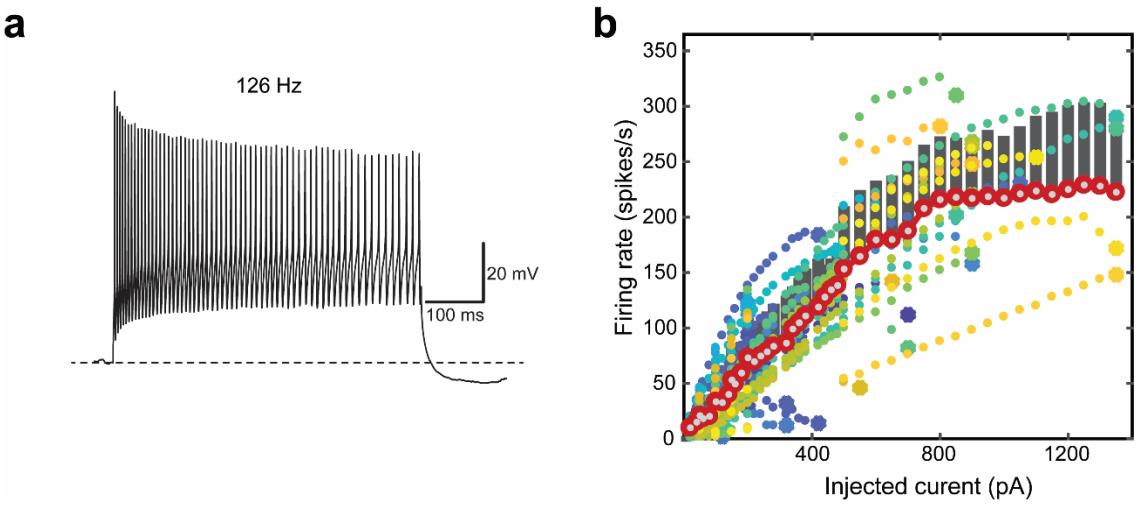

Figure 8

Characterization of firing rates of LH^{PV} neurons in response to current injections. (**a**) Representative firing pattern of a fast-spiking LH^{PV} neuron that displays spike frequency and amplitude accommodation during large depolarizing current injections (500 pA, 500 ms pulses). Note firing frequency and amplitude accommodation during the last 100 ms of the pulse. Resting membrane potential (V_{rmp} = −63 mV). (**b**) Firing rate of LH^{PV} neurons in response to current injection (*I–f* curves) during 500 ms pulses. Each recorded neuron is color coded (*n* = 34). The red/gray dots show the average firing rate of the LH^{PV} neurons and the standard deviation is indicated by the black vertical bar. The bigger dots depict the maximum current that can be injected on each neuron before they fall into depolarization block. These neurons display diversity in their *I–f* curves, which monotonically decrease as the output firing rate increases (data not shown).

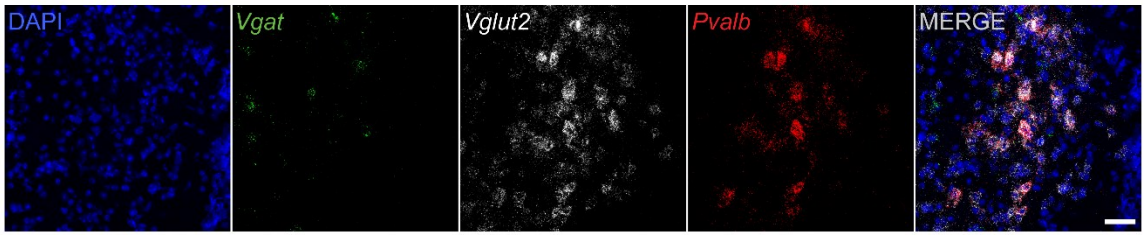

Figure 9

Fluorescent *in situ* hybridization assay for *Vgat* (green), *Vglut2* (red), and *Pvalb* (white) with DAPI (blue) counterstain. *Pvalb* mRNA was predominantly detected in neurons that express *Vglut2* (95 % *Pvalb*$^{+}$*/Vglut2*$^{+}$*;* 5% *Pvalb*$^{+}$*/Vgat*$^{+}$) Scale bar, 50 µm. Abbreviations, fornix (f), optic tract (opt), lateral mammillary nucleus (LM), lateral (L), medial (M), rostral (R), and caudal (C).

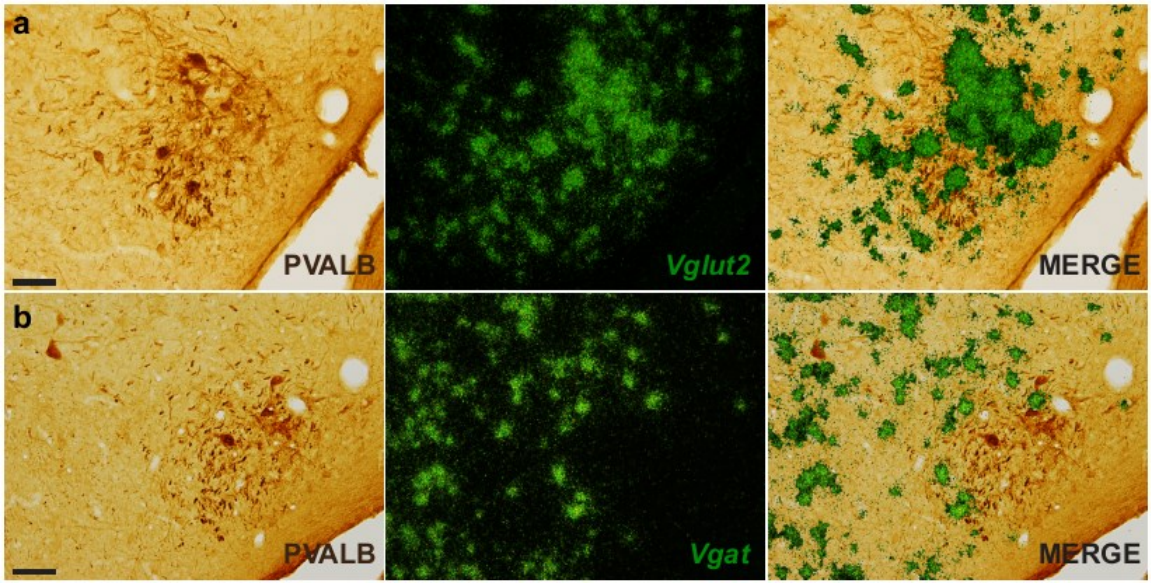

Figure 10

LH^{PV} neurons are *Vglut2*-positive. (**a**) Coronal sections showing that parvalbumin immunoreactive cells (brown; left panel) mainly colocalize with *Vglut2* mRNA (95 %; green grain aggregates; right panel) but (**b**) not with *Vgat* mRNA (5 %; green grain aggregates; right panel). Scale bars = 50 µm.

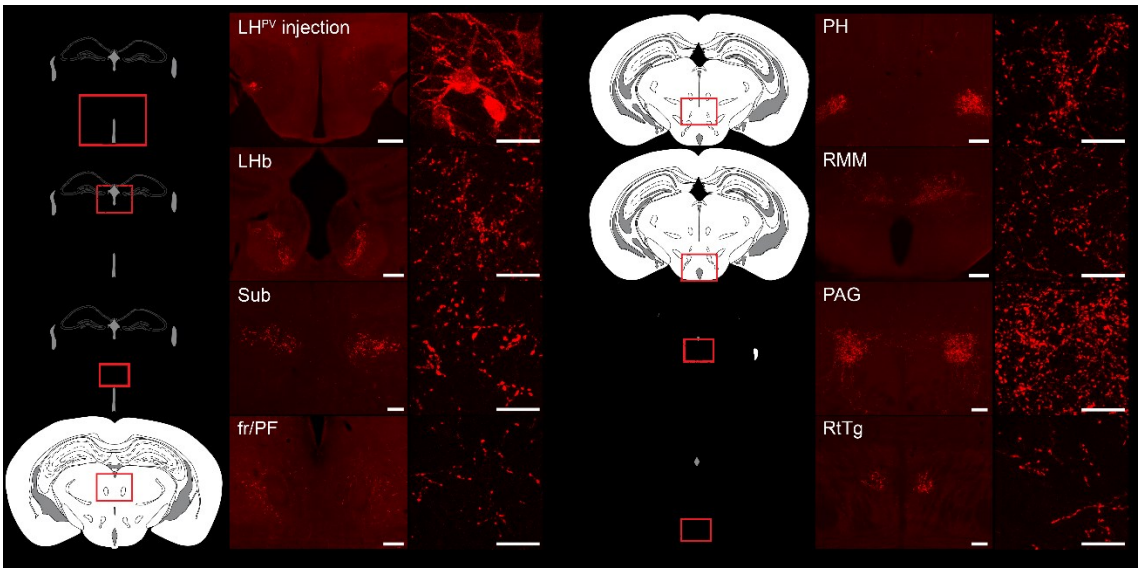

Figure 11

Axonal projections of LH^{PV} neurons. (**a**) Schematic and representative image depicting a bilateral injection of the Cre recombinase-dependent viral vector for anterograde tracing (rAAV2/9-hEf1α-DIO-synaptophysin-mCherry) into the lateral hypothalamus (LH) of a *Pvalb*^{IREScre} mouse. Scale bar 500 µm. Projections to (**b**) the lateral habenula (LHb), (**c**) the submedius thalamic nucleus (Sub), (**d**) the parafascicular thalamic nucleus (PF) surrounding the fasciculus retroflexus (fr), (**e**) the posterior hypothalamus (PH), (**f**) the retromamillary nucleus (RMM), (**g**) the periaqueductal gray (PAG), and (**h**) the reticulotegmental nucleus of the pons (RtTg). (**b-d-e-f**) Scale bars (low magnification), 200 µm; Scale bars (high magnification), 25 µm (**c-g-h**) Scale bars (low magnification), 100 µm; Scale bars (high magnification), 25 µm. (*n* = 3 mice)

Chapter 3

LH^{PV} neurons regulate feeding and general arousal

3.1 Introduction

To further investigate the functional roles of LH^{PV} neurons *in vivo* and during behavior, we tested whether these neurons regulate feeding by manipulating their activity using a chemogenetic approach. Pioneering experiments have shown that the lateral hypothalamus is predominantly known to regulate food and water intake, arousal, mating, circadian rhythm, body temperature, and reward. Early experiments using electrical self-stimulation of the LH showed that mice would perform work (*i.e*. press a lever) to receive electrical stimulation in the LH, which induced voracious feeding, demonstrating the rewarding effects of LH-induced feeding (104, 105). Meanwhile, electrolytic lesions drive a hypophagic response (15). The LH comprises a multitude of different cell types and fiber pathways, distinguished by expression of different molecular markers. Both glutamatergic and GABAergic neurons are found within the LH. Injection of glutamate receptor agonists as well as direct optogenetic stimulation of LH GABAergic (inhibitory) neurons have been shown to drive food intake (hyperphagia), yet both injection of GABA receptor agonists and optogenetic stimulation of LH glutamatergic (excitatory) neurons have been shown to decrease food intake (hypophagia) (61, 64, 106-108). More specific markers than just expression of GABA and glutamate or their receptors will be necessary to identify the subpopulations of neurons in the LH that drive different aspects of feeding behaviors.

Here I used a chemogenetic approach to specifically excite and inhibit LH^{PV} neurons. We found that inhibition of those neurons in sated mice during the light phase significantly increased food intake by 60% demonstrating that LH^{PV} neurons play a role

in regulating feeding. Additionally, we found that such inhibition also significantly increased general arousal by 44% over the course of the experiment.

3.2 Materials and methods

3.2.1 Stereotaxic viral injection

For behavioral experiments, four to twelve-week-old *Pvalb*^{IREScre} heterozygous mice were used. Mice were anesthetized with isoflurane and placed into a stereotaxic apparatus (David Kopf Instruments, CA, USA). After exposing the skull by a minor incision, small holes (< 1 mm diameter) were drilled bilaterally for virus injection. An adeno-associated virus (rAAV2/rh10-hSyn-DIO-hM3D(Gq):mCherry, rAAV2/rh10-hSyn-DIO-hM4D(Gi):mCherry; titer: 3×10^{12} virus molecules/ml each virus; University of North Carolina Vector Core, NC, USA or rAAV2/9-CAG-FLEX-*rev*-eGFP-WPRE-bGH; titer: 2.28×10^{13} GC/ml; University of Pennsylvania Gene Therapy Program Vector Core, PA, USA) (34) was injected into the lateral hypothalamus (LH; bregma, −1.80 mm; midline, ±1.40 mm; dorsal surface, −5.4 mm) by a pulled glass pipette (20−30 μm tip diameter) with a micromanipulator (Narishige International USA Inc., NY, USA) controlling the injection speed. Subsequently, the incision was stitched, and mice were individually housed for 2−5 weeks for post-surgical recovery and viral transduction.

3.2.2 Behavioral experiments

3.2.2.1 Feeding assay

Male and female *Pvalb*^{IREScre} heterozygous mice injected with either hM4D, hM3D, or GFP control virus in LH^{PV} neurons were given *ad libitum* access to rodent chow (PicoLab Rodent Diet 20, 5053 tablet, LabDiet/Land O'Lakes Inc., MO, USA) in home cages prior to

testing. For behavioral testing, mice were transferred to experimental cages with automatic food pellet dispensers (Coulbourn Instruments LLC, PA, USA) and supplied with pellets (20 mg each) of identical composition to the food in the home cage. Pellet removal was sensed by the offset of a beam break, and an additional pellet was administered after a delay (10 s). Water was available *ad libitum* during the experiment and water spout licks were sensed by optical detection (Coulbourn Instruments). Both food consumption and water spout licks were monitored continuously using Graphic State v4 software (Coulbourn Instruments). In addition, water bottles were manually weighed every 24 h to quantify water intake. Mice were acclimated to experimental cages for 2–3 days before initiating experimental protocols.

Mice were tested for evoked food and water intake during both light and dark periods (lights on at 7:00 a.m. and off at 7:00 p.m.). Light period testing began at 9:00 a.m., 2 h following light onset, and dark period testing began at 7:00 p.m. Food intake was recorded continuously for 24 h following control (sterile water) or 3.0 mg/kg clozapine-N-oxide (CNO) intraperitoneal (i.p.) injection on two consecutive days. CNO or water was injected 5–10 min before the start of the experiment. The order of water and CNO injection days was counterbalanced between mice. During an additional set of experiments, male and female *Pvalb*^{IREScre} heterozygous mice injected with hM3D virus in LH^{PV} neurons were food deprived for 10 h during light phase (9:00 a.m.–7:00 p.m.) before testing for chemogenetic excitation to further increase their drive to eat during the dark cycle. Access to food was introduced *ad libitum* from 7:00 p.m. until 9:00 a.m. Mice were i.p. injected 5–10 min prior to the onset of dark phase with either control (sterile water)

or 3.0 mg/kg CNO. Activity was recorded and tracked for 4 h following injections using ANY-maze behavior tracking software version 4.9 (Stoelting Co., IL, USA).

A separate group of *Pvalb*^{IREScre} mice (LH$^{PV/GFP}$) served as a control population for behavioral effects of CNO injection. These mice were bilaterally injected with a Cre recombinase-dependent viral vector that drives the expression of green fluorescent protein (GFP). The hyperphagic effects upon inhibition of LH^{PV} neurons were not a side effect of CNO, as injection of CNO did not induce a significant change in food intake in LH$^{PV/GFP}$ mice during light phase or dark phase (**Figure 16**). General arousal (measured as time spent mobile, including grooming and locomotion) was significantly decreased following injection of CNO in sated mice during the light cycle (**Figure 17a-c**, **P* =0.0483). General arousal was not altered following injections of CNO in sated or fasted mice during the dark cycle (**Figure 17d-i**). Thus, we did not observe a sedative-like behavior after CNO administration in any of the cohorts (*i.e.* LH$^{PV/hM3D}$, LH$^{PV/hM4D}$, and LH$^{PV/GFP}$ mice) as reported by a recent study (109).

3.2.3 Histology and immunohistochemistry for behavior animals

Mice were deeply anesthetized with isoflurane and transcardially perfused with 1× PBS followed by 4% PFA in 1× PBS. Whole brains were removed and post-fixed in 4% PFA/PBS for 2 h at 4 °C and subsequently transferred to 1× PBS for 1 to 48 h for storage at 4 °C until further processing. Coronal brain sections (50 µm thick) containing the LH were collected in 1× PBS using a vibrating tissue slicer (vibratome; Leica VT1200), and freely floating slices were immunostained for parvalbumin (PVALB) and RFP. Sections

were incubated with a blocking solution of 1× PBS/0.2% Triton X-100 (PBT) plus 2–5% normal donkey serum (NDS) for 1 h. Sections were then incubated with the primary antibodies (rabbit anti-PVALB, 1:500 PV25; Swant) and guinea pig anti-RFP, 1:40,000 (gift from J.N. Betley, University of Pennsylvania, PA, USA) (39) in PBT/2% NDS overnight at 4 °C. After rinsing 4 × 10 min in 1× PBS, sections were incubated for 2 h with secondary antibodies donkey anti-rabbit-Alexa Fluor 647 (1:500; Invitrogen, CA, USA) and donkey anti-guinea pig-Alexa Fluor 488 (1:500; Jackson ImmunoResearch Inc., PA, USA) in PBT/2% NDS at room temperature and washed with 1× PBS (4 × 10 min). Sections were mounted with DAPI-Fluoromount-G aqueous mounting medium (Electron Microscopy Sciences) onto Superfrost Plus glass slides (VWR International). Images were taken with an AxioZoom.V16 fluorescence microscope and z-stacks were collected using an LSM700 laser scanning confocal microscope (Carl Zeiss Micrsocopy LLC, NY, USA). Animals with mistargeted viral injections were excluded from analysis (n = 3).

Transduced cells expressing mCherry on every other coronal brain slice from bregma −1.3 to −2.3 were counted. Slices from two mice used in behavior experiments were excluded from cell counts due to poor quality of a significant portion of the slices, but expression in the LH^{PV} nucleus was confirmed, and therefore, their behavior data were included in this work.

3.3 Results

3.3.1 Chemogenetic inhibition of LH^{PV} neurons increases food intake and general arousal

To perform these loss-of-function like measurements, I targeted neurons in the LH of *Pvalb*^{IREScre} mice ($LH^{PV/hM4D}$) by bilaterally injecting a Cre recombinase-dependent viral vector that drives the expression of the inhibitory G-protein-coupled receptor hM4D fused to mCherry (110). I inhibited $LH^{PV/hM4D}$ neurons in sated mice by intraperitoneally injecting 3.0 mg/kg clozapine-*N*-oxide (CNO) during the early light phase, when mice normally eat little (**Figure 12a**). Chemogenetic inhibition of $LH^{PV/hM4D}$ neurons significantly increased food intake by 60% during the first 4 h after CNO injection compared to vehicle control (**Figure 12c,d**) demonstrating that LH^{PV} neuron activity is necessary for regulating feeding. The magnitude of the feeding response was related to the number of hM4D-expressing LH^{PV} cells (**Figure 13a,b**).

I observed that chemogenetic inhibition of LH^{PV} neurons did not affect water intake in water-sated mice (**Figure 14b)** suggesting that inhibition of LH^{PV} neurons selectively stimulated food rather than water intake. Moreover, I did not observe significant changes in feeding or drinking during inhibition of LH^{PV} neurons during the dark cycle, when mice normally eat (**Figure14e, Figure 15a-c**).

During the same experiments, I monitored general arousal (measured as time spent mobile, including grooming and locomotion) of the animals for 4 h following injection of CNO or vehicle. General arousal was significantly elevated by 44% in the 4 h

following chemogenetic inhibition of LH^{PV} neurons in sated mice during the light phase (**Figure 12e,f**, **P* = 0.0265).

General arousal was increased by 46% following inhibition of LH^{PV} neurons at the onset of dark phase in sated mice (**Figure 15d,e**). Thus, the increase in arousal was not solely due to increase in food intake, as there was no significant change in food intake during this same period.

3.3.2 Chemogenetic activation of LH^{PV} neurons does not affect food intake but decreases general arousal

In contrast, activation using the CNO-responsive excitatory receptor hM3D in LH^{PV} neurons ($LH^{PV/hM3D}$) did not affect food or water consumption in sated mice during the light cycle (**Figure 12h,i, Figure 14b,c**). I did not observe significant changes in feeding or drinking when testing whether activation of LH^{PV} neurons would affect food and water intake during the dark cycle, when mice normally eat (**Figure 15g,h, Figure 14f,g**).

Chemogenetic excitation of LH^{PV} neurons induced a 37% decrease in general arousal in sated mice at 4 h following injection during light phase (**Figure 12j-k**, *n* = 8, **P* = 0.0363).

3.4 Figures and tables

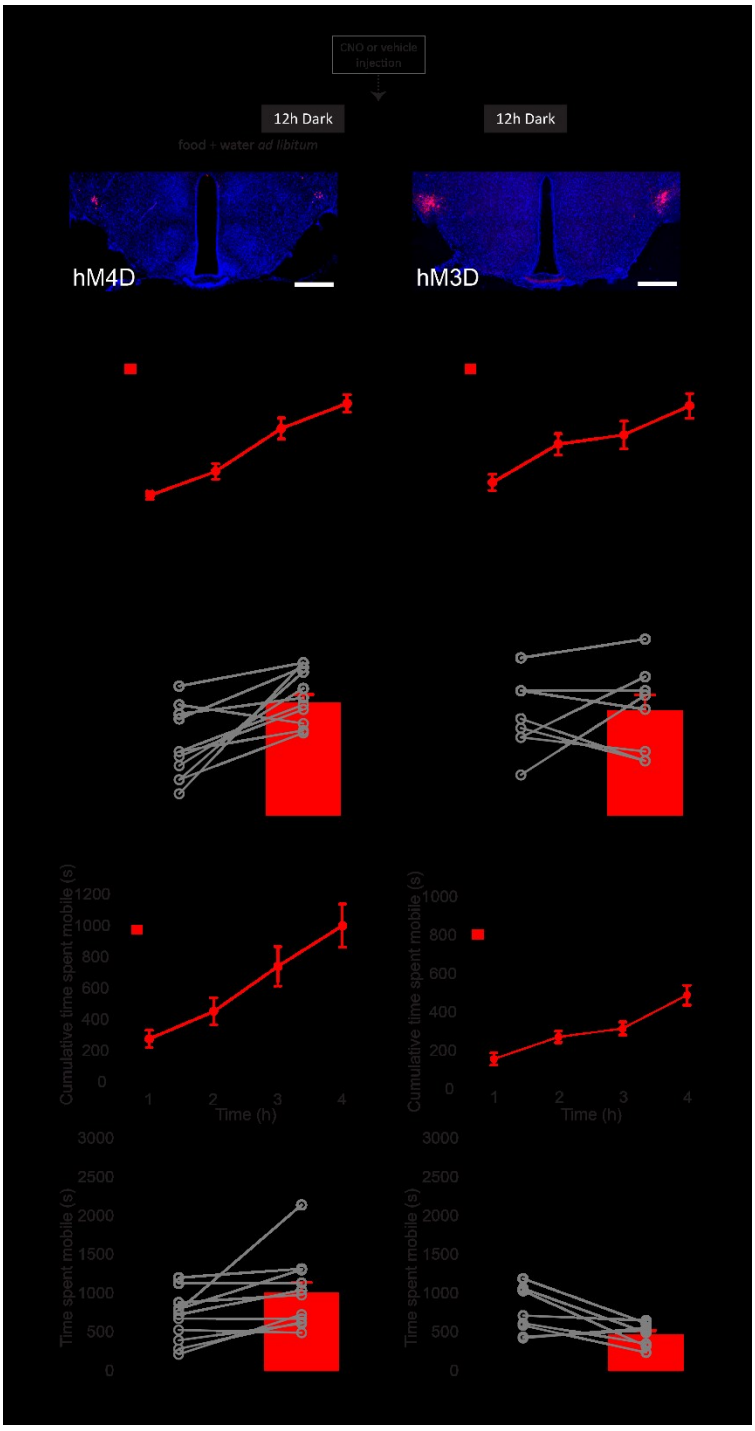

Figure 12

Inhibition of LH^{PV} neurons increases food intake and arousal in sated mice. (**a**) Experimental design of behavioral assays. Mice received *ad libitum* access to food and water before and during testing.

Intraperitoneal injections (i.p.) of CNO or vehicle were performed in the early of the light cycle. (**b**) Representative image showing bilateral hM4D:mCherry expression (red) in LH^{PV} neurons. Scale bar = 500 µm. Section was counterstained with DAPI (blue). (**c**) Chemogenetic inhibition of LH^{PV} neurons significantly increased food intake during the first 4 h after CNO injection (60% increase; n = 11; $*P$ = 0.0085, $**P$ = 0.0031). (**d**) Summary bar graphs showing the cumulative food intake during control and after inhibition of LH^{PV} neurons at 4 h. (**e**) Cumulative arousal in the 4 h following injection in sated $LH^{PV/hM4D}$ mice during the early light cycle (n = 11, $*P$ = 0.0265). (**f**) Arousal increased 44% by 4 h following injection in sated $LH^{PV/hM4D}$ mice during the early light cycle (n = 11, $*P$ = 0.0265). (**g**) Representative image showing bilateral hM3D:mCherry expression (red) in LH^{PV} neurons. Scale bar = 500 µm. Section was counterstained with DAPI (blue). (h) Chemogenetic activation of LH^{PV} neurons does not affect food intake (n = 8; P = 0.6904). (**i**) Summary bar graphs showing that the cumulative food intake is unaffected during activation of LH^{PV} neurons at 4 h. Bars represent mean ± s.e.m.; circles indicate data from individual mice. (**j**) Cumulative arousal in the 4 h following injection in sated $LH^{PV/hM3D}$ mice during the early light cycle (n = 8, $*P < 0.05$). (**k**) Arousal decreased 28% by 4 h following injection in sated $LH^{PV/hM3D}$ mice during the early light cycle (n = 8, $*P$ = 0.0363). Bars represent mean ± s.e.m.; circles indicate data from individual mice.

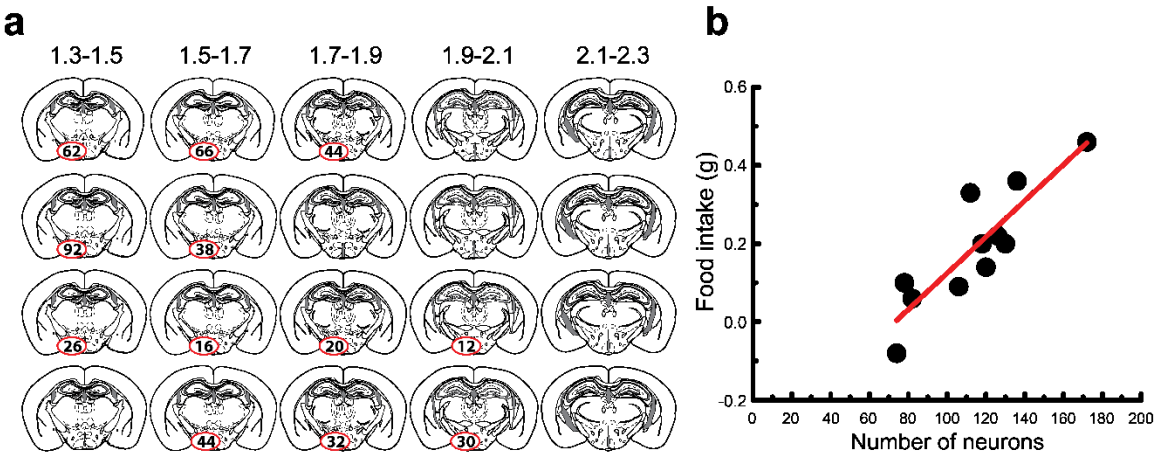

Figure 13

Food intake was dependent on the number of hM4D-expressing LH^{PV} ($LH^{PV/hM4D}$) neurons. (**a**) Schematics depicting the number of $LH^{PV/hM4D}$ neurons counted bilaterally for 4 representative mice. (**b**) Graph showing the relationship between the magnitude of food intake and the number of $LH^{PV/hM4D}$ neurons. The variability on baseline food intake between mice was accounted by calculating the amount of food consumed at 4 h as the difference between CNO and vehicle injection. Circles indicate food intake at 4 h for individual mice (n = 11). Red line shows Pearson correlation $*P$ = 0.0004; $r(11)$ = 0.874.

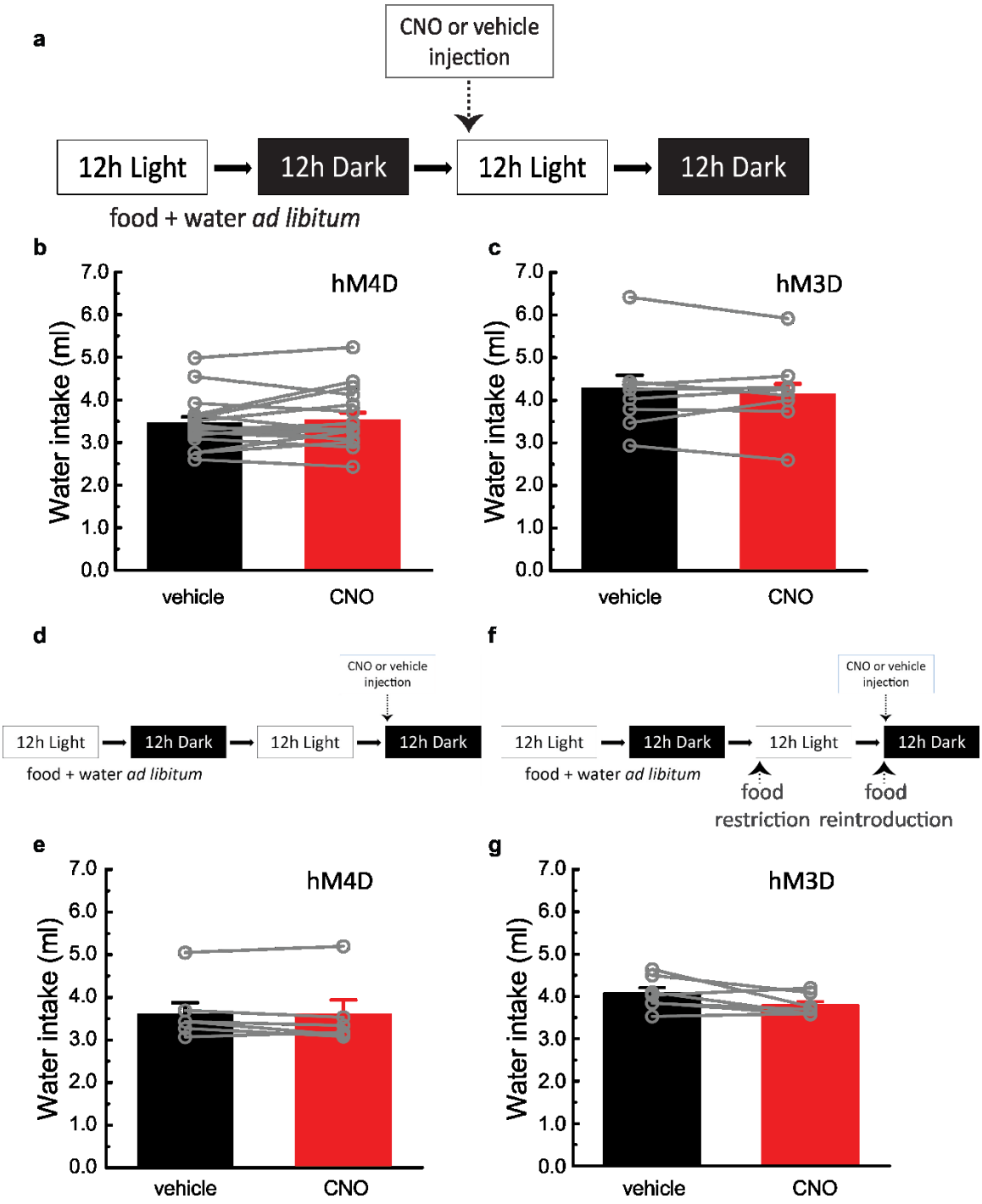

Figure 14

Chemogenetic inhibition and excitation of LH^{PV} neurons did not affect water intake in water-sated mice. (**a**) Experimental design of behavioral assays in the light cycle. Mice received *ad libitum* access to food and water prior to and during testing. Intraperitoneal injections (i.p.) of CNO or vehicle were performed at the

beginning of the light cycle. (**b**) Summary bar graphs showing the cumulative water intake after inhibition and (**c**) excitation of LH^{PV} neurons at 24 h (*n* = 11; *P* = 0.3802 and *n* = 8; *P* = 0.84518, respectively). (**d**) Experimental design of $LH^{PV/hM4D}$ behavioral assays in the dark cycle. Mice received *ad libitum* access to food and water prior to and during testing. Intraperitoneal injections (i.p.) of CNO or vehicle were performed at the beginning of the dark cycle. (**e**) Summary bar graph showing cumulative water intake at 24 h for $LH^{PV/hM4D}$ mice injected with CNO or vehicle during the dark cycle (*n* = 6; *P* = 0.31494). (**f**) Experimental design of $LH^{PV/hM3D}$ behavioral assays in the dark cycle. Mice were food restricted for 10 h prior to testing to eat during the dark cycle. Intraperitoneal injections (i.p.) of CNO or vehicle were performed at the beginning of the dark cycle. (**g**) Summary bar graphs showing the cumulative water intake after excitation at 24 h (*n* = 7; *P* = 0.081). Bars represent mean ± s.e.m.; circles indicate data from individual mice.

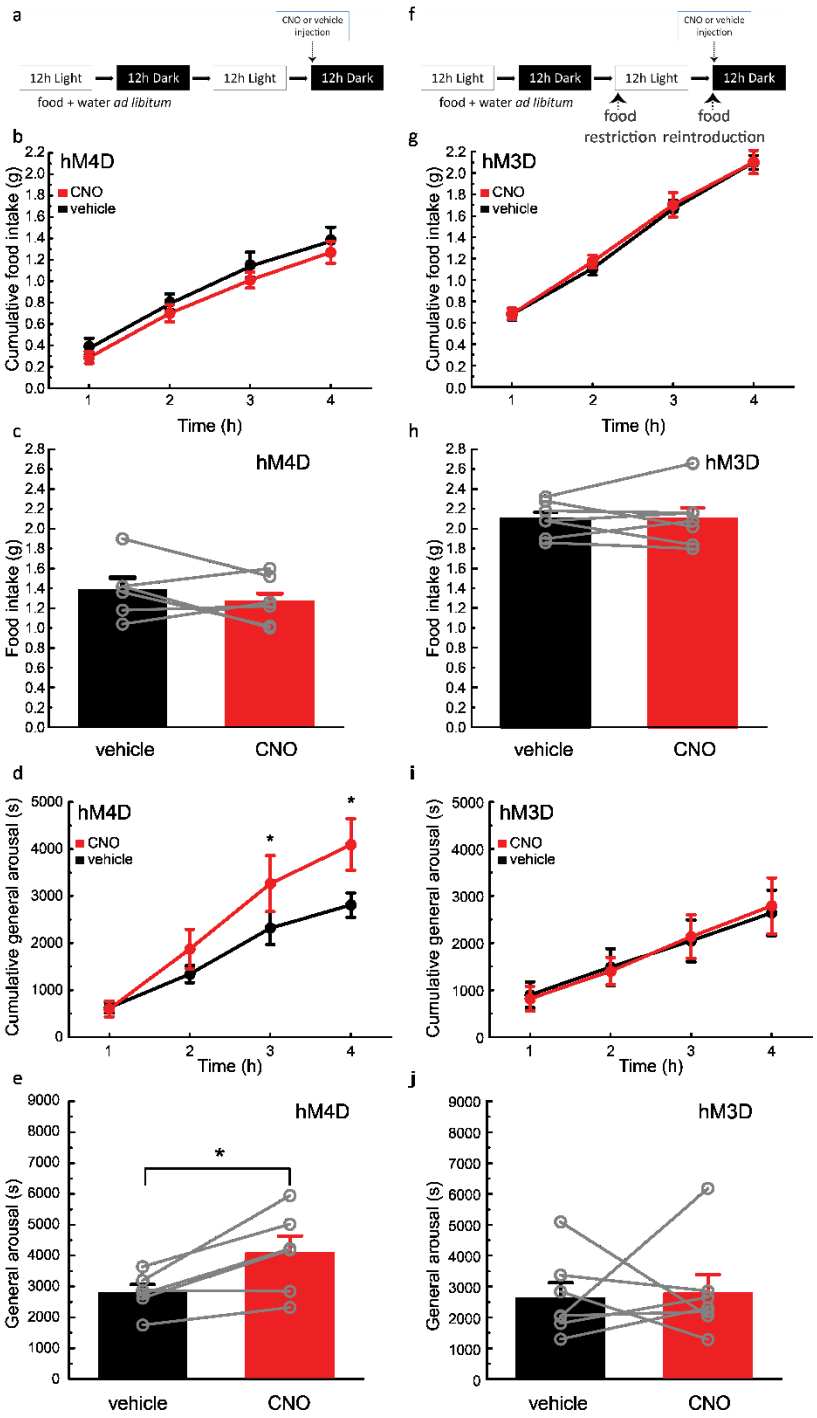

Figure 15

Food intake and arousal in response to chemogenetic inhibition and excitation of LH^{PV} neurons during the dark cycle. (**a,f**) Experimental design of behavioral assays. Mice received *ad libitum* access to food and water prior to and during testing for inhibition (**a**) and were food restricted 10 h prior to testing for

excitation to further increase their drive to eat during the dark cycle (**f**). Intraperitoneal injections (i.p.) of CNO or vehicle were performed at the beginning of the dark cycle. (**b**) Chemogenetic inhibition of LH^{PV} neurons did not affect food intake during the first 4 h after CNO injection (n = 6; P = 0.37818). (**c**) Summary bar graphs showing the cumulative food intake after inhibition of LH^{PV} neurons at 4 h. (**d**) Cumulative arousal in the 4 h following injection in sated $LH^{PV/hM4D}$ mice during the early dark cycle (n = 6, *P < 0.05). (**e**) Cumulative arousal in the 4 h following injection in sated $LH^{PV/hM4D}$ mice during the early dark cycle (n = 6, *P < 0.05). (**f**) Experimental design of behavioral assays for $LH^{PV/hM3D}$ mice. (**g**) Chemogenetic activation of LH^{PV} neurons did not affect food intake (n = 7; P = 0.974). (**h**) Summary bar graphs showing that the cumulative food intake is unaffected during activation of LH^{PV} neurons at 4 h. (**i**) Cumulative arousal was not altered by 4 h following injection in food restricted $LH^{PV/hM3D}$ mice during the early dark cycle (n = 7, P = 0.8691). (**j**) Arousal was not altered by 4 h following injection in food restricted $LH^{PV/hM3D}$ mice during the early dark cycle (n = 7, P = 0.8691). Bars represent mean ± s.e.m.; circles indicate data from individual mice.

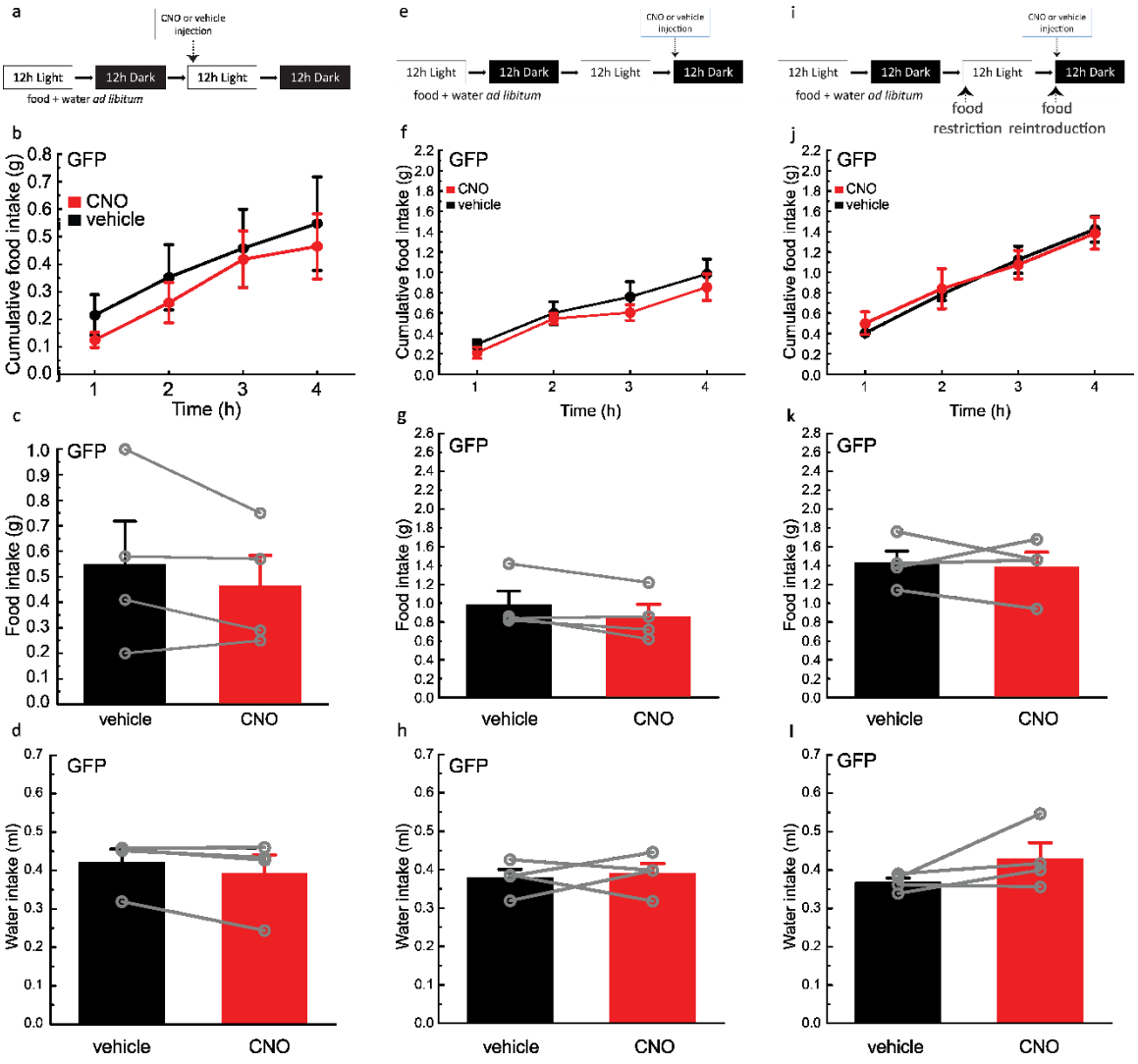

Figure 16

Food and water intake were unaffected by injection of CNO in LH$^{PV/GFP}$ mice during the light or dark cycle. (**a,e,i**) Experimental designs of all behavioral assays for LH$^{PV/GFP}$ mice. Mice received *ad libitum* access to food and water prior to and during testing (**a**) in the light cycle. Intraperitoneal injections (i.p.) of CNO or vehicle were performed at the beginning of the light cycle. For dark cycle testing, mice received *ad libitum* access to food and water prior to and during testing (**e**) or were food restricted 10 h prior to testing (**i**) to further increase their drive to eat during the dark cycle. Intraperitoneal injections (i.p.) of CNO or vehicle were performed at the beginning of the dark cycle. (**b**) Injection of CNO does not affect food intake (n = 4; P = 0.2999). (**c**) Summary bar graphs showing that that cumulative food intake is unaffected following

injection of CNO at 4 h. (**d**) Water intake at 24 h for $LH^{PV/GFP}$ mice injected with CNO or vehicle during the light cycle (n = 4, P =0.1631). (**e**) Experimental design of dark phase *ad libitum* food and water behavioral assays. (**f**) CNO did not affect food intake during the first 4 h after CNO versus vehicle injection (n = 4; P = 0.7847). (**g**) Summary bar graphs showing the cumulative food intake after injection of CNO versus vehicle at 4 h. (**h**) Summary bar graphs showing the cumulative water intake after injection of CNO versus vehicle at 24 h (n = 4; P = 0.1955). (**i**) Experimental design of dark phase behavioral assays following 10 h food restriction. (**j**) CNO injection after food restriction did not affect food intake after injection of CNO versus vehicle at 4 h (n = 4; P = 0.1109). (**k**) Summary bar graphs showing the cumulative food intake after injection of CNO versus vehicle at 4 h. (**l**) Summary bar graphs showing the cumulative water intake after injection of CNO versus vehicle at 24 h (n = 4; P = 0.7719). Bars represent mean ± s.e.m.; circles indicate data from individual mice.

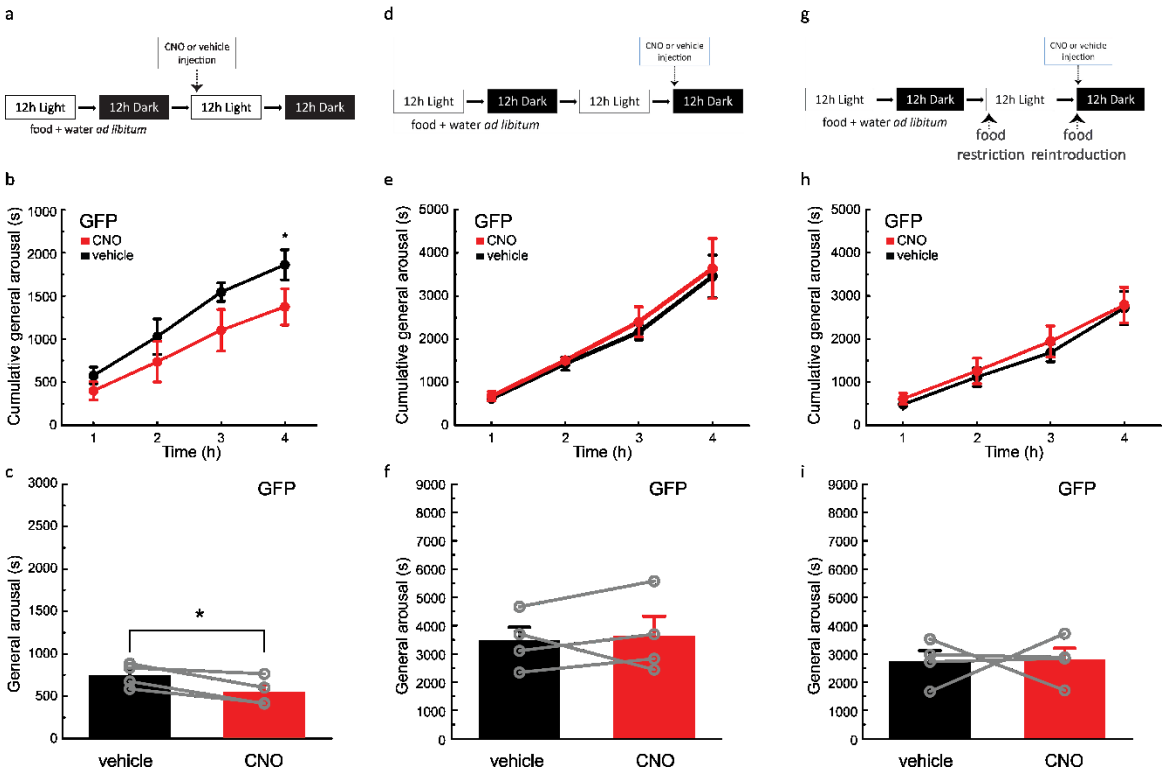

Figure 17

General arousal following injection of vehicle and CNO in LH$^{PV/GFP}$ mice during the light and dark cycle. (**a,d,g**) Experimental designs of all behavioral assays for LH$^{PV/GFP}$ mice. Mice received *ad libitum* access to food and water prior to and during testing (**a**) in the light cycle. Intraperitoneal injections (i.p.) of CNO or vehicle were performed at the beginning of the light cycle. For dark cycle testing, mice received *ad libitum* access to food and water prior to and during testing (**d**) or were food restricted 10 h prior to testing (**g**) to further increase their drive to eat during the dark cycle. Intraperitoneal injections (i.p.) of CNO or vehicle were performed at the beginning of the dark cycle. (**b**) Cumulative arousal in the 4 h following injection in sated LH$^{PV/GFP}$ mice during the early light cycle (n = 4, *P = 0.0272). (**c**) Arousal decreased 26% by 4 h following injection of CNO in sated LH$^{PV/GFP}$ mice during the early light cycle (n = 4, *P = 0.0272). (**d**) Experimental design of dark phase *ad libitum* food and water behavioral assays. (**e**) Cumulative arousal in the 4 h following injection in sated LH$^{PV/GFP}$ mice during the early dark cycle (n = 4, P = 0.7356). (**f**) Arousal was not altered by 4 h following injection in sated LH$^{PV/GFP}$ mice during the early dark cycle (n = 4, P = 0.7356). (**g**) Experimental design of dark phase behavioral assays following 10 h food restriction. (**h**)

Cumulative arousal was not altered by 4 h following injection in food restricted $LH^{PV/GFP}$ mice during the early dark cycle (n = 4, P = 0.93803). (**i**) Arousal was not altered by 4 h following injection in food restricted $LH^{PV/GFP}$ mice during the early dark cycle (n = 4, P = 0.93803). Bars represent mean ± s.e.m.; circles indicate data from individual mice.

Chapter 4

Functional imaging of neuronal activity of LH^{PV} cells using two-photon fluorescence endomicroscopy

4.1 Introduction

A fundamental goal of neuroscience research is to understand how dynamics in neuronal circuits control behavioral outputs. To date, experiments have largely been unable to determine when specific cell types are active to provide quantitative relationships between circuit activity and behavior. Studies in rats and primates have used electrophysiology methods to record the action potential firing activity of cells in the lateral hypothalamus during different metabolic states such as satiety and hunger (111, 112). These studies revealed a wide range of activity patterns, including increases and decreases in firing rate during hunger as well as different time courses of activity relative to feeding initiation. These experiments were performed with traditional extracellular electrophysiology methods and could not identify the cell types of the recorded neurons. Therefore, the feeding-related activity patterns of the genetically-distinct cell types in the lateral hypothalamus remain unknown.

An understanding of the neuronal activity of specific cell types during feeding-related behaviors would elucidate the functions performed by the components of the lateral hypothalamic circuit and thus provide insight into how the lateral hypothalamus drives feeding. The development of new methods that enable optical or electrophysiological recordings from genetically-identified cell types at deep brain regions and in freely-moving mice or rats have recently begun to emerge.

The combination of fiber photometry or *in vivo* endomicroscopy with genetically encoded calcium indicators (GCaMPs) enables the analysis of fluctuations in the intensity of calcium-sensitive fluorophores as an indicator of neuronal activity. Initially, the

targeting of deep brain structures was limited, as traditional two photon microscopes were restricted to image depths of ~1 mm from the surface (113). The use of two photon endomicroscopy to image deep brain structures has been made possible due to the advent of gradient refractive index (GRIN) lenses (114-117).

Single-photon endomicroscopy and fiber photometry have recently been utilized to record changes in activity in AGRP neurons in the arcuate nucleus (ARC^{AGRP}; (46, 47, 50)). This work has revealed surprising results that have spurred the field to reformulate theories on the functional role of these neurons. It was previously known that optogenetic stimulation of ARC^{AGRP} neurons induced voracious feeding (33). Yet, initial *in vivo* single-photon recordings of ARC^{AGRP} neurons revealed that activity of these cells was elevated during fasting compared to satiety, and this activity dramatically decreased within seconds upon feeding. Betley *et al.* demonstrated that these neurons exhibited increased activity in response to peripheral ghrelin administration(46). Additionally, they showed that these neurons responded similarly to the mere expectation of food, indicating that ARC^{AGRP} neurons may not be driving feeding or hunger as they were traditionally regarded (46). These results were further supported by similar studies from fiber photometry recordings of ARC^{AGRP} neurons (47, 50). Chen *et al.* went a step further, to demonstrate that ARC^{AGRP} activity dramatically decreased upon the sensory detection of food (47). This led to the determination that ARC^{AGRP} neurons must be driving food seeking, or a hunger drive, rather than just hunger (47, 50). However, more recent investigations into the activity of ARC^{AGRP} neurons have provided further complexity to this model. Nutrient ingestion has now been shown to drive similar shifts in ARC^{AGRP}

activity over the course of several minutes in proportion to caloric value, regardless of the individual nutrient or metabolic state of the animal. Additionally, peripheral leptin injection has been shown to induce a much more gradual shift in the activity of ARC^{AGRP} neurons, on the scale of hours rather than seconds or minutes (49). The differences in the time courses of response to varying stimuli reveal that ARC^{AGRP} neurons are capable of integrating both central and peripheral sensory information regarding food availability and metabolic state, and they respond differentially based on these factors.

To date, the dynamics of LH^{PV} neurons *in vivo* remain unknown. I used two photon fluorescence endomicroscopy to image the activity of LH^{PV} neurons in awake, head-fixed mice during different metabolic states. These findings reveal decreased calcium signals from LH^{PV} neurons during food-deprived conditions. Moreover, LH^{PV} neurons rapidly respond to the sensory detection of food.

4.2 Materials and methods

4.2.1 Stereotaxic viral injection and GRIN lens or guide cannula implantation

For GRIN lens and GRIN lens cannula implantation surgeries, six to eight-week-old *Pvalb*^{IREScre} heterozygous mice were used. Mice were anesthetized with isoflurane and placed into a stereotaxic apparatus (David Kopf Instruments, CA, USA). After exposing the skull by a minor incision, a small hole (< 1 mm diameter) was drilled for virus injection and subsequent GRIN lens or cannula implantation. First, a beveled 25-gauge needle was inserted into the hole to create a guide path for the lens or cannula (needle: bregma, −1.80 mm; midline, ±1.40 mm; dorsal surface, −5.20 mm). Next, an adeno-associated virus (rAAV2.9/CAG.FLEX-GCaMP6s.WPRE.SV40, titer: 1.34×10^{13} genomic copies/ml; University of Pennsylvania Gene Therapy Program Vector Core, PA, USA) (Chen *et al.*, 2013) was injected (100 nl; rate: 30 nl/min) into the lateral hypothalamus (injection: bregma, −1.80 mm; midline, ±1.40 mm; dorsal surface, −5.40 mm) by a pulled glass pipette (20–30 µm tip diameter) with a micromanipulator (Narishige International USA Inc., NY, USA) controlling the injection speed. After injection, either a GRIN lens (ILW-050-P146-055-NC; Go!Foton Corporaton, NJ, USA) or a cannula (MGC_560/610_5.2_v2.1; Bocarsly *et al.*, 2015; Doric Lenses Inc., QC, Canada) was lowered into position above the injection site (lens/cannula: bregma, −1.80 mm; midline, ±1.40 mm; dorsal surface, −5.25 mm). A head bar was attached to the skull surface with cyanoacrylate and dental cement (C&B Metabond Adhesive Cement, Parkell Inc., NY, USA) was spread around the lens or cannula and inside the head bar to hold everything in place. A final layer of black dental

cement (Contemporary Ortho-Jet, Lang Dental Manufacturing Company Inc., IL, USA) was applied around the lens or cannula on top of the previous layer of cement. A small piece of Parafilm was used to cover the GRIN lens or cannula, and the inside of the head bar was filled with Kwik-Sil or Kwik-Cast (World Precision Instruments, FL, USA). After surgery, mice were individually housed for 4 weeks for post-surgical recovery, inflammatory response reduction, and viral transduction (117).

4.2.2 Two-photon endomicroscopy system and mice habituation

We used both singlet (ILW-050-P146-055-NC; Go!Foton Corporaton) and doublet (NEM-050-25-10-860-DM; GRINTECH GmbH, Jena, Germany) GRIN lenses for deep tissue imaging in mice. The singlet lens has a working distance of approximately 130 µm on the object side. The doublet lens and guide cannula designs were previously described (117). The numerical aperture (NA) of 0.5 provides sufficient 3D resolution for functional imaging of neuronal cell bodies.

The GRIN lens was incorporated into a two-photon fluorescence microscope equipped with a 5× air objective of 0.16 NA (Zeiss), which generated the initial focus of the excitation light (of 0.2 NA, to match the 0.19 NA of the GRIN lens on the image side) to be relayed by the GRIN lens to the sample side. The two-photon fluorescence signal was collected and transported back to the microscope by the GRIN lens and detected with a photomultiplier tube (H7422; Hamamatsu Corporation, NJ, USA). A Ti:Sapphire femtosecond oscillator (Mai Tai HP; Spectra-Physics, CA, USA) tuned to 910 nm was used as the excitation light source for all experiments.

Three weeks after surgery, mice were habituated to head-restraint in a custom-built restraint system. Mice were habituated to head-restraint during escalating durations from 5 to 40 minutes over a period of 3 to 5 days. Following habituation to head fixation, mice were habituated to the *in vivo* imaging environment. The head-restrained mouse was placed under the two-photon microscope objective and the empty food holding plate was placed approximately 2-5 mm in front of its nose and left in place for varying durations (5 times per session, 3-10 minutes per placement) during two habituation sessions. ScanImage 3.8 (Vidrio Technologies LLC, VA, USA) was used to collect *in vivo* imaging videos at 1.5 Hz for all mice and additionally at 3.0 Hz for a subset of mice. Laser power was set to 50% to 70% power (*i.e.* 45 to 48 mW measured ~13 mm below the objective. For each mouse, the power setting was consistent among all recordings to avoid brain tissue damage by heat. All data acquisition sessions were performed during the light phase and at the same time of day for each mouse. Experiments in two mice were performed at multiple imaging speeds (1.5 Hz and 3.0 Hz), and showed the same trends in activity regardless of acquisition speed (data not shown). Acquisition speed was limited to 1.5 to 3.0 Hz by the scanning stage galvanometer.

4.2.3 Two-photon endomicroscopy metabolic state recordings

Functional images from $LH^{PV/GCaMP6s}$ neurons were acquired for each mouse (31 neurons, n = 7 mice; unilateral) during sated and food-deprived states in sessions of 5 minutes/day. One to eleven neurons were imaged per mouse. For the first batch of mice (n = 3 mice, 17 neurons), we recorded one session during both metabolic states. For the

second batch of mice (*n* = 4 mice, 14 neurons), we recorded two sessions during both metabolic states. Of note, we only recorded one session from the first cohort. By the time data analysis was completed for the initial ROIs and we decided to image for multiple sessions, GCaMP6s expression had diminished and we were unable to obtain second data sets for the same ROIs. No sensory stimuli were presented during the metabolic state sessions (**Figures 18-20**).

4.2.4 Two-photon endomicroscopy sensory stimuli presentation

All mice were given a 0.4 g serving of peanut butter in their home cage 20 to 48 h prior to sensory stimuli experiments, consumption of the peanut butter was confirmed for each mouse (**Figures 22-23**). Sensory stimuli experiments were performed two times per condition for each mouse to confirm reproducibility of effects. A 15 min rest period was given following each exposure to sensory stimuli, to ensure return to baseline and allow for dissipation of olfactory cues.

Mice were imaged during light phase following either *ad libitum* food and water (sated) or 24 h food deprivation with ad libitum water (food deprived). During olfactory sensory stimulation experiments, a 5 to 10 min video was recorded wherein a 2 min period of baseline images was collected before a metal plate was placed in front of the animal's nose. The plate was left in place for the remainder of the recording. On the plate directly in front of the nose was either no food, moistened regular chow, or peanut butter (Heinz Co., Pittsburgh, PA, USA). The order of sensory stimuli presentation was randomized. Plate position was confirmed at the end of each placement, to ensure that

the desired alignment and distance from the nose were achieved. Replicates were performed to ensure reproducibility of response.

A subset of mice was also exposed to a novel sound following 24 h food deprivation. Fluorescence was recorded during a 2 min period of baseline images, after which a novel two tone sound was played (~85 dB), video recording continued for an additional 3 min following the sound.

4.2.5 Histology for functional imaging animals

Mice were deeply anesthetized with isoflurane and transcardially perfused with 1× PBS followed by 4% PFA in 1× PBS. Head bars and GRIN lens were carefully removed to avoid damaging brain tissue. Whole brains were removed and post-fixed in 4% PFA/PBS for 2 h at 4 °C and subsequently transferred to 1× PBS for 1 to 48 h for storage at 4 °C until further processing. Coronal brain sections (50 µm thick) containing the LH were collected in 1× PBS using a vibrating tissue slicer (vibratome; Leica VT1200), and freely floating slices were immunostained for parvalbumin (PVALB) and green fluorescent protein (GFP). Sections were incubated with a blocking solution of 1× PBS/0.2% Triton X-100 (PBT) plus 2–5% normal donkey serum (NDS) for 1 h. Sections were then incubated with the primary antibodies rabbit anti-PVALB (1:500 PV25; Swant) and chicken anti-GFP (1:1000 GFP-1020; Aves Labs, OR, USA) in PBT/2% NDS overnight at 4 °C. After rinsing 4 × 10 min in 1× PBS, sections were incubated for 2 h with secondary antibodies donkey anti-rabbit-Alexa Fluor 647 (1:500; Invitrogen, CA, USA) and donkey anti-chicken-Alexa Fluor 594 (1:500; Invitrogen) in PBT/2% NDS at room temperature and washed with 1× PBS (4 × 10 min).

Sections were mounted with DAPI-Fluoromount-G aqueous mounting medium (Electron Microscopy Sciences) onto Superfrost Plus glass slides (VWR International). Images were taken with an AxioZoom.V16 fluorescence microscope and z-stacks were collected using an LSM700 laser scanning confocal microscope (Carl Zeiss Microscopy LLC).

4.2.6 Two-photon data analysis

Videos were motion corrected using custom MATLAB R2016B (The MathWorks Inc., MA, USA) scripts generously provided by the Laboratory of Chris Harvey (Harvard University, Boston, MA, USA). Videos were then manually screened for frames containing aberrations due to movement that could not be corrected, and such frames were noted and redacted from analysis. A composite image of the maximum fluorescence signal from the standard deviation of every 10 frames was created for every video of each animal (ImageJ (118)). Signal for each video was compared to identify well-defined and consistently represented somas, from which a region of interest (ROI) map was created to mark each soma as well as a random control area with no defined soma for each animal (ImageJ). The same ROI map was used for all videos of each mouse. The mean gray value (MGV) for each ROI was extracted for every frame of each video (ImageJ). The change in fluorescence ($\Delta F/F$) over time calculated as [MGV – (median MGV of baseline)/(median MGV of baseline)] for each ROI was calculated for each frame. For sensory stimuli experiments baseline was considered the 30 s prior to stimuli presentation. For videos with no sensory stimuli, the median fluorescence of each respective ROI for the entire video was used as the baseline value. Data were displayed as heatmaps and mean traces

± s.e.m. based on custom MATLAB scripts generously provided by Zhenwei Su (Laboratory of J. Nicholas Betley, University of Pennsylvania, PA, USA). Heatmap data were aligned by sensory stimuli presentation (red vertical line) and trimmed to a total of 100 frames (45 frames leading up to stimuli, 55 frames following onset of stimuli) for heatmap figures shown in this chapter. Recordings that did not have sensory stimuli are shown with the full length heatmap.

Thresholding of data was performed to examine changes in fluorescence between metabolic states. Change in fluorescence (ΔF/F) data were thresholded to the top 25% of peak values for each video. The total number of frames above this threshold for each ROI was summed and compared for each metabolic state as an indication of activity for recordings with no sensory stimuli. Events were randomly distributed between cells and normally distributed over the range of change in fluorescence, with the majority of difference between sated and food deprived states occurring in the right arm of the distribution (**Figure 19**).

4.2.7 Slice preparation for electrophysiology and analysis

After cervical dislocation, mice were decapitated and their brains were rapidly removed and placed into an ice-cold N-methyl-D-glucamine (NMDG)-based slicing solution (95) containing (in mM): 92 NMDG, 20 HEPES, 25 glucose, 30 $NaHCO_3$, 1.2 NaH_2PO_4, 2.5 KCl, 5 sodium ascorbate, 3 sodium pyruvate, 2 thiourea, 10 $MgSO_4$, and 0.5 $CaCl_2$, pH 7.4, and osmolarity of 304–308 mOsm. Acute horizontal brain slices (200–240 μm thick) containing the lateral hypothalamus were obtained using a vibratome (Leica

VT1200, Leica Biosystems Inc., IL, USA). Brain slices were transferred to a holding chamber filled with a solution containing (in mM): 92 NaCl, 20 HEPES, 25 glucose, 30 $NaHCO_3$, 1.2 NaH_2PO_4, 2.5 KCl, 5 sodium ascorbate, 3 sodium pyruvate, 2 thiourea, 1 $MgSO_4$, and 2 $CaCl_2$ (pH 7.4, 304–308 mOsm). For electrophysiological recordings, a single slice was submerged in artificial cerebrospinal fluid (aCSF, in mM: 125 NaCl, 2.5 KCl, 1.25 NaH_2PO_4, 1 $MgCl_2$ $6H_2O$, 11 glucose, 26 $NaHCO_3$, 2.4 $CaCl_2$, pH 7.4, and osmolarity of 304–308 mOsm) in a recording chamber that was continuously perfused with a peristaltic pump (World Precision Instruments, FL, USA), at a flow rate of 1.5 to 2.0 ml/min. All solutions were saturated with 95% O_2 and 5% CO_2.

Characterization of the excitation/inhibition ratio of lateral hypothalamic parvalbumin (LH^{PV}) neurons was performed using *Pvalb*^{IREScre};*Rosa26*$^{LSL\text{-}tdTomato}$ mice (*Pvalb*$^{cre/+;}$*Rosa26*$^{tom/tom}$). Parvalbumin-tdTomato-positive lateral hypothalamic neurons were located in brain slices, first with epifluorescence, followed by infrared differential interference contrast (IR-DIC) optics, using an upright Olympus BX51WI microscope (Olympus Corporation, MA, USA). Voltage-clamp recordings were made using a MultiClamp 700B amplifier (5 kHz low-pass Bessel filter and 10 kHz digitization using a 1440A Digidata Digitizer) with pClamp 10.3 software (Molecular Devices LLC, CA, USA). Borosilicate glass patch pipettes (2.0-3.0 MΩ) containing (in mM): 135 potassium gluconate, 10 HEPES, 4 KCl, 4 MgATP, 0.3 Na_3GTP, and 0.2% biocytin (pH adjusted to 7.3 using KOH, and osmolarity of 290 mOsm). The holding potential was –70 mV, and the whole-cell access resistances were 10-20 MΩ. All recordings were made at 32 °C. Input and series resistance were continually measured online; if either parameter changed by

more than 20%, data were not included in the analysis. Membrane potentials were not corrected for liquid junction potentials (estimated to the 10 mV). Excitatory and inhibitory afferents were stimulated at 0.1 Hz with a bipolar stimulating electrode placed 100-300 um rostral to the recording electrode. Horizontal slices containing the LH from *Pvalb*$^{cre/+;}$*Rosa26*$^{tom/tom}$ mice were used and tdTomato-containing cells were visualized in the LH.

The inhibition/excitation ratio experiments were performed having D-AP5 (50 μM) throughout the experiment while isolating AMPA-R-mediated currents at the reversal potential for $GABA_A$ IPSCs (-70 mV). Subsequently, the cells were depolarized to the reversal potential for EPSCs (0 mV) and DNQX (10 μM) was applied in order to block AMPA-Rs and leave a residual current mediated by monosynaptic inhibition through GABA-Rs. The nature of the GABAergic transmission isolated at 0 mV was verified at the end of each experiment by adding picrotoxin (100 μM) to the bath. The inhibition/excitation ratio was then calculated by dividing peak AMPA-R current by peak GABA-R current. All chemicals were obtained from Sigma-Aldrich (MO, USA) or Tocris Bioscience (Bristol, UK).

4.2.8 Statistical analysis

Data are reported as mean ± s.e.m. or mean ± s.d. unless otherwise noted. Statistical analyses were performed using the Analysis ToolPak of Microsoft *Excel* 2016 (Microsoft Corporation, WA, USA). Statistical significance (*P* values) for paired comparisons was determined by two-tailed Student's *t* test ($P < 0.05$ considered

statistically significant). Statistical tests, *n* values for number of animals or number of cells, and exact *P* values are presented in figure legends. (101, 102). Two photon data were analyzed with the Analysis ToolPak of Microsoft *Excel* 2016, Origin Pro v9.2, and MATLAB R2016B.

4.3 Results

I imaged changes in fluorescence as an indicator of activity in 31 LH^{PV} neurons from 7 awake head-fixed mice.

4.3.1 Modulation of LH^{PV} neuronal activity by metabolic states

Even though the non-laminated cytoarchitecture of these neurons in the LH represented a challenge, I successfully recorded fluorescence signals from $LH^{PV/GCaMP6s}$ neurons (31 neurons, *n* = 7 mice; unilateral; **Figure 18**). I recorded calcium fluctuations for 5 minute trials while mice were sated and also following 24 h food deprivation (**Figure 18b,c**). LH^{PV} neurons exhibited a 64% increase in activity on average across all neurons during satiety compared to food deprivation (**Figure 18d**, $*P = 0.021$). An increase in activity was found in 23 of 31 neurons across 7 mice during satiety, and on average, 73% of neurons exhibited this trend in each mouse (**Figure 18d, Figure 19**). The number of events was increased by 25% during satiety; 55% of recorded neurons exhibited this trend (**Figure 20a-b**). We also observed increased inhibitory inputs on LH^{PV} neurons after 24 h of food deprivation compared to satiety state during brain slice electrophysiology experiments (**Figure 21**, $*P < 0.05$). Together, these data show that LH^{PV} neurons exhibit reduced activity during food deprivation. This suggests an unprecedented role for LH^{PV} neurons in encoding for metabolic states.

4.3.2 LH^{PV} neurons respond to the sensory detection of food

Having observed that inhibition of these neurons induces food intake in sated mice and that these cells exhibit fluctuations in activity patterns with metabolic state, I next determined how these neurons responded to the sensory detection of food.

Mice were habituated to the placement of an empty food holding plate $2-5$ mm in front of their nose. Next, I imaged the activity of LH^{PV} neurons during exposure to a) empty food plate as a control, b) regular chow, and c) peanut butter during satiety and after 24 h of food deprivation (**Figure 22**). Of note, mice were previously exposed to both regular chow and a highly palatable food (*i.e.* peanut butter) in their home cages. Additionally, a subset of mice were exposed to a novel auditory cue after 24 h food deprivation (**Figure 24**).

I found that these neurons are more responsive to the smell of both regular chow and highly palatable food than the empty plate during satiety (**Figure 22a-c, Figure 23a**). These neurons exhibit a mean 43% increase in the response to the regular chow when sated compared to the empty plate (**Figure 22a-b, Figure 23a**, n = 14 cells, P = 0.2784). However, there was a far greater response to highly palatable food when sated. The exposure to highly palatable food induced an 82% increase in response to highly palatable food compared to the empty plate (**Figure 22a,c, Figure 23a**, n = 21 cells, P = 0.0916). The magnitude of response to highly palatable food was 8% greater than the response to regular chow (**Figure 23a**, n = 14 cells, P = 0.8184). Thus, LH^{PV} neurons respond to the sensory detection of food during satiety and are sensitive to the palatability/reward value of the food.

LH^{PV} neurons are also responsive to the smell of both regular chow and highly palatable food than the empty plate during food deprivation. When the mice are food deprived, there is a 20% decrease in the mean response to the regular food compared to the empty plate (**Figure 22d-e, Figure 23a**, *n* = 14 cells, *P* = 0.6830). Thus, response to the sensory detection of regular food when food deprived induces a mild decrease in response in LH^{PV} neurons. However, response to highly palatable food was enhanced by food deprivation, where highly palatable food induced at 126% increase in response compared to the empty plate (**Figure 22d-f, Figure 23a**, *n* = 31 cells, **P* = 0.0009). The response to highly palatable food was 385% greater than the response to regular chow when food deprived (**Figure 22e-f, Figure 23a**, *n* = 14, *P* = 0.0666). 74% of LH^{PV} neurons exhibited an increase in the mean change in fluorescence when exposed to highly palatable food while food deprived, whereas only 67% of neurons exhibited an increase while sated (**Figure 22c,f, Figure 23a**). Increases were seen in all 7 mice in response to the sensory detection of highly palatable food during food deprivation. LH^{PV} neurons did not respond to a novel auditory cue during food deprivation, indicating that the aforementioned responses are specific to food-related cues (**Figure 24**). There was an average 94% increase in the change in activity from the sated to food deprived state upon the sensory detection of highly palatable food (**Figure 23a**, *n* = 21 cells, **P* = 0.0323). The onset of response to all stimuli was consistently seen within 10 s of stimuli onset, but returned to baseline within 10 s except when exposed to peanut butter following food deprivation (**Figure 23b**). Thus, LH^{PV} neurons exhibit enhanced responses to the sensory

detection of food during food deprivation and are more sensitive to the palatability/reward value of the food (**Figure 25**).

4.4 Figures

Figure 3

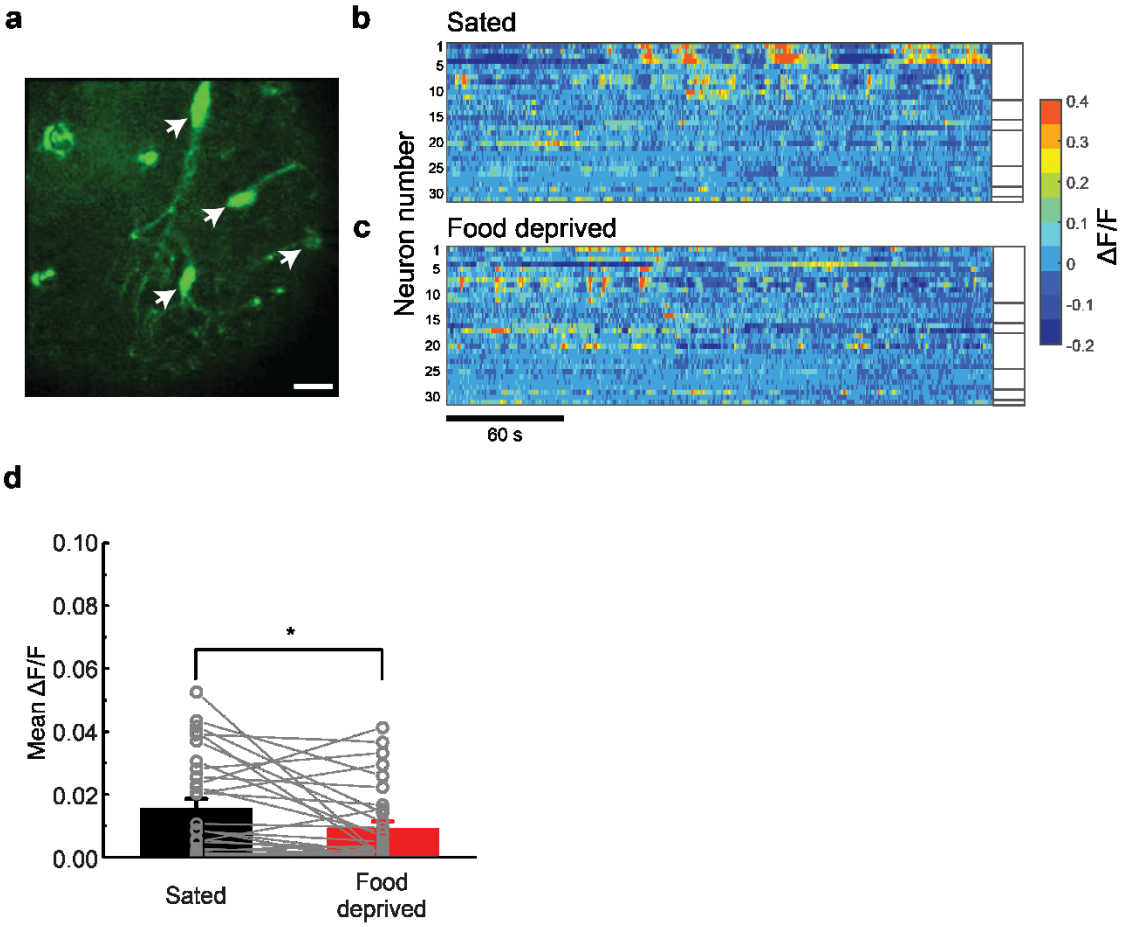

Figure 18

In vivo two-photon fluorescence endomicroscopy of LH^{PV} neurons from head-fixed awake mice. (**a**) Representative *in vivo* image showing LH^{PV} neurons expressing the neuronal activity reporter GCaMP6s ($LH^{PV/GCaMP6s}$). Arrows indicate the recorded $LH^{PV/GCaMP6s}$ neurons. Note the scattered cytoarchitecture of these neurons. (**b-c**) Heat maps depicting $LH^{PV/GCaMP6s}$ neuronal activity as measured by the changes in fluorescence (ΔF/F) over time during sated (top panel) and food-deprived states (bottom panel). Each row represents a neuron. White column on the right groups neurons by animal. (**d**) Mean change in fluorescence revealed that LH^{PV} neurons exhibited decreased activity during food-deprived states (n = 31; $*P$ = 0.021). Bars represent mean ± s.e.m.; circles indicate data from individual cells.

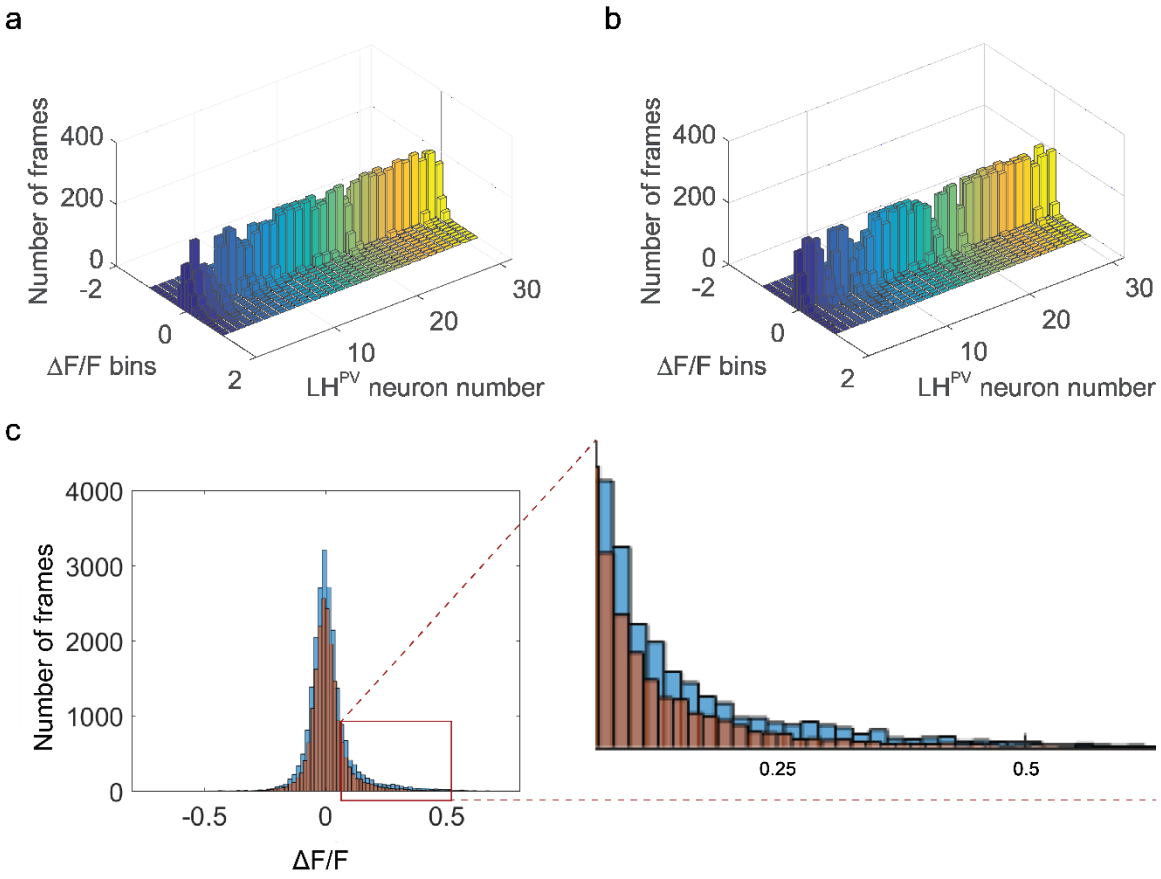

Figure 19

Differences in the change in fluorescence during sated and food-deprived states were driven by increases in fluorescence in many cells during satiety. Distribution of changes in fluorescence (ΔF/F) for individual cells during (**a**) sated and (**b**) food deprived states depicting that the greatest changes in fluorescence were not driven by a minority of cells throughout the population. Colors are used to differentiate separate cells, but have no other value. (**c**) Histogram showing the changes in fluorescence (ΔF/F) for all cells combined during sated (blue) and food-deprived (brown) states. Note the greater number of fluctuations in fluorescence during satiety, calculated as the the number of frames per bin, particularly at the higher (inset) end of the spectrum of change in fluorescence. Thus, the relative increase in mean change in fluorescence during satiety compared to food deprivation was driven by a greater number of increases in fluorescence

during satiety rather than by a greater number of decreases in fluorescence during food deprivation. Y-axis = number of frames, x-axis= 40 ΔF/F bins ranging from -1 to 1, z-axis = cell number.

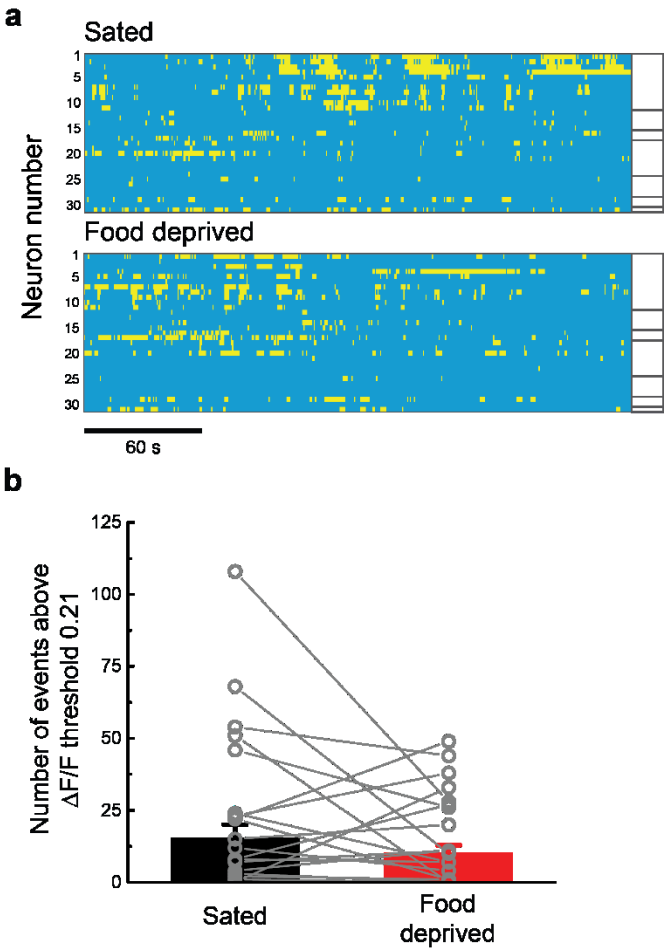

Figure 20

LH$^{PV/GCaMP6s}$ neurons exhibited a greater number of increased-fluorescence events during satiety compared to food deprivation. (**a**) Heatmaps showing the number of events above (yellow) and below (blue) threshold (*i.e.* an arbitrary value assigned to estimate the number of events across time) for each cell while sated and following 24 h food deprivation at ΔF/F threshold of 0.21 (chosen because values greater than this represent the average greatest 25% of increases in fluorescence across time). White column on the right groups neurons by animal. (**b**) Quantification of the number of frames above ΔF/F threshold of 0.21 during each metabolic state. Error bars represent s.e.m.

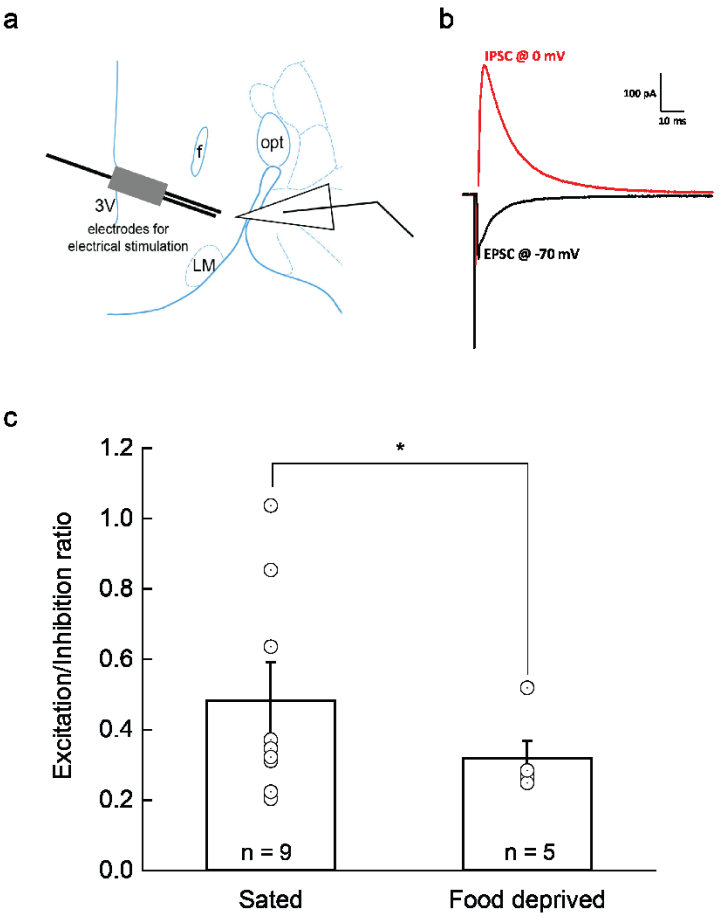

Figure 21

Decreased excitation-inhibition ratio in LH^{PV} neurons during food deprivation. (**a**) Diagram depicting brain slice electrophysiology recordings from LH^{PV} neurons and bipolar electrodes' placement (~150 um) near the recorded cells to electrically evoke AMPA-R (–70 mV) and GABA-R (0 mV) mediated currents. (**b**) Representative trace of electrically evoked AMPA-R (–70 mV) and GABA-R (0 mV) mediated currents. (**c**) Quantification of excitation/inhibition ratio from sated (*n* = 9 cells; 5 mice) and 24 h food deprived (*n* = 5 cells; 4 mice) animals (**P* <0.05). Error bars represent s.e.m.

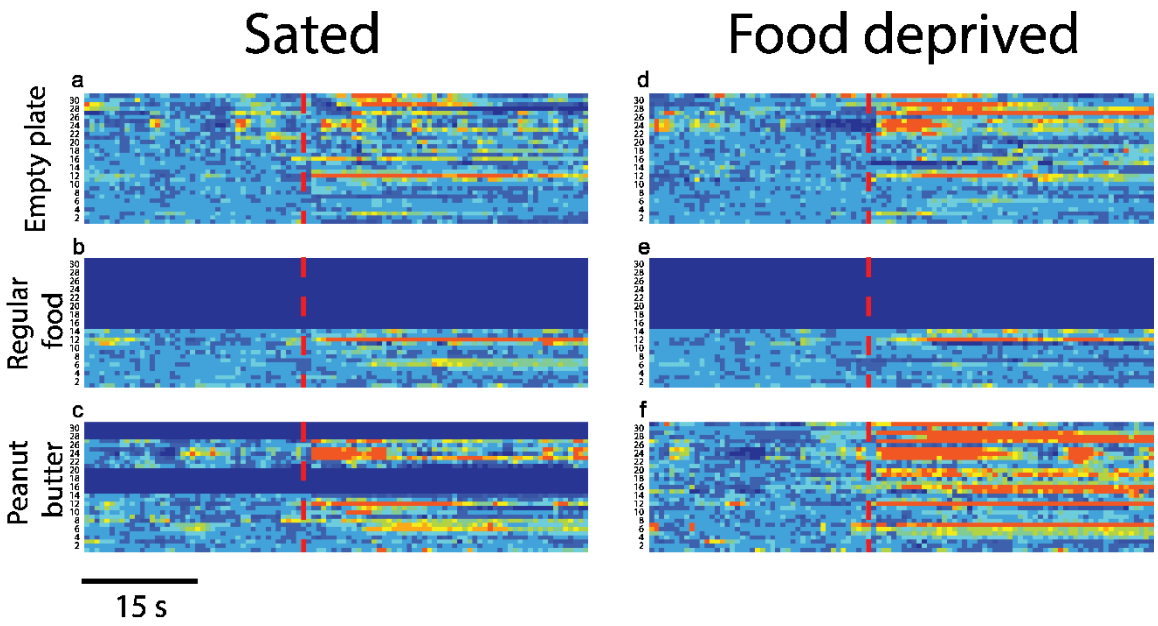

Figure 22

Heatmaps for each cell displaying the change in fluorescence (ΔF/F) upon sensory detection of food. Heatmaps display 30s leading up to placement of stimulus (red vertical line), followed by the first 40s of exposure to the stimulus. (**a**) Sated, empty plate (non-food) (*n* = 31), (**b**) sated, regular food (*n* = 14), (**c**) sated, peanut butter, (*n* = 21), (**d**) food deprived, empty plate (non-food), (*n* = 31), (**e**) food deprived, regular food (*n* = 14), (**f**) food deprived, peanut butter (*n* = 31).

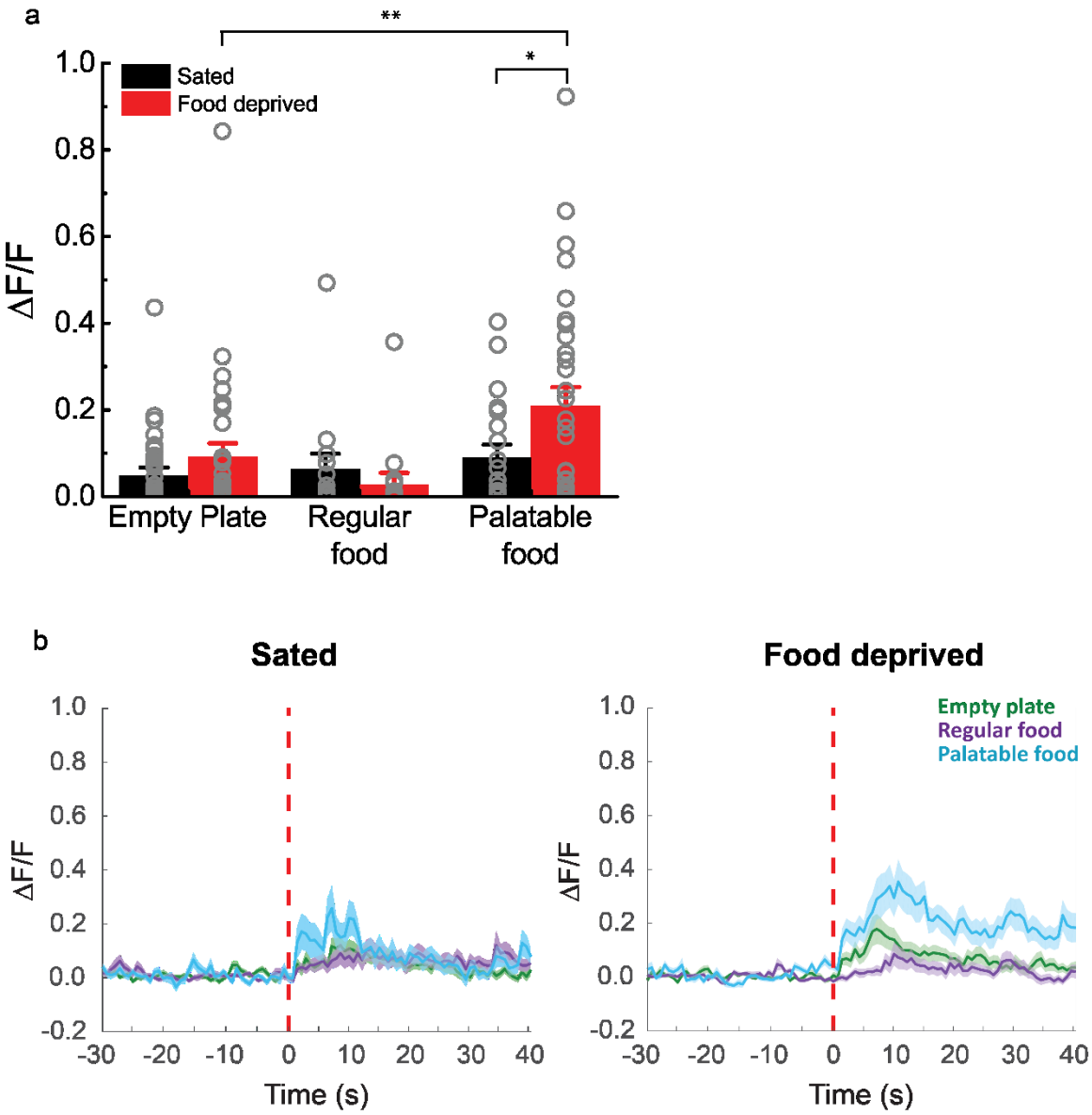

Figure 23

Quantification of magnitude of the effect of regular and highly palatable food on LH^{PV} response. (**a**) Mean change in ΔF/F of all cells combined in each condition (*n* = 14-31 cells, **p* = 0.0323, ***P* = 0.0009). Error bars represent s.e.m. (**b**) Mean ΔF/F before and after placement of each stimuli (red vertical line) while sated and food deprived. Note that the response to palatable food remains elevated when food deprived. Translucent areas represent s.e.m.

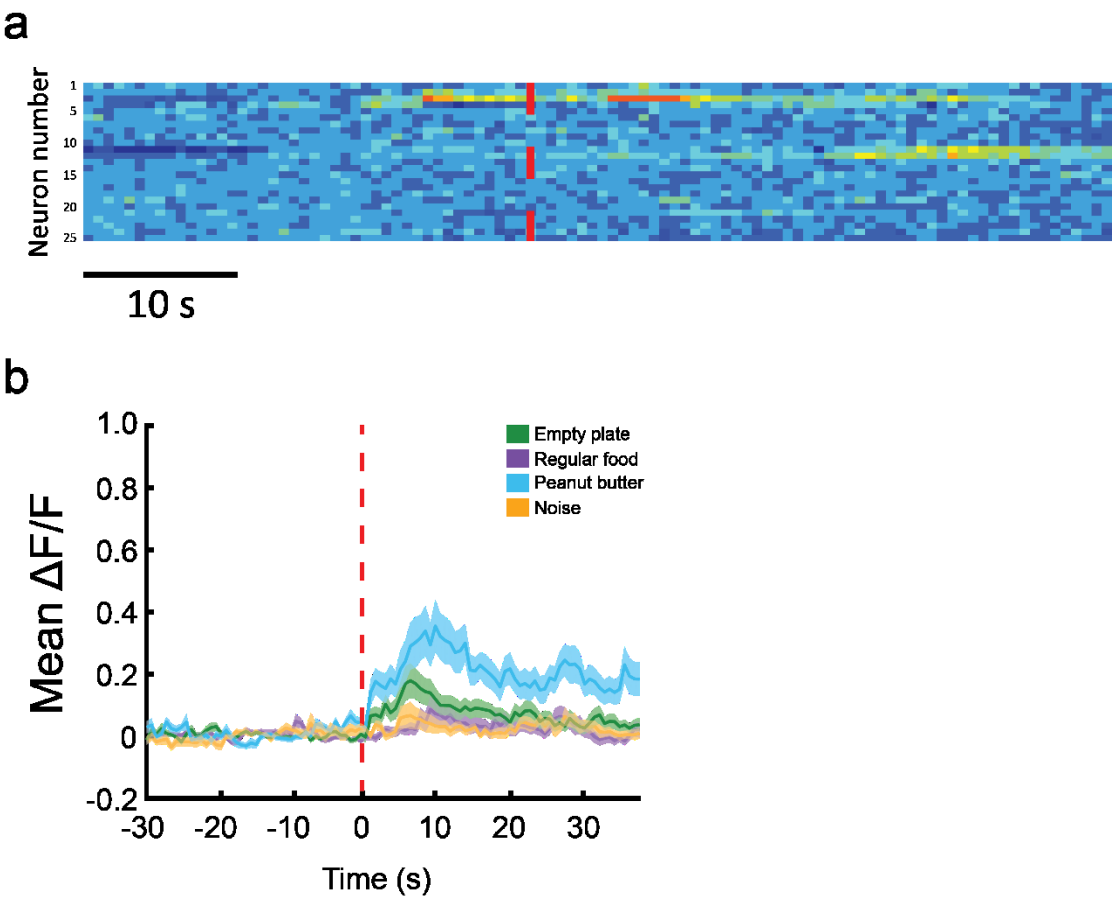

Figure 24

LH^{PV} neurons do not respond to novel auditory stimuli following 24 h food deprivation. (**a**) Heatmap for each cell (*n* = 14) displaying the change in fluorescence (ΔF/F) upon response to a 2 s novel auditory cue. Heatmap displays 30s leading up to onset of stimulus (red vertical line), followed by the first 40s following exposure to the stimulus. (**b**) Quantification of magnitude of the effect of auditory stimuli (noise) compared to response to no food, regular food, and highly palatable food (peanut butter) on LH^{PV} response following 24 h food deprivation. Mean change in ΔF/F of all cells combined in each condition (*n* = 14-31 cells). Translucent areas represent s.e.m.

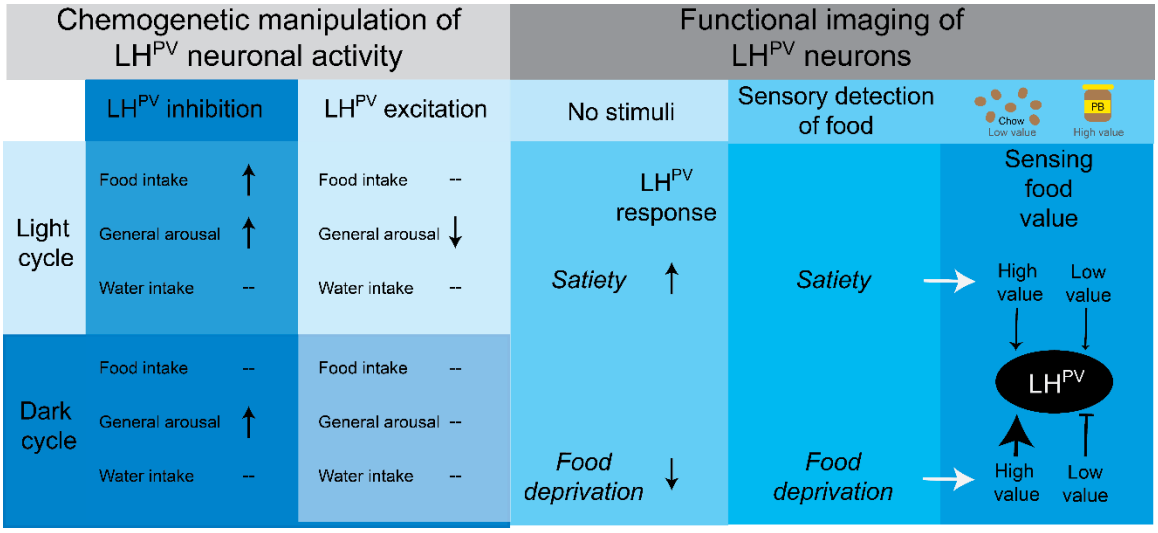

Figure 25

Schematic summary of LH^{PV} neuronal manipulations. (left) Effects of chemogenetic manipulations on food consumption, general arousal, and water intake during light and dark cycles. (right) functional imaging of LH^{PV} neurons during different metabolic states. Note decreased activity during food-deprived conditions. LH^{PV} neuronal activity fluctuates during sensory detection of food. The combination of metabolic states and food value orchestrate the magnitude of neuronal activity responses.

Chapter 5

Discussion and future directions

5.1 Discussion and future directions

Our work shows for the first time a detailed characterization of the properties of LH^{PV} neurons. We first established the electrophysiological and histological properties of these neurons. My subsequent results (described in Chapters 3–4) have expanded upon these findings to describe a functional role for these cells in behavior and have provided mechanistic insights which were previously unexplored.

First, we found that LH^{PV} neurons exhibit a fast-spiking action potential phenotype and electrophysiological characteristics similar to the properties of both hippocampal and neocortical parvalbumin-positive GABAergic interneurons (65, 93). Subsequently, using a combination of optogenetic, electrophysiology, and *in situ* hybridization approaches, we found that LH^{PV} neurons are glutamatergic and provide excitatory input within neuronal circuits of the lateral hypothalamus. Though a previous study showed parvalbumin colocalized with glutamate immunohistochemically in both, rats and mouse LH (91), our work provides quantitative measurements of the percentage of LH^{PV} neurons that express *Vglut2* and demonstrates that these cells release glutamate and form functional excitatory synapses within the LH. Remarkably, our findings and those of others (70, 119), challenge long-standing conceptualizations that fast-spiking neurons are exclusively GABAergic, suggesting conservation of the fast-spiking phenotype across at least two neurotransmitter systems.

Our finding that chemogenetic inhibition of LH^{PV} neurons significantly increases food intake in sated mice, directly implicates LH^{PV} neurons in the regulation of feeding. This data therefore suggest that these neurons normally act to encode for satiety states.

Thus, consistent with this finding, LH^{PV} neuron activity is reduced during food deprivation, which further support the idea that these neurons might encode for metabolic states. It is thus possible that similarly to the signaling properties of hippocampal and neocortical fast-spiking interneurons, LH^{PV} neurons provide fast and temporally precise modulation to their downstream targets and hence regulate feeding. Furthermore, our findings support the idea that inhibitory inputs specifically innervating and suppressing glutamatergic neurons in the lateral hypothalamus promote feeding (61). This previous study showed that inhibitory projections from the extended amygdala preferentially inhibit glutamatergic neurons in the lateral hypothalamus to drive feeding. These results demonstrated that lateral hypothalamic glutamatergic neurons are critical for regulating food consumption. Importantly, these neurons are located in a more lateral region of the LH than the areas ablated in lesion studies, which were found to drive decreases in food intake (14). Here, we have found and given identity to a new element belonging to the glutamatergic circuitry within the lateral hypothalamus.

In addition, my work provides a key piece of data which is the activity dynamics of these neurons *in vivo*. In the LH, fluctuations in neuronal activity have been reported in unspecified (111) and GABAergic (60) neurons during different metabolic states and during appetitive and consummatory behaviors. It is possible that LH^{PV} neurons play a role in driving sensory detection of food or contextual cues of feeding behaviors. An understanding of the fluctuations in neuronal activity of specific cell types during metabolic states and food rewards would provide insight into how the lateral hypothalamic circuitry drives appetitive and consummatory behaviors. This is supported

by recent studies showing that the activity of neurons in the arcuate nucleus of the hypothalamus can be rapidly modulated by the sensory detection (*i.e.* sight and smell) of food (46-48, 50). Furthermore, those fluctuations in neuronal activity were dependent on food availability, palatability, consumption, and nutritional states Those studies suggested that AGRP/POMC neurons may play a primary role in driving food seeking.

In accordance with this, I observed significant increases in general arousal during inhibition of LH^{PV} neurons and reduced arousal during excitation of LH^{PV} neurons. The increases in arousal seen during chemogenetic inhibition occur even in the absence of increased food consumption, indicating that arousal was neither the primary cause nor a secondary consequence of feeding. Our findings on general arousal fluctuations during manipulations of LH^{PV} neurons suggest that those neurons might also be involved in sensing for food availability. Perhaps feeding and food seeking are not always bound to one another, and the two may be separable depending on the metabolic state of the animal.

I used two photon endomicroscopy to provide insights into the function of LH^{PV} neurons *in vivo* during different metabolic states. I found that on average LH^{PV} neurons are significantly more active during satiety than during food deprivation. I found that this population of neurons is not uniform, in fact, 27% of neurons showed no change or exhibited increased activity during food deprivation, though such increases were modest. Chen *et al.* reported that ARC^{AGRP} neurons also exhibit cell-to-cell variability in response to metabolic state (50). These findings support my behavioral results, in that chemogenetic inhibition of LH^{PV} neurons drove feeding, perhaps by instituting a food-

deprived-like state. Furthermore, these findings also may explain why chemogenetic excitation of LH^{PV} neurons did not significantly alter food intake in sated mice, because these neurons were likely already active.

I decided to delve further into this line of thinking, by investigating the response of these neurons to sensory stimuli, to determine whether the sensory detection of food may alter activity of LH^{PV} neurons *in vivo*. Prior work has shown that AGRP neurons respond rapidly to the consumption of food, but even more surprising was the finding that they also respond to the mere sensory detection of food (46-48, 50). Similarly, I found that 74% of LH^{PV} neurons exhibited increased activity in response to the sensory detection of peanut butter. The activity of these neurons remained elevated for an average of 2 to 5 minutes after the initial onset of exposure (data not shown). Additionally, these neurons did not respond to a novel auditory stimulus, revealing that LH^{PV} neurons are specifically sensitive to food-related sensory stimuli. Thus, LH^{PV} neurons exhibited a robust response to the sensory detection of food which was influenced by the metabolic state of the animal.

The dramatic increase in magnitude of response to the sensory detection of highly palatable food compared to regular chow may be reflective of the valuation of the food identity. It is possible that LH^{PV} neurons may also play a role in adjusting the valuation of food based on drive, as the degree of response to highly palatable food versus regular chow shifts during different metabolic states. Altogether, the experiments I have performed have revealed a novel role for LH^{PV} neurons in orchestrating feeding behaviors and provided further insight into how a diverse collection of genetically-identified cells

types within the lateral hypothalamus regulate neuronal circuits and behavior. Our findings will serve as a base for future revision of models of the lateral hypothalamic feeding circuitry and may yield potential therapeutic targets in the treatment of feeding disorders

References

1. Gao Q, Horvath TL. Neurobiology of feeding and energy expenditure. Annual review of neuroscience. 2007;30:367-98. doi: 10.1146/annurev.neuro.30.051606.094324. PubMed PMID: 17506645.
2. Gross CG. Aristotle on the Brain. The Neuroscientist. 1995;1(4):245-50. doi: 10.1177/107385849500100408.
3. Jellinger KA. Minds Behind the Brain. A History of the Pioneers and their Discoveries European Journal of Neurology Volume 13, Issue 7. European Journal of Neurology [Internet]. 2006 01; 13 7:[e13-e pp.]. Available from: http://onlinelibrary.wiley.com/doi/10.1111/j.1468-1331.2006.01158.x/abstract.
4. Bell C. XXVIII. On the nerves; giving an account of some experiments on their structure and functions, which lead to a new arrangement of the system. Philosophical Transactions of the Royal Society of London. 1821;111:398-424. doi: 10.1098/rstl.1821.0029.
5. Tubbs RS, Loukas M, Shoja MM, Shokouhi G, Oakes WJ. Francois Magendie (1783-1855) and his contributions to the foundations of neuroscience and neurosurgery. J Neurosurg. 2008;108(5):1038-42. Epub 2008/05/02. doi: 10.3171/JNS/2008/108/5/1038. PubMed PMID: 18447728.
6. Kandel ER, Schwartz JH, Jessell TM. Principles of neural science. Fourth ed: McGraw-Hill; 2000.
7. Descartes R, Cottingham J, Stoothoff R, Murdoch D. The Philosophical Writings of Descartes: Cambridge University Press; 1984.
8. Darwin C. The expression of the emotions in man and animals. London: J. Murray; 1872. vi, 374 p., 7 folded leaves of plates p.
9. Hull CL. Principles of behavior, an introduction to behavior theory. New York,: D. Appleton-Century Company; 1943. x p., 1 ., 422 p., 1 . p.
10. Lashley KS. Experimental analysis of instinctive behavior. Psychological Review. 1938;45(6):445-71. doi: 10.1037/h0060183.
11. Tinbergen N. The study of instinct. Oxford Eng.: Clarendon Press; 1951. 228 p. p.
12. Mayer J, Thomas DW. Regulation of food intake and obesity. Science. 1967;156(3773):328-37. Epub 1967/04/21. PubMed PMID: 4886532.
13. Kennedy GC. The role of depot fat in the hypothalamic control of food intake in the rat. Proc R Soc Lond B Biol Sci. 1953;140(901):578-96. Epub 1953/01/15. PubMed PMID: 13027283.
14. Hetherington AW, Ranson SW. Hypothalamic lesions and adiposity in the rat. Anat Rec. 1940;78(2):149-72. doi: DOI 10.1002/ar.1090780203. PubMed PMID: WOS:000187592600002.
15. Anand BK, Brobeck JR. Hypothalamic Control of Food Intake in Rats and Cats. Yale J Biol Med. 1951;24(2):123-40. PubMed PMID: WOS:A1951UY87400005.
16. Stellar E. The physiology of motivation. Psychological Review. 1954;61(1):5-22. doi: 10.1037/h0060347.

17. Ungerstedt U. Adipsia and aphagia after 6-hydroxydopamine induced degeneration of the nigro-striatal dopamine system. Acta Physiol Scand Suppl. 1971;367:95-122. Epub 1971/01/01. PubMed PMID: 4332694.
18. Kapatos G, Gold RM. Evidence for ascending noradrenergic mediation of hypothalamic hyperphagia. Pharmacology, biochemistry, and behavior. 1973;1(1):81-7. Epub 1973/01/01. PubMed PMID: 4204514.
19. Grossman SP, Grossman L. Iontophoretic injections of kainic acid into the rat lateral hypothalamus: effects on ingestive behavior. Physiology & behavior. 1982;29(3):553-9. Epub 1982/09/01. PubMed PMID: 7178261.
20. Grossman SP, Dacey D, Halaris AE, Collier T, Routtenberg A. Aphagia and adipsia after preferential destruction of nerve cell bodies in hypothalamus. Science. 1978;202(4367):537-9. Epub 1978/11/03. PubMed PMID: 705344.
21. Stricker EM, Swerdloff AF, Zigmond MJ. Intrahypothalamic injections of kainic acid produce feeding and drinking deficits in rats. Brain research. 1978;158(2):470-3. Epub 1978/12/15. PubMed PMID: 709378.
22. Hervey GR. The effects of lesions in the hypothalamus in parabiotic rats. The Journal of physiology. 1959;145(2):336-52. Epub 1959/03/03. PubMed PMID: 13642304; PMCID: PMC1356830.
23. Ingalls AM, Dickie MM, Snell GD. Obese, a new mutation in the house mouse. The Journal of heredity. 1950;41(12):317-8. Epub 1950/12/01. PubMed PMID: 14824537.
24. Coleman DL. Effects of parabiosis of obese with diabetes and normal mice. Diabetologia. 1973;9(4):294-8. Epub 1973/08/01. PubMed PMID: 4767369.
25. Coleman DL, Hummel KP. The influence of genetic background on the expression of the obese (Ob) gene in the mouse. Diabetologia. 1973;9(4):287-93. Epub 1973/08/01. PubMed PMID: 4588246.
26. Zhang Y, Proenca R, Maffei M, Barone M, Leopold L, Friedman JM. Positional cloning of the mouse obese gene and its human homologue. Nature. 1994;372(6505):425-32. Epub 1994/12/01. doi: 10.1038/372425a0. PubMed PMID: 7984236.
27. Tartaglia LA, Dembski M, Weng X, Deng N, Culpepper J, Devos R, Richards GJ, Campfield LA, Clark FT, Deeds J, Muir C, Sanker S, Moriarty A, Moore KJ, Smutko JS, Mays GG, Wool EA, Monroe CA, Tepper RI. Identification and expression cloning of a leptin receptor, OB-R. Cell. 1995;83(7):1263-71. Epub 1995/12/29. PubMed PMID: 8548812.
28. Stuber GD, Wise RA. Lateral hypothalamic circuits for feeding and reward. Nature neuroscience. 2016;19(2):198-205. Epub 2016/01/28. doi: 10.1038/nn.4220. PubMed PMID: 26814589; PMCID: PMC4927193.
29. Horvath TL, Bechmann I, Naftolin F, Kalra SP, Leranth C. Heterogeneity in the neuropeptide Y-containing neurons of the rat arcuate nucleus: GABAergic and non-GABAergic subpopulations. Brain research. 1997;756(1-2):283-6. Epub 1997/05/09. PubMed PMID: 9187344.
30. Boston BA, Blaydon KM, Varnerin J, Cone RD. Independent and additive effects of central POMC and leptin pathways on murine obesity. Science. 1997;278(5343):1641-4. Epub 1997/12/31. PubMed PMID: 9374468.

31. Ollmann MM, Wilson BD, Yang YK, Kerns JA, Chen Y, Gantz I, Barsh GS. Antagonism of central melanocortin receptors in vitro and in vivo by agouti-related protein. Science. 1997;278(5335):135-8. Epub 1997/10/06. PubMed PMID: 9311920.
32. Baskin DG, Breininger JF, Schwartz MW. Leptin receptor mRNA identifies a subpopulation of neuropeptide Y neurons activated by fasting in rat hypothalamus. Diabetes. 1999;48(4):828-33. Epub 1999/04/02. PubMed PMID: 10102700.
33. Aponte Y, Atasoy D, Sternson SM. AGRP neurons are sufficient to orchestrate feeding behavior rapidly and without training. Nature neuroscience. 2011;14(3):351-5. doi: 10.1038/nn.2739. PubMed PMID: 21209617; PMCID: 3049940.
34. Krashes MJ, Koda S, Ye C, Rogan SC, Adams AC, Cusher DS, Maratos-Flier E, Roth BL, Lowell BB. Rapid, reversible activation of AgRP neurons drives feeding behavior in mice. The Journal of clinical investigation. 2011;121(4):1424-8. Epub 2011/03/03. doi: 10.1172/jci46229. PubMed PMID: 21364278; PMCID: PMC3069789.
35. Clark JT, Kalra PS, Crowley WR, Kalra SP. Neuropeptide Y and human pancreatic polypeptide stimulate feeding behavior in rats. Endocrinology. 1984;115(1):427-9. Epub 1984/07/01. doi: 10.1210/endo-115-1-427. PubMed PMID: 6547387.
36. Stanley BG, Leibowitz SF. Neuropeptide Y: stimulation of feeding and drinking by injection into the paraventricular nucleus. Life Sci. 1984;35(26):2635-42. Epub 1984/12/24. PubMed PMID: 6549039.
37. Cowley MA, Smart JL, Rubinstein M, Cerdan MG, Diano S, Horvath TL, Cone RD, Low MJ. Leptin activates anorexigenic POMC neurons through a neural network in the arcuate nucleus. Nature. 2001;411(6836):480-4. Epub 2001/05/25. doi: 10.1038/35078085. PubMed PMID: 11373681.
38. Wang D, He X, Zhao Z, Feng Q, Lin R, Sun Y, Ding T, Xu F, Luo M, Zhan C. Whole-brain mapping of the direct inputs and axonal projections of POMC and AgRP neurons. Front Neuroanat. 2015;9:40. Epub 2015/04/15. doi: 10.3389/fnana.2015.00040. PubMed PMID: 25870542; PMCID: PMC4375998.
39. Betley JN, Cao ZF, Ritola KD, Sternson SM. Parallel, redundant circuit organization for homeostatic control of feeding behavior. Cell. 2013;155(6):1337-50. doi: 10.1016/j.cell.2013.11.002. PubMed PMID: 24315102.
40. Atasoy D, Aponte Y, Su HH, Sternson SM. A FLEX switch targets Channelrhodopsin-2 to multiple cell types for imaging and long-range circuit mapping. The Journal of neuroscience : the official journal of the Society for Neuroscience. 2008;28(28):7025-30. Epub 2008/07/11. doi: 10.1523/JNEUROSCI.1954-08.2008. PubMed PMID: 18614669; PMCID: PMC2593125.
41. Fodor M, Csaba Z, Epelbaum J, Vaudry H, Jegou S. Interrelations between hypothalamic somatostatin and proopiomelanocortin neurons. J Neuroendocrinol. 1998;10(2):75-8. Epub 1998/04/16. PubMed PMID: 9535052.
42. Bagnol D, Lu XY, Kaelin CB, Day HE, Ollmann M, Gantz I, Akil H, Barsh GS, Watson SJ. Anatomy of an endogenous antagonist: relationship between Agouti-related protein and proopiomelanocortin in brain. The Journal of neuroscience : the official journal of the Society for Neuroscience. 1999;19(18):RC26. Epub 1999/09/10. PubMed PMID: 10479719.

43. Mountjoy KG, Mortrud MT, Low MJ, Simerly RB, Cone RD. Localization of the melanocortin-4 receptor (MC4-R) in neuroendocrine and autonomic control circuits in the brain. Mol Endocrinol. 1994;8(10):1298-308. Epub 1994/10/01. doi: 10.1210/mend.8.10.7854347. PubMed PMID: 7854347.
44. Sahm UG, Qarawi MA, Olivier GW, Ahmed AR, Branch SK, Moss SH, Pouton CW. The melanocortin (MC3) receptor from rat hypothalamus: photoaffinity labelling and binding of alanine-substituted alpha-MSH analogues. FEBS Lett. 1994;350(1):29-32. Epub 1994/08/15. PubMed PMID: 8062918.
45. Zaborszky L, Makara GB. Intrahypothalamic connections: an electron microscopic study in the rat. Exp Brain Res. 1979;34(2):201-15. Epub 1979/01/15. PubMed PMID: 105917.
46. Betley JN, Xu S, Cao ZFH, Gong R, Magnus CJ, Yu Y, Sternson SM. Neurons for hunger and thirst transmit a negative-valence teaching signal. Nature. 2015;521(7551):180-5. Epub 2015/04/29. doi: 10.1038/nature14416. PubMed PMID: 25915020; PMCID: PMC4567040.
47. Chen Y, Lin YC, Kuo TW, Knight ZA. Sensory detection of food rapidly modulates arcuate feeding circuits. Cell. 2015;160(5):829-41. Epub 2015/02/24. doi: 10.1016/j.cell.2015.01.033. PubMed PMID: 25703096; PMCID: PMC4373539.
48. Mandelblat-Cerf Y, Ramesh RN, Burgess CR, Patella P, Yang Z, Lowell BB, Andermann ML. Arcuate hypothalamic AgRP and putative POMC neurons show opposite changes in spiking across multiple timescales. Elife. 2015;4. Epub 2015/07/15. doi: 10.7554/eLife.07122. PubMed PMID: 26159614; PMCID: PMC4498165.
49. Beutler LR, Chen Y, Ahn JS, Lin YC, Essner RA, Knight ZA. Dynamics of Gut-Brain Communication Underlying Hunger. Neuron. 2017;96(2):461-75 e5. Epub 2017/10/13. doi: 10.1016/j.neuron.2017.09.043. PubMed PMID: 29024666.
50. Chen Y, Lin YC, Zimmerman CA, Essner RA, Knight ZA. Hunger neurons drive feeding through a sustained, positive reinforcement signal. Elife. 2016;5. Epub 2016/08/25. doi: 10.7554/eLife.18640. PubMed PMID: 27554486; PMCID: PMC5016090.
51. Leinninger GM, Jo YH, Leshan RL, Louis GW, Yang H, Barrera JG, Wilson H, Opland DM, Faouzi MA, Gong Y, Jones JC, Rhodes CJ, Chua S, Jr., Diano S, Horvath TL, Seeley RJ, Becker JB, Munzberg H, Myers MG, Jr. Leptin acts via leptin receptor-expressing lateral hypothalamic neurons to modulate the mesolimbic dopamine system and suppress feeding. Cell metabolism. 2009;10(2):89-98. doi: 10.1016/j.cmet.2009.06.011. PubMed PMID: 19656487; PMCID: 2723060.
52. Celio MR, Babalian A, Ha QH, Eichenberger S, Clement L, Marti C, Saper CB. Efferent connections of the parvalbumin-positive (PV1) nucleus in the lateral hypothalamus of rodents. The Journal of comparative neurology. 2013;521(14):3133-53. Epub 2013/06/22. doi: 10.1002/cne.23344. PubMed PMID: 23787784; PMCID: PMC3772778.
53. Rosin DL, Weston MC, Sevigny CP, Stornetta RL, Guyenet PG. Hypothalamic orexin (hypocretin) neurons express vesicular glutamate transporters VGLUT1 or VGLUT2. The Journal of comparative neurology. 2003;465(4):593-603. Epub 2003/09/17. doi: 10.1002/cne.10860. PubMed PMID: 12975818.

54. Del Cid-Pellitero E, Jones BE. Immunohistochemical evidence for synaptic release of GABA from melanin-concentrating hormone containing varicosities in the locus coeruleus. Neuroscience. 2012;223:269-76. Epub 2012/08/15. doi: 10.1016/j.neuroscience.2012.07.072. PubMed PMID: 22890079.
55. Elias CF, Lee CE, Kelly JF, Ahima RS, Kuhar M, Saper CB, Elmquist JK. Characterization of CART neurons in the rat and human hypothalamus. The Journal of comparative neurology. 2001;432(1):1-19. Epub 2001/03/10. PubMed PMID: 11241374.
56. Harthoorn LF, Sane A, Nethe M, Van Heerikhuize JJ. Multi-transcriptional profiling of melanin-concentrating hormone and orexin-containing neurons. Cell Mol Neurobiol. 2005;25(8):1209-23. Epub 2006/01/03. doi: 10.1007/s10571-005-8184-8. PubMed PMID: 16388333.
57. Harris GC, Wimmer M, Aston-Jones G. A role for lateral hypothalamic orexin neurons in reward seeking. Nature. 2005;437(7058):556-9. Epub 2005/08/16. doi: 10.1038/nature04071. PubMed PMID: 16100511.
58. Adamantidis AR, Zhang F, Aravanis AM, Deisseroth K, de Lecea L. Neural substrates of awakening probed with optogenetic control of hypocretin neurons. Nature. 2007;450(7168):420-4. doi: 10.1038/nature06310. PubMed PMID: 17943086.
59. Jego S, Glasgow SD, Herrera CG, Ekstrand M, Reed SJ, Boyce R, Friedman J, Burdakov D, Adamantidis AR. Optogenetic identification of a rapid eye movement sleep modulatory circuit in the hypothalamus. Nature neuroscience. 2013;16(11):1637-43. Epub 2013/09/24. doi: 10.1038/nn.3522. PubMed PMID: 24056699; PMCID: PMC4974078.
60. Jennings JH, Ung RL, Resendez SL, Stamatakis AM, Taylor JG, Huang J, Veleta K, Kantak PA, Aita M, Shilling-Scrivo K, Ramakrishnan C, Deisseroth K, Otte S, Stuber GD. Visualizing hypothalamic network dynamics for appetitive and consummatory behaviors. Cell. 2015;160(3):516-27. Epub 2015/01/31. doi: 10.1016/j.cell.2014.12.026. PubMed PMID: 25635459; PMCID: PMC4312416.
61. Jennings JH, Rizzi G, Stamatakis AM, Ung RL, Stuber GD. The inhibitory circuit architecture of the lateral hypothalamus orchestrates feeding. Science. 2013;341(6153):1517-21. doi: 10.1126/science.1241812. PubMed PMID: 24072922; PMCID: 4131546.
62. Berk ML, Finkelstein JA. Efferent connections of the lateral hypothalamic area of the rat: an autoradiographic investigation. Brain research bulletin. 1982;8(5):511-26. Epub 1982/05/01. PubMed PMID: 6811106.
63. Matsumoto M, Hikosaka O. Lateral habenula as a source of negative reward signals in dopamine neurons. Nature. 2007;447(7148):1111-5. Epub 2007/05/25. doi: 10.1038/nature05860. PubMed PMID: 17522629.
64. Stamatakis AM, Van Swieten M, Basiri ML, Blair GA, Kantak P, Stuber GD. Lateral Hypothalamic Area Glutamatergic Neurons and Their Projections to the Lateral Habenula Regulate Feeding and Reward. The Journal of neuroscience : the official journal of the Society for Neuroscience. 2016;36(2):302-11. Epub 2016/01/14. doi: 10.1523/JNEUROSCI.1202-15.2016. PubMed PMID: 26758824; PMCID: PMC4710762.
65. Hu H, Gan J, Jonas P. Interneurons. Fast-spiking, parvalbumin(+) GABAergic interneurons: from cellular design to microcircuit function. Science.

2014;345(6196):1255263. Epub 2014/08/02. doi: 10.1126/science.1255263. PubMed PMID: 25082707.
66. Arif SH. A Ca(2+)-binding protein with numerous roles and uses: parvalbumin in molecular biology and physiology. Bioessays. 2009;31(4):410-21. Epub 2009/03/11. doi: 10.1002/bies.200800170. PubMed PMID: 19274659.
67. Sohal VS, Zhang F, Yizhar O, Deisseroth K. Parvalbumin neurons and gamma rhythms enhance cortical circuit performance. Nature. 2009;459(7247):698-702. Epub 2009/04/28. doi: 10.1038/nature07991. PubMed PMID: 19396159; PMCID: PMC3969859.
68. Schwaller B, Tetko IV, Tandon P, Silveira DC, Vreugdenhil M, Henzi T, Potier MC, Celio MR, Villa AE. Parvalbumin deficiency affects network properties resulting in increased susceptibility to epileptic seizures. Mol Cell Neurosci. 2004;25(4):650-63. Epub 2004/04/15. doi: 10.1016/j.mcn.2003.12.006. PubMed PMID: 15080894.
69. Marin O. Interneuron dysfunction in psychiatric disorders. Nature reviews Neuroscience. 2012;13(2):107-20. Epub 2012/01/19. doi: 10.1038/nrn3155. PubMed PMID: 22251963.
70. Shang C, Liu Z, Chen Z, Shi Y, Wang Q, Liu S, Li D, Cao P. BRAIN CIRCUITS. A parvalbumin-positive excitatory visual pathway to trigger fear responses in mice. Science. 2015;348(6242):1472-7. Epub 2015/06/27. doi: 10.1126/science.aaa8694. PubMed PMID: 26113723.
71. Melzer S, Gil M, Koser DE, Michael M, Huang KW, Monyer H. Distinct Corticostriatal GABAergic Neurons Modulate Striatal Output Neurons and Motor Activity. Cell Rep. 2017;19(5):1045-55. Epub 2017/05/04. doi: 10.1016/j.celrep.2017.04.024. PubMed PMID: 28467898; PMCID: PMC5437725.
72. Sparta DR, Hovelso N, Mason AO, Kantak PA, Ung RL, Decot HK, Stuber GD. Activation of prefrontal cortical parvalbumin interneurons facilitates extinction of reward-seeking behavior. The Journal of neuroscience : the official journal of the Society for Neuroscience. 2014;34(10):3699-705. Epub 2014/03/07. doi: 10.1523/JNEUROSCI.0235-13.2014. PubMed PMID: 24599468; PMCID: PMC3942585.
73. Kim H, Ahrlund-Richter S, Wang X, Deisseroth K, Carlen M. Prefrontal Parvalbumin Neurons in Control of Attention. Cell. 2016;164(1-2):208-18. Epub 2016/01/16. doi: 10.1016/j.cell.2015.11.038. PubMed PMID: 26771492; PMCID: PMC4715187.
74. Watson C, Paxinos G, Puelles L. The mouse nervous system. 1st ed. Amsterdam ; Boston: Elsevier Academic Press; 2012. xvii, 795 p. p.
75. Xu X, Roby KD, Callaway EM. Immunochemical characterization of inhibitory mouse cortical neurons: three chemically distinct classes of inhibitory cells. The Journal of comparative neurology. 2010;518(3):389-404. Epub 2009/12/02. doi: 10.1002/cne.22229. PubMed PMID: 19950390; PMCID: PMC2804902.
76. Meyer AH, Katona I, Blatow M, Rozov A, Monyer H. In vivo labeling of parvalbumin-positive interneurons and analysis of electrical coupling in identified neurons. The Journal of neuroscience : the official journal of the Society for Neuroscience. 2002;22(16):7055-64. Epub 2002/08/15. doi: 20026742. PubMed PMID: 12177202.
77. Inda MC, DeFelipe J, Munoz A. Morphology and distribution of chandelier cell axon terminals in the mouse cerebral cortex and claustroamygdaloid complex. Cereb Cortex.

2009;19(1):41-54. Epub 2008/04/29. doi: 10.1093/cercor/bhn057. PubMed PMID: 18440949.
78. Gabbott PL, Dickie BG, Vaid RR, Headlam AJ, Bacon SJ. Local-circuit neurones in the medial prefrontal cortex (areas 25, 32 and 24b) in the rat: morphology and quantitative distribution. The Journal of comparative neurology. 1997;377(4):465-99. Epub 1997/01/27. PubMed PMID: 9007187.
79. Kawaguchi Y, Kubota Y. Correlation of physiological subgroupings of nonpyramidal cells with parvalbumin- and calbindinD28k-immunoreactive neurons in layer V of rat frontal cortex. Journal of neurophysiology. 1993;70(1):387-96. Epub 1993/07/01. PubMed PMID: 8395585.
80. Zhu Y, Stornetta RL, Zhu JJ. Chandelier cells control excessive cortical excitation: characteristics of whisker-evoked synaptic responses of layer 2/3 nonpyramidal and pyramidal neurons. The Journal of neuroscience : the official journal of the Society for Neuroscience. 2004;24(22):5101-8. Epub 2004/06/04. doi: 10.1523/JNEUROSCI.0544-04.2004. PubMed PMID: 15175379.
81. Del Rio MR, DeFelipe J. A study of SMI 32-stained pyramidal cells, parvalbumin-immunoreactive chandelier cells, and presumptive thalamocortical axons in the human temporal neocortex. The Journal of comparative neurology. 1994;342(3):389-408. Epub 1994/04/15. doi: 10.1002/cne.903420307. PubMed PMID: 7517410.
82. Jinno S, Kosaka T. Parvalbumin is expressed in glutamatergic and GABAergic corticostriatal pathway in mice. The Journal of comparative neurology. 2004;477(2):188-201. Epub 2004/08/10. doi: 10.1002/cne.20246. PubMed PMID: 15300789.
83. Williams KW, Elmquist JK. Lighting up the hypothalamus: coordinated control of feeding behavior. Nature neuroscience. 2011;14(3):277-8. Epub 2011/02/25. doi: 10.1038/nn0311-277. PubMed PMID: 21346745; PMCID: PMC3755601.
84. Morton GJ, Cummings DE, Baskin DG, Barsh GS, Schwartz MW. Central nervous system control of food intake and body weight. Nature. 2006;443(7109):289-95. doi: 10.1038/nature05026. PubMed PMID: 16988703.
85. van den Pol AN. Weighing the role of hypothalamic feeding neurotransmitters. Neuron. 2003;40(6):1059-61. PubMed PMID: 14687541.
86. Williams KW, Elmquist JK. From neuroanatomy to behavior: central integration of peripheral signals regulating feeding behavior. Nature neuroscience. 2012;15(10):1350-5. doi: 10.1038/nn.3217. PubMed PMID: 23007190; PMCID: 3763714.
87. Krashes MJ, Shah BP, Koda S, Lowell BB. Rapid versus delayed stimulation of feeding by the endogenously released AgRP neuron mediators GABA, NPY, and AgRP. Cell metabolism. 2013;18(4):588-95. doi: 10.1016/j.cmet.2013.09.009. PubMed PMID: 24093681; PMCID: 3822903.
88. Adamantidis A, de Lecea L. Physiological arousal: a role for hypothalamic systems. Cellular and molecular life sciences : CMLS. 2008;65(10):1475-88. doi: 10.1007/s00018-008-7521-8. PubMed PMID: 18351292.
89. Cason AM, Smith RJ, Tahsili-Fahadan P, Moorman DE, Sartor GC, Aston-Jones G. Role of orexin/hypocretin in reward-seeking and addiction: implications for obesity. Physiology & behavior. 2010;100(5):419-28. doi: 10.1016/j.physbeh.2010.03.009. PubMed PMID: 20338186; PMCID: 2886173.

90. Celio MR. Calbindin D-28k and parvalbumin in the rat nervous system. Neuroscience. 1990;35(2):375-475. PubMed PMID: 2199841.
91. Meszar Z, Girard F, Saper CB, Celio MR. The lateral hypothalamic parvalbumin-immunoreactive (PV1) nucleus in rodents. The Journal of comparative neurology. 2012;520(4):798-815. doi: 10.1002/cne.22789. PubMed PMID: 22020694; PMCID: 3523738.
92. Markram H, Toledo-Rodriguez M, Wang Y, Gupta A, Silberberg G, Wu C. Interneurons of the neocortical inhibitory system. Nature reviews Neuroscience. 2004;5(10):793-807. Epub 2004/09/21. doi: 10.1038/nrn1519. PubMed PMID: 15378039.
93. DeFelipe J, Lopez-Cruz PL, Benavides-Piccione R, Bielza C, Larranaga P, Anderson S, Burkhalter A, Cauli B, Fairen A, Feldmeyer D, Fishell G, Fitzpatrick D, Freund TF, Gonzalez-Burgos G, Hestrin S, Hill S, Hof PR, Huang J, Jones EG, Kawaguchi Y, Kisvarday Z, Kubota Y, Lewis DA, Marin O, Markram H, McBain CJ, Meyer HS, Monyer H, Nelson SB, Rockland K, Rossier J, Rubenstein JL, Rudy B, Scanziani M, Shepherd GM, Sherwood CC, Staiger JF, Tamas G, Thomson A, Wang Y, Yuste R, Ascoli GA. New insights into the classification and nomenclature of cortical GABAergic interneurons. Nature reviews Neuroscience. 2013;14(3):202-16. doi: 10.1038/nrn3444. PubMed PMID: 23385869; PMCID: 3619199.
94. Opland D, Sutton A, Woodworth H, Brown J, Bugescu R, Garcia A, Christensen L, Rhodes C, Myers M, Jr., Leinninger G. Loss of neurotensin receptor-1 disrupts the control of the mesolimbic dopamine system by leptin and promotes hedonic feeding and obesity. Mol Metab. 2013;2(4):423-34. Epub 2013/12/12. doi: 10.1016/j.molmet.2013.07.008. PubMed PMID: 24327958; PMCID: PMC3857883.
95. Ting JT, Daigle TL, Chen Q, Feng G. Acute brain slice methods for adult and aging animals: application of targeted patch clamp analysis and optogenetics. Methods Mol Biol. 2014;1183:221-42. doi: 10.1007/978-1-4939-1096-0_14. PubMed PMID: 25023312; PMCID: 4219416.
96. Peng H, Bria A, Zhou Z, Iannello G, Long F. Extensible visualization and analysis for multidimensional images using Vaa3D. Nat Protocols. 2014;9(1):193-208. doi: 10.1038/nprot.2014.011.
97. Qi J, Zhang S, Wang HL, Barker DJ, Miranda-Barrientos J, Morales M. VTA glutamatergic inputs to nucleus accumbens drive aversion by acting on GABAergic interneurons. Nature neuroscience. 2016. doi: 10.1038/nn.4281. PubMed PMID: 27019014.
98. Root DH, Mejias-Aponte CA, Zhang S, Wang HL, Hoffman AF, Lupica CR, Morales M. Single rodent mesohabenular axons release glutamate and GABA. Nature neuroscience. 2014;17(11):1543-51. doi: 10.1038/nn.3823. PubMed PMID: 25242304.
99. Aponte Y, Lien CC, Reisinger E, Jonas P. Hyperpolarization-activated cation channels in fast-spiking interneurons of rat hippocampus. The Journal of physiology. 2006;574(Pt 1):229-43. doi: 10.1113/jphysiol.2005.104042. PubMed PMID: 16690716; PMCID: 1817792.
100. Livak KJ, Schmittgen TD. Analysis of relative gene expression data using real-time quantitative PCR and the 2(-Delta Delta C(T)) Method. Methods. 2001;25(4):402-8. doi: 10.1006/meth.2001.1262. PubMed PMID: 11846609.

101. Aponte Y, Bischofberger J, Jonas P. Efficient Ca2+ buffering in fast-spiking basket cells of rat hippocampus. The Journal of physiology. 2008;586(8):2061-75. doi: 10.1113/jphysiol.2007.147298. PubMed PMID: 18276734; PMCID: 2465201.
102. Krashes MJ, Shah BP, Madara JC, Olson DP, Strochlic DE, Garfield AS, Vong L, Pei H, Watabe-Uchida M, Uchida N, Liberles SD, Lowell BB. An excitatory paraventricular nucleus to AgRP neuron circuit that drives hunger. Nature. 2014;507(7491):238-42. doi: 10.1038/nature12956. PubMed PMID: 24487620; PMCID: 3955843.
103. Petreanu L, Huber D, Sobczyk A, Svoboda K. Channelrhodopsin-2-assisted circuit mapping of long-range callosal projections. Nature neuroscience. 2007;10(5):663-8. doi: 10.1038/nn1891. PubMed PMID: 17435752.
104. Delgado JM, Anand BK. Increase of food intake induced by electrical stimulation of the lateral hypothalamus. The American journal of physiology. 1953;172(1):162-8. Epub 1953/01/01. PubMed PMID: 13030733.
105. Olds J, Milner P. Positive reinforcement produced by electrical stimulation of septal area and other regions of rat brain. Journal of comparative and physiological psychology. 1954;47(6):419-27. Epub 1954/12/01. PubMed PMID: 13233369.
106. Stanley BG, Ha LH, Spears LC, Dee MG, 2nd. Lateral hypothalamic injections of glutamate, kainic acid, D,L-alpha-amino-3-hydroxy-5-methyl-isoxazole propionic acid or N-methyl-D-aspartic acid rapidly elicit intense transient eating in rats. Brain research. 1993;613(1):88-95. Epub 1993/06/04. PubMed PMID: 7688643.
107. Wu Z, Kim ER, Sun H, Xu Y, Mangieri LR, Li DP, Pan HL, Xu Y, Arenkiel BR, Tong Q. GABAergic projections from lateral hypothalamus to paraventricular hypothalamic nucleus promote feeding. The Journal of neuroscience : the official journal of the Society for Neuroscience. 2015;35(8):3312-8. Epub 2015/02/27. doi: 10.1523/JNEUROSCI.3720-14.2015. PubMed PMID: 25716832; PMCID: PMC4339348.
108. Kelly J, Rothstein J, Grossman SP. GABA and hypothalamic feeding systems. I. Topographic analysis of the effects of microinjections of muscimol. Physiology & behavior. 1979;23(6):1123-34. Epub 1979/12/01. PubMed PMID: 542523.
109. Gomez JL, Bonaventura J, Lesniak W, Mathews WB, Sysa-Shah P, Rodriguez LA, Ellis RJ, Richie CT, Harvey BK, Dannals RF, Pomper MG, Bonci A, Michaelides M. Chemogenetics revealed: DREADD occupancy and activation via converted clozapine. Science. 2017;357(6350):503-7. doi: 10.1126/science.aan2475. PubMed PMID: 28774929.
110. Rogan SC, Roth BL. Remote control of neuronal signaling. Pharmacol Rev. 2011;63(2):291-315. Epub 2011/03/19. doi: 10.1124/pr.110.003020. PubMed PMID: 21415127; PMCID: PMC3082452.
111. de Araujo IE, Gutierrez R, Oliveira-Maia AJ, Pereira A, Jr., Nicolelis MA, Simon SA. Neural ensemble coding of satiety states. Neuron. 2006;51(4):483-94. doi: 10.1016/j.neuron.2006.07.009. PubMed PMID: 16908413.
112. Burton MJ, Rolls ET, Mora F. Effects of hunger on the responses of neurons in the lateral hypothalamus to the sight and taste of food. Experimental neurology. 1976;51(3):668-77. PubMed PMID: 819286.
113. Mittmann W, Wallace DJ, Czubayko U, Herb JT, Schaefer AT, Looger LL, Denk W, Kerr JN. Two-photon calcium imaging of evoked activity from L5 somatosensory neurons

in vivo. Nature neuroscience. 2011;14(8):1089-93. Epub 2011/07/12. doi: 10.1038/nn.2879. PubMed PMID: 21743473.
114. Jung JC, Schnitzer MJ. Multiphoton endoscopy. Optics letters. 2003;28(11):902-4. Epub 2003/06/21. PubMed PMID: 12816240.
115. Levene MJ, Dombeck DA, Kasischke KA, Molloy RP, Webb WW. In vivo multiphoton microscopy of deep brain tissue. Journal of neurophysiology. 2004;91(4):1908-12. Epub 2003/12/12. doi: 10.1152/jn.01007.2003. PubMed PMID: 14668300.
116. Jung JC, Mehta AD, Aksay E, Stepnoski R, Schnitzer MJ. In vivo mammalian brain imaging using one- and two-photon fluorescence microendoscopy. Journal of neurophysiology. 2004;92(5):3121-33. Epub 2004/05/07. doi: 10.1152/jn.00234.2004. PubMed PMID: 15128753; PMCID: PMC2826362.
117. Bocarsly ME, Jiang WC, Wang C, Dudman JT, Ji N, Aponte Y. Minimally invasive microendoscopy system for in vivo functional imaging of deep nuclei in the mouse brain. Biomed Opt Express. 2015;6(11):4546-56. Epub 2015/11/26. doi: 10.1364/BOE.6.004546. PubMed PMID: 26601017; PMCID: PMC4646561.
118. Schneider CA, Rasband WS, Eliceiri KW. NIH Image to ImageJ: 25 years of image analysis. Nature methods. 2012;9(7):671-5. Epub 2012/08/30. PubMed PMID: 22930834; PMCID: PMC5554542.
119. Wallace ML, Saunders A, Huang KW, Philson AC, Goldman M, Macosko EZ, McCarroll SA, Sabatini BL. Genetically Distinct Parallel Pathways in the Entopeduncular Nucleus for Limbic and Sensorimotor Output of the Basal Ganglia. Neuron. 2017;94(1):138-52 e5. doi: 10.1016/j.neuron.2017.03.017. PubMed PMID: 28384468.

Biography

Julia E. Slocomb Dluzen was born in 1985 in the USA.

Julia did her undergraduate studies at Villanova University where she majored in Biology and minored in English Literature.

Julia subsequently worked for the Pennsylvania State University College of Medicine's Department of Neurology as a Research Coordinator and Technician for five years. During this period, she helped design, conduct, and analyze data for institutional and national scale clinical trials as well as write manuscripts and grants. She presented her findings regarding novel biomarkers for stroke and diabetes at both local and international scientific conferences. This work led to authorship of over a dozen publications in peer reviewed scientific journals.

In 2013 Julia joined the National Institutes of Health's Graduate Partnership Program with Johns Hopkins University's Cell, Molecular, Developmental Biology and Biophysics PhD program. She was the TA for two laboratory sections of Biology at JHU in 2013. In 2014 she joined Yeka Aponte's Neuronal Circuits and Behavior Unit at the National Institute on Drug Abuse (NIDA), where she studied the neuronal circuits that drive survival behaviors.